Performance Analysis and Resource Optimization in Free Space Optical Communication Networks

A THESIS

SUBMITTED IN PARTIAL FULFILLMENT OF THE REQUIREMENTS

FOR THE DEGREE OF

Doctor of Philosophy

By

Priyanka Singh

PhD19110

under the guidance of

Prof. Vivek Ashok Bohara
Professor, IIIT-Delhi
&
Prof. Anand Srivastava
Professor, IIIT-Delhi

INDRAPRASTHA INSTITUTE *of*
INFORMATION TECHNOLOGY **DELHI**

Department of Electronics & Communication Engineering
Indraprastha Institute of Information Technology, Delhi
June, 2025

Acknowledgments

My Ph.D. journey has been a rich tapestry of invaluable lessons and significant achievements, all culminating in this thesis. Its success is primarily attributed to the unwavering support and encouragement of many individuals throughout this process. I am deeply grateful to have these people in my life, and I want to express my heartfelt thanks to each of them. I would like to take this opportunity to express my sincere appreciation to all those who contributed to making this **Ph.D.** thesis possible.

First and foremost, I would like to express my deepest gratitude to my advisors, **Prof. Vivek Ashok Bohara** and **Prof. Anand Srivastava**, for their unwavering belief in me and their guidance throughout my Ph.D. journey. Their mentorship has played a pivotal role in my technical and personal growth. I feel incredibly fortunate to have been under their supervision, as their dedication and commitment to every task are truly inspiring. I thoroughly enjoyed our insightful discussions, which constantly challenged me to think critically. Without their guidance, this thesis would have remained a distant goal.

I also would like to express my heartfelt gratitude to my overseas collaborators, **Prof. Haythem Bany Salameh** and **Prof. Moussa Ayyash**, for their constant encouragement and invaluable support throughout this journey. Their participation truly made a significant difference.

I am deeply thankful to **Dr. Abhijit Mitra** and **Dr. Mukulika Maity** for serving as members of my monitoring committee. Their insightful feedback and thoughtful suggestions played an essential role in shaping my research, and I appreciate their generosity in dedicating their time to my work.

A special thanks goes to my friends, **Dr. Akshita Gupta** and **Rahul**, for their unwavering support during both the highs and the lows of this journey. The bond we have developed will continue to be a source of strength and joy for me in the years to come. I also would like to express my gratitude to my senior, **Dr. Anand Singh**, whose guidance and encouragement were incredibly valuable throughout my work. I would also like to express my appreciation to my labmates **Dr. Rana Kumar Jana, Neetu, Saumya,** and **Saswati** for their help, support, and the countless memorable moments we shared during my Ph.D.

This thesis would not have been possible without the financial support of the **University Grant Commission (UGC), Government of India**. I am deeply grateful for receiving **UGC-JRF** and **UGC-SRF** fellowships that supported my studies. A heartfelt thank you to the administrative staff at **IIIT-D** for their prompt assistance with administrative matters, ensuring that everything ran smoothly.

Finally, I cannot express enough gratitude to my family for their unwavering love and support. I dedicate this thesis to my beloved son, **Vivansh**. I would also like to thank my husband, **Dharmesh**, for his constant encouragement. This journey would not have been possible without his unyielding support and the countless sacrifices he has made for me. I will forever remain indebted to him.

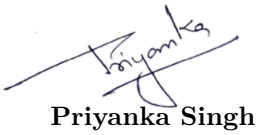

Priyanka Singh

PhD19110

Certificate

This is to certify that the thesis titled **"Performance Analysis and Resource Optimization in Free Space Optical Communication Networks"** being submitted by **Priyanka Singh** to **Indraprastha Institute of Information Technology, Delhi**, for the award of the **Doctor of Philosophy**, is an original research work carried out under our supervision. In our opinion, the thesis has reached the standards fulfilling the requirements of the regulations relating to the degree. The results contained in this thesis have not been submitted in part or full to any other university or institute for the award of any degree/diploma.

Prof. Vivek Ashok Bohara

Department of Electronics & Communication Engineering
Indraprastha Institute of Information Technology, Delhi

Prof. Anand Srivastava

Department of Electronics & Communication Engineering
Indraprastha Institute of Information Technology, Delhi

Declaration

This is to be certified that the dissertation entitled **"Performance Analysis and Resource Optimization in Free Space Optical Communication Networks"** being submitted by **Priyanka Singh** to the **Indraprastha Institute of Information Technology, Delhi**, for the award of degree of **Doctor of Philosophy**, is a bonafide work carried out by me. This research work has been carried out under the supervision of **Prof. Vivek Ashok Bohara** and **Prof. Anand Srivastava**. The study pertains to this dissertation has not been submitted in part or in full, to any other University or Institution for the award of any other degree.

Prof. Vivek Ashok Bohara

Department of Electronics & Communication Engineering
Indraprastha Institute of Information Technology, Delhi

Prof. Anand Srivastava

Department of Electronics & Communication Engineering
Indraprastha Institute of Information Technology, Delhi

Dedication

To My Husband & Son

for giving me the support and encouragement to follow my dreams.

Abstract

In today's world, wireless communication has become a necessity due to the growing reliance on data-intensive Internet usage. The growing need for high transmission rates in bandwidth-intensive applications, such as ultra-high-definition video streaming, video-on-demand, and online video, further intensifies the current radio frequency (RF) spectrum shortage. In contrast, optical wireless communication (OWC) leverages unlicensed infrared and visible spectrums to offer gigabit-per-second data rates and provides substantial bandwidth capacity. Free space optics (FSO) communication is a kind of OWC technology that utilizes an infrared spectrum to transmit modulated light through free space using a coherent optical source. Compared to traditional RF systems, FSO offers several advantages, including access to unlicensed spectrum, ultra-high data rates, reduced electromagnetic interference, and flexible deployment. However, its effectiveness is constrained by the requirement for a clear line-of-sight (LoS) between transmitter and receiver.

To address this limitation, this thesis investigates the use of an optical intelligent reflecting surface (OIRS), a passive beamforming device that enhances signal strength and mitigates LoS blockages. With their low cost, deployment flexibility, and range extension capabilities, OIRSs are poised to become integral components of future wireless networks. Despite the high data rate potential of FSO communication in next-generation networks, it remains vulnerable to physical-layer security threats, particularly jamming attacks that can lead to denial-of-service (DoS). This thesis explores robust designs to improve the resilience and performance of FSO-based networks under such challenges.

First, this thesis examines the performance of multiple possible integration architectures of the FSO/fiber-based back-end with the Light-Fidelity (LiFi)/Wireless-Fidelity (WiFi)-based front-end to deliver seamless connectivity to last-mile users. Link aggregation (LA) is also investigated to improve throughput and reliability. These proposed architectures are benchmarked against conventional architecture in terms of throughput, cost-per-bit, fairness, and reliability.

Next, the thesis proposes an integrated terrestrial-air-underwater (TAU) optical communication network and compares its performance with a traditional RF-based TAU network. A novel algorithm, COgnition-based Divergence Angle Tracking (CODAT) is introduced to dynamically optimize the divergence angle of the FSO beam, thereby improving data rate and minimizing outage probability.

To tackle LoS challenges in multi-user environments, the thesis further explores the integration of unmanned aerial vehicles (UAVs) with OIRS-assisted FSO systems to support quality-of-service (QoS) requirements. Specifically, a mirror element assignment problem is formulated and addressed using both a heuristic approach and a sequential-fixing linear programming (SFLP) method. These solutions demonstrate superior performance in sum rate, fairness, and user coverage compared to benchmark strategies.

Finally, the thesis presents a jamming-aware mirror element assignment scheme to mitigate physical-layer jamming in UAV and OIRS-assisted FSO networks. The proposed approach enhances system robustness by im-

proving sum rate, reducing blocking probability, and satisfying QoS constraints in adversarial environments. Overall, these contributions demonstrate the feasibility and effectiveness of robust FSO-based communication systems in various next-generation wireless network scenarios, offering significant advances in throughput, security, and deployment flexibility.

List of Publications

The following papers are the outcome of the work done towards this thesis:

Papers published in Refereed Journals

1. **P. Singh**, A. Gupta, V. A. Bohara and A. Srivastava, "QoS-Aware Reliable Architecture for Broadband Fiber-Wireless Access Networks", in *IEEE Systems Journal*, vol. 16, no. 4, pp. 5753-5764, Dec. 2022, doi: 10.1109/JSYST.2022.3149854.

2. **P. Singh**, V. A. Bohara and A. Srivastava, "On the Optimization of Integrated Terrestrial-Air-Underwater Architecture Using Optical Wireless Communication for Future 6G Network," in *IEEE Photonics Journal*, vol. 14, no. 6, pp. 1-12, Dec. 2022, Art no. 7355712, doi: 10.1109/JPHOT.2022.3210481.

3. **P. Singh**, V. A. Bohara and A. Srivastava, "Reliable and cost effective all-optical wireless architecture for a broadband access network," in *Journal of Optical Communications and Networking*, vol. 15, no. 2, pp. 98-110, February 2023, doi: 10.1364/JOCN.463574.

4. **P. Singh**, H. B. Salameh, V. A. Bohara, A. Srivastava and M. Ayyash, "Optimizing Connectivity in OIRS-Assisted UAV Indoor Optical Networks: Efficient Admission Control and Mirror-Element Assignment," in *IEEE Transactions on Network Science and Engineering*, vol. 11, no. 3, pp. 2890-2900, May-June 2024, doi: 10.1109/TNSE.2024.3353671.

5. **P. Singh**, H. B. Salameh, V. A. Bohara, A. Srivastava and M. Ayyash, "Jamming-Resilient Mirror Element Allocation Scheme for OIRS-aided UAV-based FSO Networks," in *IEEE Transactions on Intelligent Vehicles*, doi: 10.1109/TIV.2024.3450191.

6. **P. Singh**, H. B. Salameh, V. A. Bohara, A. Srivastava and M. Ayyash, "On Mitigating Reactive Jamming with Dynamic Resource Allocation in OIRS and UAV-assisted FSO-based Networks", in *Physical Communication*, 2024, 102520, ISSN 1874-4907, doi: 10.1016/j.phycom.2024.102520.

Papers submitted in Refereed Journals

1. **P. Singh**, V. A. Bohara and A. Srivastava, "Intelligent Mirror Element Assignment in OIRS-Aided UAV-based FSO Network under Different Environmental Conditions", submitted in *Physical Communication, 2025.*

Presentations in Conferences

1. **P. Singh**, A. Gupta, V. A. Bohara and A. Srivastava, "Cost Effective Hybrid FSO-Wireless Architecture for Broadband Access Network," *2022 International Conference on Optical Network Design and Modeling (ONDM)*, Warsaw, Poland, 2022, pp. 1-6, doi: 10.23919/ONDM54585.2022.9782861.

2. **P. Singh**, V. A. Bohara and A. Srivastava, "On the Optimal Assignment of Mirror Element in UAV and OIRS-Assisted OWC based Architecture," *2023 IEEE 97th Vehicular Technology Conference (VTC2023-Spring)*, Florence, Italy, 2023, pp. 1-7, doi: 10.1109/VTC2023-Spring57618.2023.10199990.

3. **P. Singh**, H. A. Bany Salameh, V. A. Bohara, A. Srivastava and M. Ayyash, "Opportunities and Challenges of OIRS-assisted UAV-based FSO Communication Systems", *2023 International Conference on Intelligent Computing, Communication, Networking and Services (ICCNS)*, Valencia, Spain, 2023, pp. 92-98, doi: 10.1109/ICCNS58795.2023.10193665.

4. K. Jeyapiriya, **P. Singh**, A. Singh and A. Srivastava, "Performance Analysis of DCO-OFDM based UWOC System under Varying Underwater Channel Conditions," *2023 IEEE International Conference on Advanced Networks and Telecommunications Systems (ANTS)*, Jaipur, India, 2023, pp. 1-6, doi: 10.1109/ANTS59832.2023.10469575.

5. S. S, **P. Singh**, A. Singh and A. Srivastava, "Hybrid RF-VLC Technology for V2X in Platooning Applications Under Different Weather Conditions," *2024 IEEE Wireless Communications and Networking Conference (WCNC)*, Dubai, United Arab Emirates, 2024, pp. 1-6, doi: 10.1109/WCNC57260.2024.10570908.

6. **P. Singh**, H. B. Salameh, V. A. Bohara, A. Srivastava and M. Ayyash, "Jamming Attacks on FSO Networks: Challenges, Opportunities, and a Public Safety Use-Case", *2024 IEEE World Forum on Public Safety Technology (WFPST)*, Herndon, VA, USA, 2024, pp. 7-12, doi: 10.1109/WFPST58552.2024.00027.

7. **P. Singh**, H. A. B. Salameh, V. A. Bohara, A. Srivastava and M. Ayyash, "Efficient Mirror Element Assignment in OIRS-Aided UAV-Based FSO Networks with Rate Adaptation", *2024 IEEE International Black Sea Conference on Communications and Networking (BlackSeaCom)*, Tbilisi, Georgia, 2024, pp. 13-16, doi: 10.1109/BlackSeaCom61746.2024.10646266.

Contents

List of Figures

List of Tables

Nomenclature

$\Gamma(\cdot)$	Gamma function
$K_x(\cdot)$	Modified bessel function of the second kind of order xth
$B(\cdot)$	Beta function
$\text{erf}(\cdot)$	Error function
$F(\cdot)$	CDF
$f(\cdot)$	PDF
$G_{\cdot,\cdot}^{\cdot,\cdot}(\cdot)$	Meijer-G function
$\mathbf{E}[\cdot]$	Expectation operator
$\mathcal{X}(\mu, \sigma^2)$	Log normal distribution
$\text{erfc}(\cdot)$	Complementary error function
$\delta(.)$	Dirac delta function
$\mathcal{N}(\mu, \sigma^2)$	denotes the Gaussian distribution with μ mean and σ^2 variance.

List of Abbreviations

5G fifth generation

6G sixth generation

3D three-dimensional

AoA angle of arrival

AON active optical network

AOS active optical splitter

AP access point

AR augmented reality

AS access slots

AW access window

AUV autonomous underwater vehicle

AWGN additive white Gaussian noise

B5G beyond 5G

BER bit error rate

BLP binary linear programming

BMEA batch-based user-selection and mirror-element assignment

BSFLP batch-based polynomial-time sequential-fixing linear programming

CAPEX capital expenditures

CC central controller

CCDF complementary cumulative distribution function

CDF cumulative distribution function

CO central office

CODAT COgnition-based Divergence Angle Tracking

CSMA/CA carrier sense multiple access with collision avoidance

DF decode-and-forward

DoS denial of services

EMA equal mirror element assignment

FoV field of view

FSO free space optical

FoLi free space optical-Light fidelity

FiLi fiber-Light fidelity

FoWi free space optical-WiFi

FiWi fiber-wireless

FoLA free space optical-Link aggregation

FiLA fiber-Link aggregation

GPS global positioning system

IRS intelligent reflecting surfaces

IM/DD intensity modulation and direct detection

JA-EMA jamming Aware-Equal Mirror element Allocation

JU-EMA jamming Unaware-Equal Mirror element Allocation

JA-MEA jamming Aware-Mirror element Allocation

JU-MEA jamming Unaware-Mirror element Allocation

LA link aggregation

LD laser diode

LED light emitting diode

LiFi light fidelity

LoS line-of-sight

LSD light-shaped diffuser

MA micro-mirror array

MCS modulation and coding scheme

MISO multiple-input, single-output

MR mixed reality

MZM mach zehnder modulator

NOMA non-orthogonal multiple access

NLBP non-linear binary linear programming problem

OCDMA optical code division multiple access

ODN optical distribution network

OIRS optical intelligent reflecting surfaces

ONU optical network unit

OOK on-off keying

OLT optical line terminal

OSS over sea surface

OWC optical wireless communication

PA phased array

PLR packet loss ratio

PD photodetector

PON passive optical network

PDF probability distribution function

PSD power spectral density

QoS quality of service

RF radio frequency

RJA-MEA Reactive Jamming Aware-Mirror Element Allocation

RJU-MEA Reactive Jamming UnAware-Mirror Element Allocation

RJA-EMEA Reactive Jamming Aware-Equal Mirror element Allocation

RJU-EMEA Reactive Jamming Unaware-Equal Mirror element Allocation

RLP relaxed linear programming

SFLP sequential-fixing linear programming

SINR signal to interference plus noise ratio

SISO single input single output

SNR signal to noise ratio

SJR signal-to-jamming noise ratio

SMA signal strength aware multiple mirror element assignment

TDM time division multiplexing

TDMA time division multiple access

TWDM time wavelength division multiplexing

TAU terrestrial Air Underwater

UAV unmanned aerial vehicle

UWOC underwater wireless optical communication

VLC visible light communication

VR virtual reality

VCSEL vertical-cavity surface-emitting laser

WDM wavelength division multiplexing

WiFi wireless fidelity

XGPON 10-Gigabit-capable passive optical network

Chapter 1

Introduction

This Chapter presents background, motivation, and objectives of this thesis while also providing an overview of the key research contributions and related publications.

1.1 Background

The massive usage of radio frequency (RF) devices has led to significant congestion and intense competition for access to the exclusive, licensed bands of the tightly regulated RF spectrum. As concerns over RF spectrum scarcity grow, there has been a significant shift towards exploring higher frequency ranges. This shift has driven the increasing popularity of millimeter waves and the optical band. Optical fibers have gained significant attention due to their ability to offer high bandwidth, immunity to electromagnetic interference, low security risks, and suitability for long-distance communication. However, despite these advantages, optical fiber technology faces considerable challenges, such as the high cost of installation, vulnerability to damage during installation or construction due to their fragility, and the need for specialized equipment for testing. As data traffic continues to increase exponentially, network service providers face growing challenges, including the demand for larger network capacities, reduced latency, higher data rates, and lower deployment costs. It's important to note that the large-scale deployment of optical fibers in traditional architectures may not be feasible in certain deployment scenarios, such as in remote locations, rugged terrains, or densely populated urban areas where the installation of additional fiber is restricted due to high costs and limited flexibility. One potential solution to address these challenges is the integration of free space optical (FSO) links into conventional network architectures. The FSO is an attractive solution as it offers greater flexibility and easier redeployment. The FSO has numerous benefits, such as providing unlicensed spectrum, high bandwidth, immunity to electromagnetic interference, high-speed communication, and quick deployment to the end-users [1]. FSO communication utilizes laser technology to transmit a highly collimated optical beam through the atmosphere to a designated receiver within the line-of-sight (LoS) path. Experimental studies have demonstrated that FSO systems are capable of achieving data rates comparable to those of optical fiber, making them a promising solution for delivering high-speed last-mile connectivity to remote or hard-to-reach end users.

1.2 Motivation

The sixth generation (6G) communication network is envisioned to meet the growing demand for exceptional quality of service (QoS), offering features such as extremely high data rates (1–10 Tbps), ultra-low latency (down to 0.1 ms), minimal delay jitter (around 1 s), massive device connectivity (up to 10^7 connections per km^2), and seamless coverage, as summarized in Table. 1.1 [2, 3]. As 6G technology evolves, services such as streaming and augmented / virtual reality mobile devices will require significantly higher data rates. To support delay-sensitive and reliable services, 6G aims to increase network capacity by 10 to 100 times compared to fifth generation (5G) [3].

Table 1.1: Comparison of 5G and 6G Performance Requirements

Feature	**5G Target**	**6G Vision**
Peak Data Rate	Up to 10 Gbps	1–10 Tbps
Latency	1 ms	0.1 ms
Device Connectivity	$\sim 10^6$ / km^2	10^7 / km^2
Mobility Support	Up to 500 km/h	$\geq$1000 km/h
Spectrum Utilization	Sub-100 GHz	Up to THz bands
Reliability	99.999%	99.9999%+
Energy Efficiency	Moderate	Highly optimized

As 6G technology evolves, services such as streaming and augmented / virtual reality mobile devices will require significantly higher data rates. To support delay-sensitive and reliable services, 6G aims to increase network capacity by 10 to 100 times compared to 5G [3]. Table. 1.2 provides a comparative overview of key enabling technologies for 6G communication networks, highlighting their operating spectrum, advantages, and associated challenges. These technologies collectively form the foundation of a robust, flexible, and high-capacity 6G architecture, particularly in scenarios requiring high data rates, ultra-low latency, and diverse deployment environments. The space–air–ground-integrated network has also emerged as a promising architecture to meet the demands of 6G networks, offering seamless access, extensive coverage, and low-latency transmissions [4]. However, the limited availability of licensed spectrum poses a significant challenge, as existing RF communication systems have reached saturation. Even with some available RF spectrum, achieving ambitious 6G data rate targets (in the order of Tbps) remains challenging due to the restricted bandwidth of the RF systems [5]. FSO communication is a promising solution that emerges as a strong candidate for the 6G networks. With its high capacity and license-free operation, FSO can help meet the 6G performance requirement using its wide bandwidths, from hundreds of GHz to THz [6]. In addition, links between ground stations and satellites can achieve even higher data rates, making FSO communication a compelling option. The future 6G network is also expected to offer full integration among terrestrial, air, and underwater communication entities.

Table 1.2: Comparison of Key Technologies for 6G Networks

Technology	**Spectrum**	**Advantages**	**Challenges**
Free space optics	THz/Infrared	High data rate, license-free, immune to RF interference	Line-of-sight requirement, weather sensitivity
Visible light communication	Visible light	Unlicensed spectrum, low interference, safe for humans	Limited to short-range, requires illumination
Millimeter-Wave	30–300 GHz	Wide bandwidth, suitable for dense urban areas	High path loss, penetration issues
Terahertz communication	0.1–10 THz	Ultra-high capacity, low latency	Hardware limitations, absorption losses

FSO enables long-distance point-to-point communication with higher data rates due to the coherent nature of laser light. Therefore, integrating an FSO-based back-end with a wireless fidelity (WiFi)-based front-end in 10-Gigabit-capable passive optical network (XGPON) architecture can leverage the strengths of both technologies, offering flexibility and high data rates in hybrid FSO-based networks [7]. Additionally, visible light communication (VLC) has emerged as a promising solution for short-range, indoor communication. In VLC, transmitters like light emitting diode (LED)s or laser diode (LD)s generate optical signals, which are received by photodetector (PD)s and converted into electrical signals for further processing. VLC provides benefits such as unlicensed bandwidth, no electromagnetic interference, and widespread availability [8]. light fidelity (LiFi), a networking extension of VLC, facilitates point-to-multipoint communication in indoor settings. Hence, an FSO-based back-end can complement a LiFi-based front-end in XGPON architecture, delivering high transmission rates while improving the overall performance of hybrid FSO networks.

Despite its advantages, FSO, as a LoS technology, faces challenges due to channel impairments. These include fading caused by weather variations, atmospheric turbulence, misalignment errors between transmitters and receivers, and physical blockages. Such impairments significantly impact the data-carrying capacity of FSO communication channels [9–11]. The key challenge in FSO implementation is maintaining a clear LoS between devices. Recently, optical intelligent reflecting surfaces (OIRS) and unmanned aerial vehicle (UAV)s have gained attention as effective technologies to overcome non-LoS issues in communication systems [12, 13].

UAV-assisted FSO-based networks hold the promise of augmenting the performance of terrestrial communication systems. By acting as mobile relays between the communicating devices, UAVs can circumvent the strict LoS requirement, thus improving connectivity. This integration is envisioned to significantly improve the capabilities of future 6G networks [14], [15]. Recently, OIRS have been employed to achieve notable performance enhancements in communication networks, particularly in scenarios where LoS connectivity is unavailable or is affected by "skip-zone" issues. The skip-zone refers to coverage gaps where the optical signal cannot reach the intended receiver without degradation. This challenge highlights the importance of strategic optical network planning to ensure seamless and reliable data transmission. OIRS functions as a passive device comprised of micro-mirror elements or metasurfaces, enabling signal beamforming toward the user's direction to enhance

received signal strength. Beyond this, OIRS presents additional advantages, including flexibility, ease of deployment, cost effectiveness, and extended communication coverage [9, 16, 17]. OIRS is expected to improve the performance of FSO-based networks, particularly in scenarios where LoS connectivity is not available.

An OIRS-assisted UAV, where the OIRS is mounted on the UAV, can function as a mobile relay between communication devices, reducing the dependency on LoS in FSO-based networks [18]. This setup is anticipated to significantly enhance the performance of conventional FSO-based systems.

However, despite FSO technology's potential for high data rates in next-generation wireless networks, it is vulnerable to security threats such as jamming attacks in the physical layer, which can escalate to denial of services (DoS) attack. A jamming attack is an intentional disturbance where the attacker deliberately transmits high-power directed optical signals to disrupt the legitimate receiver [19, 20]. FSO technology has certain inherent technical limiting factors that make it vulnerable to jamming attacks, such as the wide field of view (FoV) of the receiver's aperture, easily detectable operating wavelengths, and easily trackable FSO receivers [19–21].

Motivated by these challenges, this research aims to investigate performance and explore the benefits and trade-offs of integrating FSO/fiber-based back-end with LiFi/WiFi-based front-end under adverse channel conditions. Additionally, we examine the end-to-end performance of an integrated terrestrial Air Underwater (TAU) optical communication framework, accounting for FSO and underwater wireless optical communication (UWOC) channel impairments. Moreover, previous studies have not addressed resource allocation in OIRS-assisted UAV-based FSO networks. In particular, no optimization framework has been proposed for mirror element allocation to serve multiple users in these networks. This research specifically addresses the mirror element allocation problem under QoS design constraints.

FSO technology presents a promising opportunity to increase next-generation network capacity due to its unlicensed spectrum and wide bandwidth. However, jamming attacks, combined with inherent channel anomalies, pose significant threats to the performance of FSO-based networks. This is particularly concerning for security-sensitive applications that require a resilient communication infrastructure. Therefore, evaluating the performance of FSO-based networks under jamming attacks is crucial to designing modern and reliable communication systems.

1.3 Objectives

The primary objective of this thesis is to evaluate the performance of FSO-based communication networks and to optimize resource allocation within these networks. The specific objectives of the thesis are as follows.

- Examine the performance of various integration architectures that combine the FSO/fiber-based back-end with the LiFi/WiFi-based front-end, considering the effects of channel fading, atmospheric turbulence, and pointing errors. In addition, the link aggregation (LA) approach is employed to enhance the performance of these hybrid architectures.
- Analyze the end-to-end performance of integrated TAU optical communication networks and improve performance by optimizing the divergence angle of the optical beam.

- To evaluate the performance of OIRS-assisted UAV-based FSO network and improve their performance using a mirror element allocation scheme.
- Investigate the impact of jamming attacks on OIRS-assisted UAV-based FSO networks, and enhance network performance by employing optimal mirror element allocation.

1.4 Research Contributions

The main contributions presented in this thesis are as follows:

- The performance of a novel hybrid free space optical-Light fidelity (FoLi) architecture is investigated under the impact of channel attenuation, atmospheric turbulence, and pointing errors. As a performance benchmark, we have compared the performance of FoLi with two other hybrid architectures, namely, hybrid fiber-Light fidelity (FiLi) and hybrid free space optical-WiFi (FoWi), in which fiber and FSO-based back-end are integrated with LiFi and WiFi-based front-end, respectively. We further explore the performance improvement of active optical network (AON) by incorporating LA into the front-end network. Specifically, we complement standalone LiFi and WiFi with the LA framework and consequently propose two more integration scenarios, i.e., hybrid fiber-Link aggregation (FiLA) and hybrid free space optical-Link aggregation (FoLA) architecture. We also compare the cost analysis in terms of capital expenditures (CAPEX) and cost-per-bit of the proposed architectures with the conventional fiber-wireless (FiWi) architecture.
- The end-to-end performance of an integrated FiWi based UAV assisted hybrid FSO and UWOC system. The performance of the proposed system is investigated by taking into account the impact of the channel impairments such as atmospheric attenuation, pointing errors, atmospheric turbulence, and underwater turbulence. In addition, divergence angle of optical beam in the aerial network is optimized using the proposed COgnition-based Divergence Angle Tracking (CODAT) algorithm.
- The performance of OIRS-assisted UAV-based FSO networks is investigated under the impact of channel impairments. The optimization framework is presented for mirror element allocation to serve multiple users in OIRS-assisted UAV-based FSO networks.
- The performance of OIRS-assisted UAV-based FSO networks under the jamming attack is investigated. A novel mirror element allocation scheme is proposed to mitigate proactive jamming attacks in such networks while satisfying a set of QoS requirements for the users. The performance of the proactive jamming-aware mirror allocation scheme is compared against other reference schemes. Likewise, we generalized this scenario to a reactive jamming attack. Furthermore, the performance of a reactive jamming-aware mirror element allocation scheme is analyzed and compared with other existing schemes.

1.5 Thesis organization

The rest of the thesis is organized as follows:

- Chapter 2 presents the background and related work of this thesis. Initially, the basics of FSO are briefly discussed, along with its potential benefits and limitations. This chapter also provides the concept of OIRS, UAV, and jamming attacks. It is followed by a discussion of the literature on the performance of conventional FSO-based networks. In addition, the fundamentals of the OIRS and UAVs are discussed, along with the motivation for utilizing the OIRS and UAVs. Likewise, the related literature on the performance of OIRS and UAV-assisted FSO-based networks is also reviewed. Furthermore, an overview of the vital issue of jamming attacks on FSO-based networks and its related literature is discussed.

- Chapter 3 presents a comparison of the end-to-end performance of the hybrid FSO/fiber-based back-end and the LiFi/WiFi-based front-end architecture under the impact of channel fading, atmospheric turbulence, and pointing errors. An analytical expression of the outage probability of the end-to-end hybrid FSO-LiFi FoLi architecture is also presented in this chapter. This chapter focuses on the end-to-end performance of proposed architectures such as hybrid FoLi, FoWi, FiLi, FiLA, and FoLA with the conventional FiWi architecture in terms of average throughput, fairness, capital expenditure CAPEX, cost per bit, and reliability.

- Chapter 4 discusses the end-to-end performance of an integrated FiWi-based UAV-assisted hybrid FSO and UWOC network in terms of the outage probability. The analytical expression for the outage probability of the proposed system using FSO and UWOC channel statistics is derived in this chapter. Further, in the latter part of this chapter, the problem formulation for optimizing the divergence angle and the proposed CODAT algorithm are presented. Moreover, as a performance benchmark, the end-to-end outage performance of the proposed system is compared with a conventional RF-based TAU communication network.

- Chapter 5 presents an analytical framework to investigate the performance of OIRS-assisted UAV-based FSO networks under the consideration of atmospheric turbulence, attenuation, misalignment error, and angle of arrival (AoA) fluctuations. In addition, the problem formulation and proposed scheme for the assignment of mirror elements are presented. This chapter also evaluates and compares our proposed scheme with state-of-the-art schemes.

- Chapter 6 presents the formulation of a mirror element allocation problem in OIRS-assisted UAV-based FSO networks and takes into account FSO channel conditions and user rate demands while being aware of jamming attacks. It also compares the performance of the proposed mirror element scheme with respect to conventional benchmark schemes in terms of user rate demand, achieved sum rate, and severity of the jamming attack.

- Chapter 7 summarizes the contributions of the work and outlines possible directions for future work.

Chapter 2

Background and Related Works

2.1 Introduction

This chapter presents a comprehensive review of existing research related to FSO-based communication systems, their integration with UAVs, and the emerging role of OIRS in enhancing communication performance for 6G networks. The review highlights significant developments in FSO technologies, identifies the limitations of current systems, and discusses key challenges such as atmospheric impairments, jamming threats, and LoS maintenance. Special emphasis is placed on UAV-assisted FSO systems, hybrid RF/FSO communication frameworks, and resource optimization strategies involving OIRS. Additionally, the chapter identifies critical research gaps that shape the objectives of this study and discusses real-world applications of FSO-based communication networks.

This chapter introduces the fundamental concepts and related mathematical expressions that form the foundation of the work presented in this thesis. These foundational elements are necessary for formulating the mathematical models of different system configurations, which will be explored in later chapters. While FSO links have been extensively researched, with various aspects covered by numerous studies, this chapter focuses specifically on those relevant to our work. In summary, it presents the necessary concepts and equations that will aid in the analysis and derivation of performance metrics for the system.

The structure of this chapter is organized as follows: Section 2.2 provides an overview of FSO communication systems and their channel impairments. Section 2.3 reviews OIRS and its application in FSO and hybrid networks. Section 2.4 examines the impact of jamming attacks on FSO-based communication and existing mitigation strategies. Section 2.5 summarizes the identified research gaps and outlines the motivation for the research presented in subsequent chapters. Finally, Section 2.6 presents practical applications of FSO-based communication networks.

2.2 Free space optical communication

FSO communication is one of the most cost-effective wireless solutions capable of meeting the high QoS requirements in next-generation wireless networks, including beyond 5G (B5G) and 6G. FSO offers numerous

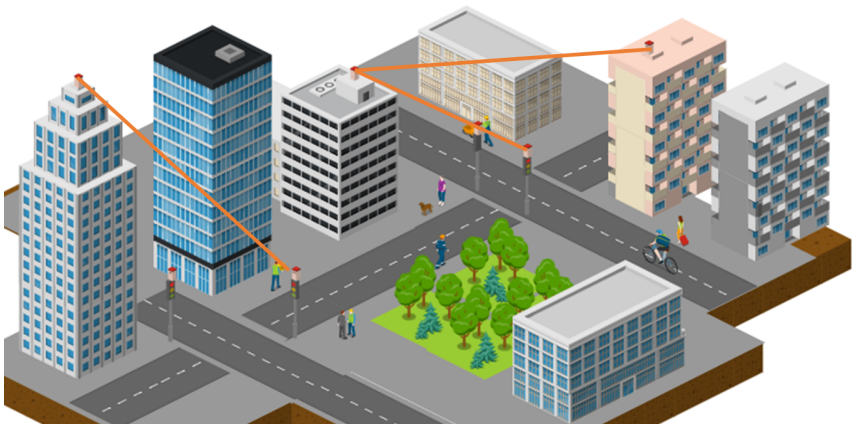

Figure 2.1: An application of FSO communication

advantages such as an unlicensed spectrum, high bandwidth, immunity to electromagnetic interference, high-speed data transmission, and rapid deployment [1]. It is a flexible and easily deployable solution that uses a laser diode as a transmitter and a photodetector as a receiver. Due to the coherent nature of laser light, FSO enables long-distance, point-to-point communication with high data rates [7], which is illustrated in Fig. 2.1.

2.2.1 Motivation for FSO communication

The evolution of the next 6G of cellular networks is attracting considerable attention from many researchers. In the near future, 6G networks are poised to achieve remarkable performance benchmarks such as low latency, high energy efficiency, high security, high data rates, and massive device connectivity [2]. Conventional RF resources do not meet these rigorous demands. The high data rate requirements for bandwidth-intensive applications, such as high-definition video streaming, augmented reality (AR), mixed reality (MR), and virtual reality (VR), exaggerate the RF spectrum crunch. However, FSO technology is expected to provide users with high data rates with minimal installation costs. FSO technology offers several benefits, such as wide bandwidth, low latency, greater flexibility for deployment, unlicensed spectrum, and less electromagnetic interference [9–11]. Furthermore, FSO offers ease of deployment and long-distance communication with a high transmission rate. The potential of FSO technology has recently attracted significant attention. Despite all these notable advantages, the FSO link experiences several channel impairments, such as fading due to varying weather conditions, atmospheric turbulence, pointing errors due to misalignment between transmit and receive apertures, and physical blockages. Table. 2.1 captures the main physical-layer challenges encountered in FSO-based networks. These impairments in the FSO channel affect the information carrying capacity of the FSO-based communication channels to a greater extent [9–11]. However, the key challenge in the large-scale deployment of FSO is to provide LoS between communicating devices.

Table 2.1: Channel Impairments in FSO Systems

Impairment	Cause	Impact on FSO Performance
Atmospheric attenuation	Absorption and scattering by atmospheric particles such as fog, rain, and snow	Leads to significant signal loss and reduced transmission range, especially in dense fog conditions
Atmospheric turbulence	Variations in temperature and pressure causing refractive index fluctuations	Results in signal scintillation, beam wander, and intensity fluctuations, degrading signal quality
Pointing errors	Misalignment between transmitter and receiver due to building sway, vibrations, or wind	Causes beam misdirection or partial signal loss, especially in narrow-beam FSO systems
Obstructions	Physical objects such as birds, trees, or temporary obstructions in LoS path	Interrupts the optical link, causing temporary outages

2.2.2 Modeling of FSO communication link

FSO link is affected by three key distance-dependent impairments: atmospheric attenuation, atmospheric turbulence, and pointing errors [22] as illustrated in Fig. 2.2. The atmospheric attenuation is governed by the Beer-Lambert Law [23], while atmospheric turbulence arises from random fluctuations in the refractive index of the atmosphere, typically modeled using the Gamma-Gamma distribution [24]. Pointing errors, another critical challenge, result from beam misalignment between the transmitter and receiver, often caused by factors such as strong winds, thermal expansion, or seismic activity. To mitigate pointing errors, acquisition, tracking, and pointing systems can be employed to maintain beam alignment [15]. Additionally, installing multiple FSO apertures at the transmitter can further reduce the impact of beam misalignment [25].

2.2.2.1 Absorption, Scattering, and Turbulence

In FSO communication, the atmosphere serves as the transmission medium, playing a crucial role in the performance of the link. The atmosphere consists of different layers, commonly categorized as the troposphere, stratosphere, mesosphere, thermosphere, and exosphere. For terrestrial FSO communications, the troposphere is particularly significant. This layer contains most of the water vapor and aerosols, is the site of weather phenomena, and experiences variations in pressure and temperature. Since FSO relies on a line-of-sight path between optical transceivers, any physical obstruction or atmospheric conditions such as rain, snow, fog, or haze that reduce visibility are problematic. Additionally, the presence of gases, water vapor, and suspended particulate matter causes absorption and scattering of the optical beam as it propagates through the troposphere. Both absorption and scattering are wavelength-dependent and attenuate the optical signal. Absorption and scattering are deterministic phenomena that are often grouped together under the term “extinction," which refers to the loss or attenuation of the propagation optical beam. This loss can be mathematically expressed using the Beer-Lambert law, which is given as in [26]:

$$h_a = \exp\left(-k_l L_F\right), \tag{2.1}$$

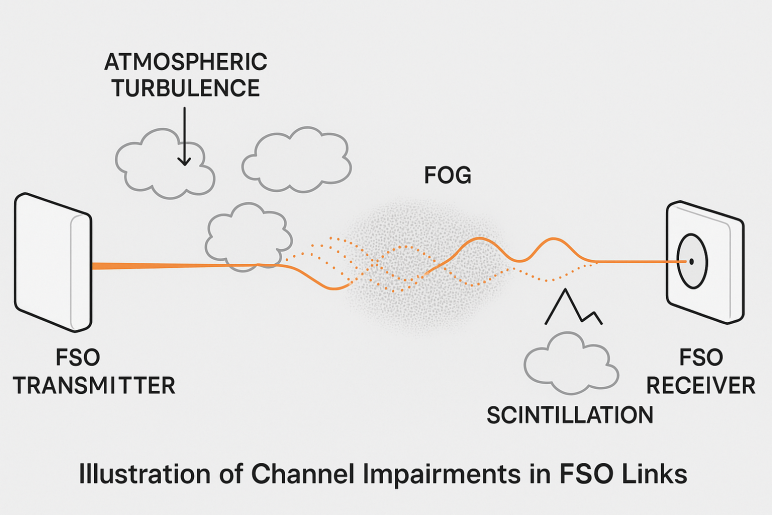

Figure 2.2: Channel impairments in FSO communication

where k_l is the extinction coefficient and is related to the absorption and scattering of the optical beam (in km^{-1}) over a distance of L_F (in km). Atmospheric turbulence occurs due to irregular air motions or eddies of varying sizes, which are driven by fluctuations in air pressure, wind velocity, and temperature gradients in the atmosphere. Atmospheric turbulence is typically caused when wind, in the presence of a temperature gradient, moves over a terrain with aerodynamically rough features. This interaction results in fluctuations in the refractive index of the atmosphere, a phenomenon known as atmospheric turbulence. Several models have been proposed in the literature to represent weak to strong atmospheric turbulence, such as the negative exponential, lognormal, K-distribution, Gamma-Gamma, Double Generalized Gamma, Double Weibull, M-distribution, and Málaga distribution. In works like [27],[28],[29], the Gamma-Gamma distribution is recognized as the most realistic model for FSO links, as it closely aligns with experimental results and applies to a wide range of atmospheric turbulence conditions [30]. As a result, the Gamma-Gamma distribution has gained widespread acceptance in current research. For the analysis in this thesis, the FSO channel will be modeled using the Gamma-Gamma distribution. Atmospheric turbulence is modeled as a random process following a Gamma-Gamma distribution, with its probability distribution function (PDF) expressed as [26]

$$f_{h_{at}}(h_{at}) = \frac{2(\alpha_f\beta_f)^{\frac{\alpha_f+\beta_f}{2}}}{\Gamma(\alpha_f)\Gamma(\beta_f)} h_{at}^{\frac{\alpha_f+\beta_f}{2}-1} K_{\alpha_f-\beta_f}(2\sqrt{\alpha_f\beta_f h_{at}}), \tag{2.2}$$

where $\Gamma(\cdot)$ is a Gamma function and $K_x(\cdot)$ is a modified Bessel function of the second kind of order xth. α_f and β_f are the scintillation parameters of FSO link f that are further expressed as [26]

$$\begin{aligned} \alpha_f &= \frac{1}{\left[\exp\left(\frac{0.49\sigma_R^2}{(1+0.56\sigma_R^{12/5})^{7/6}}\right)-1\right]}, \\ \beta_f &= \frac{1}{\left[\exp\left(\frac{0.51\sigma_R^2}{(1+0.69\sigma_R^{12/5})^{5/6}}\right)-1\right]}, \end{aligned} \tag{2.3}$$

where σ_R^2 is the Rytov variance is denoted as $\sigma_R^2 = 1.23C_n^2\left(\frac{2\pi}{\lambda}\right)^{7/6} L_F^{11/6}$ and λ represents the wavelength of the optical beam in meters, and L_F is the FSO link length in meters. The value of the coefficient 1.23 used for the

Rytov variance corresponds to the plane wave assumption often used in UAV-based FSO system modeling. This formulation, as found in [23], is appropriate for the propagation geometry and atmospheric conditions considered. The use of 1.23 is consistent with the modeling assumptions and aligns with prior literature examining similar UAV-assisted FSO configurations. However, the coefficient 0.5 for the Rytov variance is typically used in terrestrial FSO channel modeling, where links are near the ground and spherical wave propagation is assumed, commonly accepted practice in such scenarios. The parameter C_n^2 characterizes the refractive index and denotes the strength of atmospheric turbulence, ranging from 10^{-13} $\mathrm{m}^{-2/3}$ for strong turbulence to 10^{-16} $\mathrm{m}^{-2/3}$ for weak turbulence [26]. For a horizontal path, the value of C_n^2 is taken to be a constant, whereas, for ground-to-space link and space-to-ground link, the C_n^2 is modeled as a function of altitude, H (in meters) has to be used. For inclined paths, the so-called Hufnagel-Valley model is generally used [14]. In an FSO link, C_n^2 decreases with altitude H (up to 3 km) [14]. The refraction structure parameter C_n^2 is defined as $C_n^2 \approx C_n^2(0)\exp(\frac{-H}{100})$, where $C_n^2(0)$ is the refraction structure parameter in the horizontal link and H is the height of the FSO link above ground level in meters.

2.2.2.2 Pointing Errors

Any deviation from the desired LoS of the FSO links results in a pointing error or misalignment between the optical transceiver pair, which can significantly degrade the performance of the FSO link. The pointing error is also generated due to atmospheric turbulence-induced beam drift and is considered to be of particular importance for FSO links [26]. The PDF of pointing error is expressed as [26]

$$f_{h_p}(h_p) = \frac{\xi^2}{A_0^{\xi^2}}(h_p)^{\xi^2-1}, \tag{2.4}$$

where $A_0 = [\mathrm{erf}(v)]^2$ represents the fraction of the collected power within a circular aperture centered at radial distance zero, $\mathrm{erf}(\cdot)$ denotes the error function, and $v = \frac{\sqrt{\pi}a}{\sqrt{2}\omega}$ with a being the aperture radius and ω the beam radius. ξ is the pointing error coefficient, which is defined in terms of the standard deviation of the jitter σ_j and the equivalent beam waist ω_{L_F} at distance L_F as [26]

$$\xi = \frac{\omega_{L_F}}{2\sigma_j}, \tag{2.5}$$

FSO link is affected by atmospheric turbulence, mainly caused by the random fluctuation of the refractive index of the atmosphere. In addition to the atmospheric turbulence effect, the pointing error also affects the performance of the FSO link. To mitigate the effect of misalignment, we can install an acquisition, tracking, and pointing system to align the optical beam [15]. However, the misalignment problem can also be alleviated by the installation of multiple FSO apertures at FSO transmitter [25]. The PDF of the channel fading due to atmospheric turbulence, atmospheric loss, and pointing error is expressed as [26]

$$f_h(h) = \frac{\xi^2\alpha_f\beta_f}{A_0 h_a \Gamma(\alpha_f)\Gamma(\beta_f)} G_{1,3}^{3,0}\left(\frac{\alpha_f\beta_f}{A_0 h_a}h \middle| \begin{matrix} \xi^2 \\ \xi^2-1, \alpha_f-1, \beta_f-1 \end{matrix}\right), \tag{2.6}$$

where, $G_{\cdot,\cdot}^{\cdot,\cdot}(\cdot)$ is the Meijer-G function. The PDF of the instantaneous signal to noise ratio (SNR) (γ_{FSO}) is

expressed as [26]

$$f_{\gamma_{FSO}}(\gamma) = \frac{\xi^2}{\Gamma(\alpha_f)\Gamma(\beta_f)}\gamma^{-1}G_{1,3}^{3,0}\left(\frac{\alpha_f\beta_f\wp}{\bar{\gamma}_{FSO}}\gamma\middle|\begin{matrix}\xi^2+1\\ \xi^2,\alpha_f,\beta_f\end{matrix}\right), \tag{2.7}$$

where, $\wp = \xi^2/\xi^2+1$ and $\bar{\gamma}_{FSO}$ is average electrical SNR. On integrating (6.31), the corresponding cumulative distribution function (CDF) of the SNR is expressed as

$$F_{\gamma_{FSO}}(\gamma) = \frac{2\xi^2}{\Gamma(\alpha_f)\Gamma(\beta_f)}G_{2,4}^{3,1}\left(\frac{\alpha_f\beta_f\wp}{\bar{\gamma}_{FSO}}\gamma\middle|\begin{matrix}1,\xi^2+1\\ \xi^2,\alpha_f,\beta_f,0\end{matrix}\right). \tag{2.8}$$

2.2.3 Related Works

In recent years, advancements in FSO technology have made it a promising alternative to optical fibers, primarily due to its lower installation costs. FSO systems are especially advantageous in locations where optical fiber installation and trenching are challenging or impractical [1]. For example, in [31], the authors proposed a time wavelength division multiplexing (TWDM)-passive optical network (PON) architecture integrating both PON and FSO links to ensure survivability against fiber failures. In [32], the performance of an FSO-based optical code division multiple access (OCDMA) PON system was analyzed, with the FSO link between the optical line terminal (OLT) and passive splitter. In [33], the integration of optical baseband, FSO, and millimeter wave traffic in the PON architecture was explored using on-off keying (OOK) signals. Similarly, [34] investigated bidirectional time division multiplexing (TDM) FSO-based PON. Studies such as [35] examined how weather parameters (e.g. temperature, humidity, wind speed) affect fiber-FSO-fiber networks, while [36] proposed a hybrid system combining TWDM PON with FSO and evaluated its performance in terms of bit error rate (BER). Furthermore, in [37], the performance of wavelength division multiplexing (WDM) PON, integrating fiber and FSO links with modulation and detection using modified OOK signals, was examined. A cost analysis of the hybrid PON-FSO approach for fronthaul networks was also conducted in [38], comparing it with standalone PON architectures.

Despite all these notable advantages, the FSO link experiences several channel impairments, such as fading due to varying weather conditions, atmospheric turbulence, pointing errors due to misalignment between transmit and receive apertures, and physical blockages. These impairments in the FSO channel affect the information carrying capacity of the FSO-based communication channels to a greater extent [9–11]. However, the key challenge in the large-scale deployment of FSO is to provide LoS between communicating devices. An effective solution to mitigate these challenges is using UAVs as aerial relays for FSO links.

UAVs are expected to play an important role in 6G communication networks when deployed as aerial base stations or mobile aerial relays [39]. Recently, the use of UAV has evolved as a promising solution in FSO-based communication systems for providing LoS links for longer FSO links, including the necessity of precise FSO link alignment [40], [41]. UAV-based FSO relays could be deployed in challenging terrain to provide high throughput and reliable services. The channel modeling of a UAV-based FSO communication system is proposed under the combined effects of atmospheric attenuation, atmospheric turbulence, pointing errors, and AoA fluctuation in [42]. The end-to-end performance of the UAV-based FSO communication system is analyzed under the effect

of the channel impairments in [43], [44], and [14, 45, 46]. UAV is communicated with the ground station via FSO as a backhaul link, and UAV can transmit information to users through an RF link in [46].

The ground station sends the information to UAV via FSO link as a backhaul link, and thereafter UAV transmits the information to the users via RF links in [14]. UAV-assisted hybrid RF and FSO-based communication systems optimized the optical beam's divergence angle to maximize data rate with minimizing outage probability in [43]. The beam width of the optical beam and position of the UAV is optimized under the impact of the position and height of the building in UAV assisted FSO-based communication system in [44]. The architecture for remotely charging a UAV via laser beam has been proposed in [47]. The optimal trajectory-planning of a laser-charged UAV was proposed in [48], [49]. Finally, exploiting FSO as backhaul and energizer for the UAV, which works as an aerial relay, novel optimization frameworks were also developed in [50], [51]. As research progresses, it is evident that laser-driven wireless power transfer is a more feasible solution to overcome the UAV's energy limitations in aerial communication networks. The trajectory of UAV should also be optimized such that the flight time of UAV is maximized in order to satisfy the requirement of the desired data rate [45].

2.3 Optical Intelligent Reflecting Surfaces (OIRS)

In recent years, intelligent reflecting surfaces (IRS) may considerably enhance the performance of wireless communication systems in case of 'skip-zone' problems and the non-availability of LoS. IRS is expected to be one of the key technologies for the 6G communication network. IRS can reflect or beamform the signal in the user's desired direction, and it is a passive device. IRS can be employed for FSO and RF-based communication systems. IRS has numerous benefits, such as low cost, easier installation, and energy efficient. Currently, IRS can be designed in the form of mirrors, micro-mirrors, and metasurfaces [16]. RF-based IRS is assumed to be composed of metasurfaces. In the case of RF-based IRS, the output power distribution on the IRS surface is uniformly distributed, and the incident wavefront can be modeled as planar. While in the case of FSO-based OIRS, the optical power distribution on the OIRS surface is non-uniform and has a curved wavefront since the optical beam in FSO communication is modeled as a Gaussian beam [52]. Contrary to RF-based IRS communication systems, the development of an FSO-based OIRS communication system is still in a nascent stage and is a topic of intensive research. OIRS is a near-passive device that can reflect the signal in the desired direction and alter the shape of the signal to form a beam. In [17], two architectures for FSO-based OIRS are proposed in a point-to-multipoint FSO communication system, which is a micro-mirror array (MA) and phased array (PA). MA-based OIRS consists of multiple micro-mirror units and can converge the optical beam in the desired direction by mechanical adjustment of their orientations. MA-based OIRS has the potential benefit of low cost and more comprehensive coverage so that it can be applied in broad application scenarios of the FSO-based communication system. Like RF-based IRS, PA-based OIRS is composed of multiple programmable phased modulation units, which can modify the beam direction and shape by adjusting the phase distribution of the phased modulation units. MA and PA-based OIRS can realize beam convergence, deflection, and beam splitting [17].

2.3.1 Motivation for Optical Intelligent Reflecting Surfaces

In a traditional FSO communication system, the performance loss for the entire network is huge when obstacles block optical channels. FSO operates as a LoS technology that transmits data via a modulated optical beam across free space. The primary challenge for the widespread adoption of FSO technology lies in maintaining a clear LoS between the communicating devices. OIRS has the potential to greatly improve the performance of FSO-based networks, particularly in scenarios where LoS connectivity is not feasible. As a result, OIRS can be utilized in a wide variety of realistic application scenarios [9, 16, 17]. OIRS is expected to improve the performance of FSO-based networks, specifically when LoS is not available [18]. Hence, the OIRS-assisted UAV, where the OIRS is mounted on the UAV, can be used as a mobile relay between the communicating devices so that the requirement of LoS is mitigated [53]. Consequently, an OIRS-assisted UAV is expected to significantly enhance the performance of conventional FSO-based networks. OIRS-assisted UAVs can help in existing wireless infrastructure by improving their coverage area, spectral efficiency, and QoS parameters because of the unique attributes of UAVs, such as three-dimensional (3D) maneuverability, autonomous governing, and flexible deployment. OIRS-assisted UAV-based FSO communication system is also appropriate for challenging deployment scenarios such as in difficult terrains, the city's center, and remote locations [54]. Moreover, in the absence of communication infrastructure, OIRS-assisted UAV emerges as a cost-effective solution that can provide on-demand coverage and the required data rate to users.

2.3.2 Modeling of Optical Intelligent Reflecting Surfaces

In this thesis, we explore the application of OIRS in FSO-based networks. Existing implementations of OIRS encompass mirrors, micro-mirrors, and metasurfaces [16]. Previous research has outlined two primary architectures for OIRS: mirror-based and phased array-based. Mirror-based OIRS utilizes multiple micromirror elements that can mechanically adjust their orientations to converge the optical beam in the desired direction [17]. The optical power distribution on the surface of mirror-based OIRS exhibits non-uniformity and a curved wavefront, as the optical beam in FSO communication is typically modeled as a Gaussian beam [52]. PA-based OIRS, on the other hand, employs multiple programmable phase modulation units capable of adjusting the beam shape and direction by manipulating the phase distribution across these units. Both types of OIRS can achieve tasks such as beam convergence, deflection, and beam splitting [17].

Furthermore, we consider a mirror-based OIRS with a square geometrical shape, comprising an array of multiple micromirror elements. These mirror elements are capable of orientation adjustments through mechanical actuators and are controlled by a dedicated controller [13]. Moreover, the orientation angle of each mirror element θ_i is adjusted to achieve beamforming in a specific direction. The orientation angle θ_i is defined as follows [17]:

$$\cos\theta_i = \left| \frac{h_{x_i}\left(\frac{x_j - x_i}{2l_1} - \frac{x_s}{2l_2}\right) + h_{y_i}\left(\frac{y_j - y_i}{2l_1} - \frac{y_s}{2l_2}\right) + h_{z_i}\left(\frac{z_j - z_i}{2l_1} - \frac{z_s}{2l_2}\right)}{l_3} \right|, \tag{2.9}$$

where normal vectors are denoted by $(h_{x_i}, h_{y_i}, h_{z_i})$. The coordinates of a mirror element are represented as (x_i, y_i, z_i). The coordinates of the users and the optical transmitter are (x_j, y_j, z_j) and (x_s, y_s, z_s) respectively.

$l_1 = \sqrt{(x_j - x_i)^2 + (y_j - y_i)^2 + (z_j - z_i)^2}$, $l_2 = \sqrt{x_s^2 + y_s^2 + z_s^2}$, and $l_3 = \sqrt{\frac{1}{2} - \frac{(x_j - x_i)x_s + (y_j - y_i)y_s + (z_j - z_i)z_s}{2l_1 l_2}}$. The distribution of the received power density $\mathcal{P}_i$ is expressed as in [12, 17]

$$\mathcal{P}_i(x, y) = \frac{\mathcal{K} A_c^2}{\omega_{L_F}^2} exp\left[-\frac{2((x + x_i)^2 + (y + y_i)^2)}{\omega_{L_F}^2}\right], \tag{2.10}$$

where ω_{L_F} is the radius of the beam on the surface of OIRS, $\mathcal{K}$ represents the power factor and A_c is the central amplitude of the beam.

2.3.3 Related Works

Integrating UAV and OIRS could be a viable and efficient solution to provide high QoS in FSO-based communication for 6G communication networks. The deployment of an OIRS-assisted UAV as a mobile aerial relay between the transmitter and the receiver for mitigating the non-LoS and blockage challenges in 6G communication networks [55], [56]. In [53], the authors analyzed the performance of a UAV and IRS-based assisted hybrid FSO/RF system under the impact of effects of atmospheric attenuation, turbulence, pointing errors, and phase error of IRS. In this work, the authors proposed that UAV is equipped with IRS and serves as a relay node for a hybrid RF/FSO-based communication link between transmitter and receiver. In [57], the authors proposed an IRS-based FSO communication system, where the IRS is deployed on the building to serve as a fixed relay node to maintain the LoS communication link between two buildings in the presence of blockages. In [58], the authors evaluated the pointing errors under the effect of building sway and also analytically modeled the FSO channel under the impact of size, position, and orientation of IRS. In [56], the authors investigated the performance of an OIRS-assisted hybrid RF/FSO system in terms of symbol error probability and outage probability under the effect of multiple OIRS elements, atmospheric turbulence, and pointing error. The deep neural network was also employed in a UAV-assisted RF-based IRS-based communication system to determine the outage probability by considering the impact of channel impairments in [55]. Three protocols for sharing the IRS by multiple FSO links were proposed in [59], and the performance of the point-to-point IRS-assisted FSO system in terms of the BER and outage probability was analyzed.

2.4 Jamming Attacks on FSO Networks

In many realistic applications, delivering messages between devices on time is always required. These applications are often associated with critical human tasks such as health care, road safety, and defense, where a high level of security is crucial. Unfortunately, due to the specific characteristics of the FSO-based infrastructure, achieving security is more complex than in traditional networks. FSO-based networks are prone to jamming attacks due to their inherent technical limitations. The jammer transmits illegitimate emissions of optical signals to block the legitimate transmission between the optical transmitter and the receiver. The intervention of malicious optical transmitters, such as jammers in the FSO network, deliberately uses the optical signal to disrupt the communication between a legitimate transmitter and an FSO receiver, which can result in higher-layer security problems such as DoS.

Jamming in an FSO-based communication network is the most challenging threat, for which limited research has been conducted. Since FSO links are highly immune to interference, it is widely considered that they are not easy to disrupt, which has resulted in minimal investigation of jamming attacks in FSO systems. However, the broadcast nature and channel impairments of the FSO communication system make it prone to intrusion by adversaries. Consequently, in the presence of an adversary, FSO technology cannot uniquely support all requirements of 6G communication networks.

In FSO-based networks, jamming is intentional interference to destroy legitimate communications by corrupting signals received by FSO receivers. Jamming attacks primarily the physical layer. However, cross-layer attacks are also possible. Therefore, it is essential to be aware of the jamming activities so that a proper countermeasure can be taken. Jamming activity in FSO-based networks is relatively less studied and analyzed than in RF-based networks [60–62]. Jamming attacks in FSO-based networks are more feasible and cost-effective. RF jamming is a frequency-dependent activity in which RF-based jammers utilize a transmitter to radiate jamming signals tuned to a similar operating frequency and modulation type. In addition, RF-based jammers are expensive, since they usually require large batteries to enhance their jamming radius.

2.4.1 Vulnerabilities of FSO-based Networks against Jamming Attacks

A jammer obstructs legitimate transmission between the optical transmitter and the receiver by directly jamming the receiver aperture of the legitimate receiver. In this section, we explore the factors that can make FSO-based networks susceptible to jamming attacks.

- **Detectable operating wavelength:** The FSO transmission is most likely to operate at 830 nm, 1300 nm, and 1550 nm wavelength. In most realistic application scenarios, FSO transceivers operate at 1550 nm, the most common operating wavelength. Therefore, the jammer can easily know the operating wavelength ranges. It becomes clear that an attacker could easily jam and disrupt the dedicated FSO communication link [20].

- **Wider FoV**: To mitigate the adverse fading effect of atmospheric turbulence, angle of arrival fluctuations, and boresight angle in an FSO-based network, the size of the apertures of the FSO receivers is kept large, which in turn results in a wide FoV [21]. A wide FoV of FSO receivers maximizes signal reception by significantly reducing fading effects. However, due to the wide FoV of the FSO receiver, the FSO-based network is more susceptible to jamming attacks. A wide beamwidth of the optical beam and a wide FoV of the FSO receiver are required to tolerate pointing errors in FSO-based networks. This makes FSO-based networks more susceptible to jamming attacks.

- **Inexpensive FSO jammer**: FSO-based networks operate on an unlicensed spectrum; therefore, the illegitimate intruder does not need a license to launch the optical signal to jam the legitimate transmission. Additionally, an FSO transmitter is a low-cost device that is easy to install at the top of the building due to its small size and lightweight.

- **Trackable FSO receiver**: In general, FSO transceivers are placed at the top of buildings. Therefore,

illegitimate intruders can quickly identify the position of a legitimate FSO receiver.

- **Relay-assisted FSO-based network**: To establish long-distance point-to-point communication in an FSO-based network, multiple relays are required. Heavy traffic loss occurs if the jammer targets any of the relays and the entire network performance is disturbed.

2.4.2 Classification of Jamming Attacks in FSO-based Networks

We classify different jammers that may be used against FSO-based networks. FSO-based jammers are broadly classified as proactive, reactive, and advanced. Proactive jammers do not require pre-knowledge about the network infrastructure and user traffic. A reactive jammer monitors the network and starts jamming only when it observes any network activity on a communication channel. Advanced jammers are power efficient and more effective in jamming attacks. These jammers can be implemented as hybrid jammers with both proactive and reactive jamming techniques. Jammers in FSO-based networks are further classified as random jammers, persistent jammers, deceptive jammers, passive jammers, and smart jammers [63–66].

- **Random Jammer:** A random jammer jams the communication channel by intermittently transmitting random bits to the legitimate FSO receiver. This type of jamming activity is very energy-efficient because it is active only for the jamming phase. Otherwise, it is in sleep mode. Hence, the random jammer can save its transmit power. It is challenging to detect the jamming activity of a random jammer since its operation switches between active and sleep mode.

- **Persistent Jammer:** Unlike a random jammer, the persistent jammer continuously transmits jamming signals and random bits to a legitimate FSO receiver without following a media access control protocol. A persistent jammer keeps a legitimate communication channel busy until its transmit power is exhausted. Therefore, a persistent jammer requires significant power for its operation. This type of jamming activity offers ease in launching the jamming signal. However, persistent jamming can be easily detected due to its continuous presence.

- **Deceptive Jammer:** A deceptive jammer continuously transmits jamming signals as regular packets similar to a legitimate transmission. In this type of jamming activity, a deceptive jammer misleads the legitimate FSO receiver as if actual data is taking place. Unlike persistent jammers, this type of jamming attack is difficult to trace because it sends regular packets instead of random bits.

- **Passive Jammer:** A passive jammer reflects a legitimate source signal from the legitimate transmitter, affecting the legitimate FSO receiver. A passive jammer requires power for its operation, and this type of jamming is not energy-efficient. A large size of legitimate FSO receiver aperture is needed to effectively detect passive jamming to absorb the legitimate source signal.

- **Reactive Jammer:** This type of jamming attack is the most energy-efficient. A reactive jammer starts transmitting jamming signals only when the legitimate transmission is detected. It is much more challenging to detect the presence of a reactive jammer because the loss of a fair packet cannot be estimated accurately in practice.

- **Smart Jammer**: A smart jammer makes a jamming attack effective by combining two or more different types of jamming above. This jamming attack is energy-efficient since it fairly utilizes its transmit power to jam the FSO-based network. It is difficult to detect its presence and mitigate its impact.

2.4.3 Related Works

In [67], the authors analyzed the performance of a single input single output (SISO) FSO-based network in the presence of a jammer. A multiple-input, single-output (MISO) FSO-based network is proposed to mitigate the impact of jamming attacks. The performance of the MISO and SISO FSO-based network is evaluated in terms of BER. In [68], the authors propose threshold-based detection to detect legitimate transmission in the presence of a jammer. A MISO FSO-based network is utilized to alleviate the impact of jamming attacks. The performance comparison of MISO and SISO FSO-based networks in the presence of a jammer is studied in terms of BER, outage probability, and diversity order. The jamming attack is investigated under the effect of FSO channel impairments such as atmospheric turbulence and pointing errors over Gamma-Gamma fading channels, along with the pointing error. In [20], the authors developed a non-cooperative game where two players, the jammer and legitimate users, interact competitively to maximize secrecy capacity and minimize energy consumption. In this non-cooperative game model, energy-efficient attack and defense are considered utility functions for both players, the jammer and the legitimate user. In [69], the authors propose using a buffer on the relay node to combat the effects of jamming attacks on FSO-based networks. A max-link selection protocol is used to select the best possible link for communication at any given instant, which offers significant performance enhancement in FSO-based networks. The authors compared the performance of non-buffer-aided and buffer-aided in terms of BER and outage probability. In [70], the authors analyzed the jamming effect on the UAV-assisted FSO link. The authors employ threshold-based detection to detect jamming activity in legitimate transmission. The authors analytically derived and analyzed the BER expression for FSO-based networks assisted by UAVs in the presence of a random jammer. The performance of the UAV-assisted FSO-based network is examined under the combined effect of jamming activity, pointing error, and Gamma-Gamma followed atmospheric turbulence. In [71], the authors compared a suboptimal and an approximated threshold-based detector for detecting jamming activity in the relay-assisted FSO-based network. A suboptimal and an approximated threshold-based detector are derived from a maximum likelihood detector. Moreover, the authors analytically derived and analyzed the BER and diversity gain expression for relay-based FSO-based networks with an arbitrary number of relays in the presence of a random jammer. In the research mentioned above work, the jammer is considered a stationary entity in the research mentioned above. However, in [72], the authors deemed mobile UAV jammers in IRS-assisted UAV and FSO-based networks. Furthermore, the authors compared two types of scenarios. In the first scenario, the UAV acts as a jammer, corrupting the signal received at the UAV as a relay between the source and destination. However, in the second scenario, the UAV, as a jammer, jams the received signal at the destination. Furthermore, analytical expressions for the BER and outage probability for both scenarios have been derived in the presence of a random jammer. To mitigate the jamming effect, an IRS is utilized, and the performance of the proposed system in the presence and absence of the IRS is also demonstrated for different scenarios.

2.5 Key Challenges and Research Gaps

While FSO-based networks have garnered attention due to their potential to provide cost-effective and high-performance alternatives to traditional optical fiber networks, several critical gaps in the current literature require further investigation. Despite progress in overcoming some technical challenges, substantial hurdles remain that limit the large-scale deployment and operational efficiency of FSO-based networks. Below are key research gaps that need to be addressed:

- A significant gap in the literature is the lack of comprehensive studies that address the degradation of FSO network performance under a variety of challenging environmental conditions. While some research has focused on individual factors like atmospheric attenuation, turbulence, and pointing errors, the combined impact of these impairments on FSO-based networks, particularly in dynamic environments, is insufficiently explored. Moreover, the effect of environmental factors such as temperature fluctuations, wind, and rain on long-term FSO-based networks' performance remains largely unexamined, which could hinder the reliability of FSO-based networks in various climates.

- Maintaining a clear LoS for FSO-based networks remains a significant barrier for its deployment, especially in urban and obstructed environments. UAVs have been proposed as potential solutions to overcome these challenges by acting as aerial relays. However, the precise optimization of UAV positioning, path planning, and mobility is not adequately addressed in the existing literature. Most studies focus on the effects of individual channel impairments, yet fail to consider how UAV mobility, dynamic environmental factors, and link alignment collectively affect system performance over time.

- The integration of FSO with RF technologies to create a hybrid communication network has been explored, but there is a lack of in-depth research on the optimal resource allocation strategies for such networks. Existing studies primarily focus on system performance metrics like BER and outage probability, without addressing joint optimization strategies that balance the advantages and limitations of both FSO and RF technologies. Developing optimization frameworks that consider beam alignment, throughput maximization, and efficient load balancing in the hybrid network is a crucial area for further research, especially as 6G networks demand high-throughput and low-latency communication solutions.

- As FSO and UAV technologies are increasingly integrated into large-scale communication networks, the challenges of managing scalability and resource distribution across multiple UAVs and OIRSs become more apparent. Existing research, while offering valuable insights into small-scale and point-to-point systems, does not adequately address the coordination and interference management needed in large-scale deployments. Research is needed on scalable architectures for UAV-assisted OIRS and hybrid FSO/ RF networks, with a focus on coordination between multiple UAVs, resource allocation among OIRS elements, and efficient interference management in dense network environments.

- Most existing research focuses on optimizing system performance in the short term, such as minimizing outage probability or maximizing throughput. However, long-term optimization strategies for UAV-assisted

FSO-based networks are underexplored. These strategies should consider network scalability, the lifecycle of UAVs and OIRS elements, operational costs, and the integration of dynamic environmental changes. Understanding how to optimize UAV-assisted FSO-based networks for long-term operations, including resource planning and network management, will be essential for the sustainability of these systems in future 6G networks.

- While many studies have examined jamming effects on FSO-based networks, there is a gap in understanding dynamic jamming models and their impact on system resilience. Most existing research focuses on traditional static jammer models, often considering basic performance metrics like BER and outage probability in the presence of a jammer. However, evolving and sophisticated jamming strategies, especially in UAV and OIRS-assisted FSO-based networks, require further investigation. In particular, adaptive mitigation techniques, such as dynamic power control, adaptive beamforming, and interference cancellation, have yet to be explored in the context of UAV and OIRS-assisted FSO-based networks. Furthermore, energy-efficient jamming mitigation solutions are needed to ensure sustainable network operation.

While there have been significant advancements in the research on FSO-based networks, UAV and OIRS-assisted communication, and hybrid systems, several critical research gaps remain. Addressing these gaps, ranging from environmental modeling and dynamic jamming mitigation to throughput efficiency and long-term scalability, will be essential for unlocking the full potential of UAV and OIRS-assisted FSO-based networks in the context of emerging 6G communication networks.

2.6 Practical Applications of FSO-based Communication Networks

The proposed FSO-based communication architecture is designed to address the growing need for flexible, high-speed, and resilient wireless communication. Its real-world relevance spans several domains in both civilian and defense sectors, aligning with the key demands of future 6G networks and beyond.

- Rural and Remote Area Connectivity: Many geographically remote or rural areas lack access to high-capacity communication infrastructure. Deploying fiber or RF systems in such regions is often cost-prohibitive. The proposed UAV and OIRS-assisted FSO-based networks provide a flexible alternative by extending FSO-based connectivity, enabling digital inclusion and access to essential services like telemedicine and remote education.

- Emergency and Disaster Response: In the aftermath of natural disasters (e.g., earthquakes, floods, wildfires), terrestrial communication infrastructure may be rendered inoperative. UAVs equipped with OIRS can be rapidly deployed to restore high-speed connectivity by acting as airborne reflectors or relays, facilitating coordination among emergency services and affected populations.

- Temporary and High-Density Events: Large-scale public events such as sports events, concerts, and festivals often experience network congestion due to the temporary spike in demand. UAVs equipped with OIRS can be utilized to dynamically scale communication capacity by providing dedicated high-throughput FSO links, ensuring uninterrupted service quality.

- Military and Tactical Operations: In hostile or remote environments, secure and interference-resistant communication is critical. The directionality and low probability of interception properties of FSO links, combined with the adaptability of OIRS-assisted UAV systems, offer a viable solution for establishing tactical communication networks that are robust against jamming attacks.
- Smart Cities and 6G Infrastructure: OIRS and UAVs are envisioned as integral components of 6G architecture, where intelligent surfaces dynamically shape the communication environment. In smart city deployments, these systems can support high-data-rate applications like intelligent transportation systems, real-time surveillance, and autonomous vehicle coordination.

Chapter 3

Comprehensive Analysis of Hybrid Optical Wireless Communication Architectures

In the conventional FiWi architecture, fiber-based next-generation access technologies are integrated with front-end WiFi networks. However, large-scale deployment of optical fibers in FiWi may not be practical in unconventional scenarios like rugged terrains, remote locations, or urban centers, where additional fiber installation is limited due to high costs or lack of flexibility. Recent advancements in FSO communication offer a viable, cost-effective alternative to optical fibers, especially in areas where fiber installation and trenching are challenging and expensive. Integrating an FSO-based back-end with a WiFi-based front-end in XGPON architecture combines the benefits of both FSO and WiFi, delivering enhanced flexibility and higher data rates. Additionally, LiFi has emerged as a promising complement to WiFi for indoor communication, offering easy deployment and access to a wide, unlicensed spectrum. This chapter explores the benefits and trade-offs of integrating an FSO-based back-end with a LiFi/WiFi front-end. Moreover, we examine the use of LA, which enables users to simultaneously receive data from both WiFi and LiFi access point (AP)s to improve system performance further.

The remainder of the chapter is organized as follows: Section 3.1 provides the motivation for this research and highlights our key contributions. In Section 3.2, we describe the system model for the conventional FiWi architecture and propose various hybrid architectures. Section 3.3 addresses channel modeling for both WiFi and LiFi channels. An analytical expression for the outage probability in the hybrid FoLi architecture is presented in Section 3.4. Section 3.5 discusses the performance evaluations of the proposed architectures, followed by the chapter conclusion.

The work in this chapter resulted in the following publication:

1. P. Singh, A. Gupta, V. A. Bohara and A. Srivastava, “Cost Effective Hybrid FSO-Wireless Architecture for Broadband Access Network," 2022 International Conference on Optical Network Design and Modeling (ONDM), Warsaw, Poland, 2022, pp. 1-6, doi: 10.23919/ONDM54585.2022.9782861.

2. P. Singh, V. A. Bohara and A. Srivastava, “Reliable and Cost Effective All-Optical Wireless Architecture for a Broadband Access network," in Journal of Optical Communications and Networking, vol. 15, no. 2, pp. 98-110, February 2023, doi: 10.1364/JOCN.463574.

3.1 Introduction

Conventional FiWi networks integrate a fiber-based back-end with a WiFi front-end in a PON architecture. Large-scale fiber deployment in conventional FiWi setups may not be feasible in challenging terrains, remote areas, or dense urban centers, where fiber installation is limited due to high costs and low flexibility. A potential solution to these challenges is to introduce FSO links in AON architectures. Unlike PON, AON relies on Ethernet, where an active optical splitter (AOS) equipped with an Ethernet switch is used. This AOS connects multiple optical network unit (ONU)s to the central office through dedicated fiber links, with the Ethernet switch aggregating the traffic from the ONUs and connecting it to the central office via fiber [73].

Recent advancements in FSO technology have made it a cost-effective alternative to optical fiber, particularly in areas where trenching fiber is challenging [1, 31, 36]. In [32], the authors analyzed the performance of an FSO-based PON system with an FSO link between the OLT and passive splitter. In [33], the integration of optical baseband, FSO, and millimeter wave traffic in the PON architecture was explored using OOK signals. Similarly, [34] investigated bidirectional TDM FSO-based PON. Furthermore, in [37], the performance of WDM PON, integrating fiber and FSO links with modulation and detection using modified OOK signals, was examined. A cost analysis of the hybrid PON-FSO approach for fronthaul networks was also conducted in [38], comparing it with standalone PON architectures.

Recent research has also explored the integration of VLC with FSO to leverage the benefits of both technologies. In [74], the authors analyzed the outage probability and BER of a cascaded FSO-VLC system under varying atmospheric conditions, LED counts, and room sizes. In [75], an experimental demonstration of FSO/VLC heterogeneous interconnection for future space-air-ground-ocean-integrated communication was presented. Hybrid FSO/VLC links for user connectivity were demonstrated experimentally in [76]. Additionally, in [77], a decode-and-forward-based VLC-FSO-VLC cooperative system was statistically analyzed for BER and outage probability, while [78] proposed a reinforcement learning algorithm to address load balancing in heterogeneous LiFi-WiFi networks. Furthermore, a Q-learning-based power allocation strategy to optimize transmit power in hybrid RF/VLC networks, ensuring the required QoS, was introduced in [79].

Despite these advancements, the integration of an FSO-based back-end with a LiFi or LA-based front-end in PON/AON architecture has not yet been fully analyzed, nor has its performance under various factors been investigated. Therefore, in this chapter, we evaluate the end-to-end performance of hybrid FSO-based back-end and VLC (LiFi/LA)-based front-end architectures under the impact of channel fading, atmospheric turbulence, and pointing errors. In these architectures, FSO links replace both feeder and distribution fibers in the AON back-end, while users are connected to LiFi APs via VLC links in indoor environments.

3.1.1 Contributions

The major contributions in this chapter can be summarized as:

1. We propose a hybrid FoLi architecture that integrates an FSO-based back-end network with a VLC-based front-end within an AON. The end-to-end performance of the FoLi system is analyzed, taking into

account the impairments in the FSO channel. Furthermore, we derive a closed-form expression for the outage probability of the hybrid FoLi architecture by determining the PDF and CDF of the instantaneous SNR.

2. As a performance benchmark, we also investigate two alternative integration architectures: hybrid FiLi and FoWi. In these configurations, fiber and FSO-based back-ends are integrated with LiFi and WiFi-based front-ends, respectively. Furthermore, we explore the performance enhancement of AON by incorporating LA in the front-end network. With LA, users are able to receive data concurrently from both LiFi and WiFi APs, further improving the efficiency of the system.

3. We compare the end-to-end performance of the proposed architectures with the conventional FiWi architecture across various metrics, including average throughput, fairness, CAPEX and cost per bit. Furthermore, we conduct a reliability analysis of the proposed FoLi architecture using probabilistic modeling and benchmark its performance against the conventional FiWi architecture.

3.2 System Model

We compare the performance of six architectures such as FoLi, FoWi, FiLi, FoLA, FiLA, and conventional FiWi architecture. These architectures are described in detail in the subsequent subsections.

3.2.1 FiWi Architecture

Fig. 3.1 (a) illustrates the conventional FiWi network, which consists of an optical fiber-based XGPON back-end and a WiFi-based front-end network. In this FiWi architecture, the OLT is located at the central office and is connected to a passive optical splitter via a feeder fiber. The splitter, in turn, connects multiple ONUs through distribution fibers. These ONUs are colocated with APs, providing wireless connectivity to end users. XGPON employs time division multiple access (TDMA) for upstream and TDM for downstream traffic management. For indoor communication, we consider a room-sized 10 m $\times$ 10 m $\times$ 3 m, where a single WiFi AP provides coverage. It is assumed that U mobile users are uniformly distributed within the coverage area of the WiFi AP.

3.2.2 FoLi Architecture

In this architecture, FSO based XGPON back-end network is connected to LiFi based front-end access network as shown in Fig. 3.1 (b). In the FoLi architecture, it is assumed that OLT consists of a LD for generating an optical signal. The optical signal is transmitted to the ONUs through optical distribution network (ODN). In ODN, each ONU is connected to the AOS through FSO link, whereas the AOS is connected to OLT using another FSO link. At the ONUs, PDs are employed to receive optical signals. Further, the ONU is connected/colocated with LiFi APs. As shown in Fig. 3.1 (b), we have considered four LiFi APs are install LED inside the room to provide high data rate connectivity to the users present inside the room.

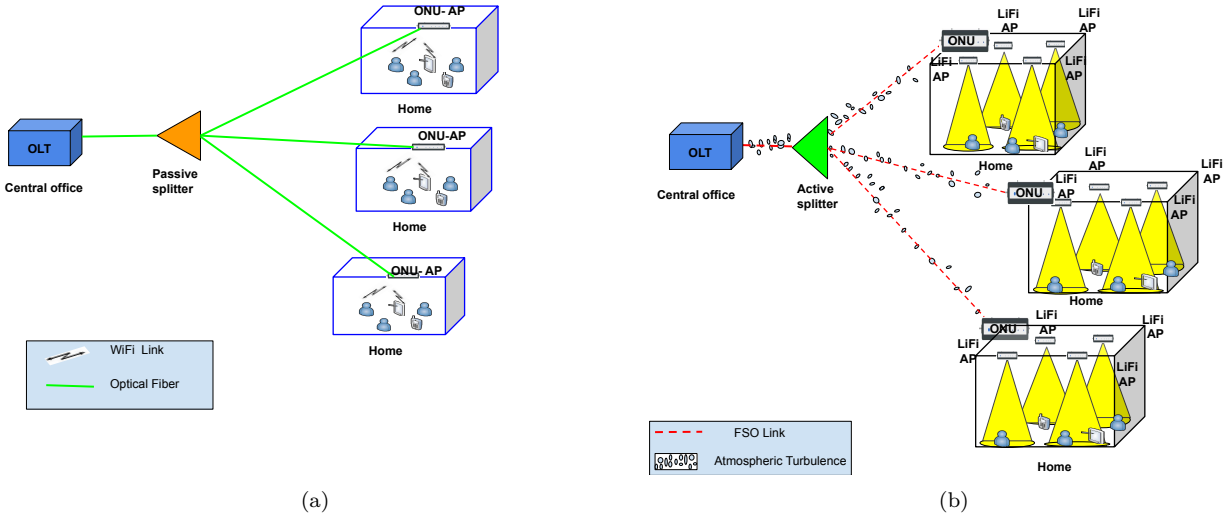

Figure 3.1: (a) Conventional FiWi architecture (b) Proposed FoLi architecture

3.2.3 FoWi Architecture

As illustrated in Fig. 3.2 (a), the FoWi architecture connects the OLT to an AOS via an FSO link, with the AOS further connected to ONUs through another FSO link within the ODN. In this setup, the OLT uses an LD to generate the optical signal, which is transmitted to the ONUs via the FSO-based ODN. At the ONUs, PDs receive and process the optical signal. Each ONU is then connected or colocated with a WiFi AP. For indoor communication, a single WiFi AP is assumed to provide seamless wireless connectivity to the users in the room.

3.2.4 FiLi Architecture

This architecture integrates an optical fiber-based back-end with an LiFi-based front-end access network. As depicted in Fig. 3.2 (b), the OLT is connected to a passive optical splitter via feeder fiber. In the ODN, the passive splitter is linked to ONUs through distribution fibers. In the front-end network, similar to the FoLi architecture, each ONU is colocated with and connected to four LiFi APs within the indoor environment.

3.2.5 FoLA Architecture

Since LiFi and WiFi operate in separate, non-overlapping frequency bands, they can coexist and complement each other effectively. In the LA scheme, both WiFi and LiFi APs are connected to a central controller (CC) via an error-free link. This setup allows users to receive data simultaneously from both WiFi and LiFi APs using the LA scheme [78], [80]. The proposed FoLA system incorporates the LA scheme to enhance overall system performance, particularly in terms of average throughput and fairness. In the system diagram (Fig. 3.2 (c)), the OLT connects to a splitter through an FSO link, and the splitter, in turn, connects to the ONUs via another FSO link. Additionally, an ONU connects to the CC to implement the LA scheme for WiFi and LiFi APs within the room. Similar to the FoLi and FiLi architectures, the room is equipped with four LiFi APs

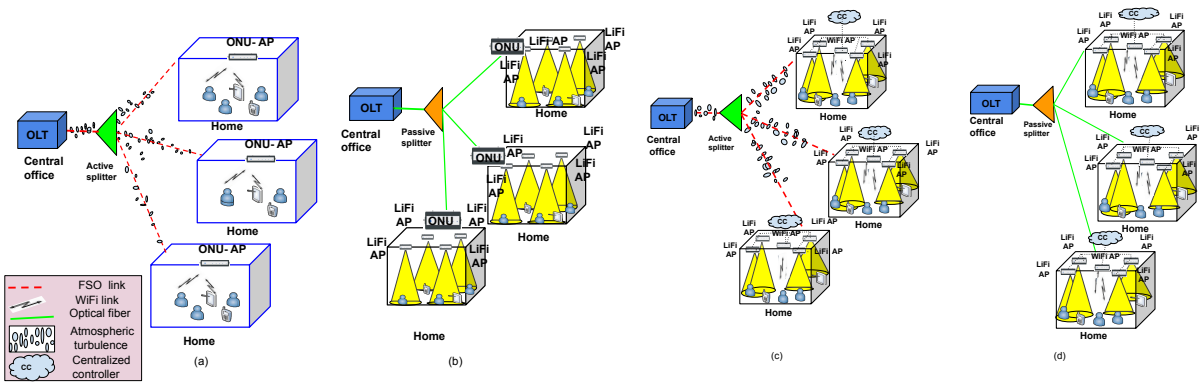

Figure 3.2: System model for (a) FoWi (b) FiLi (c) FoLA (d) FiLA

and a single WiFi AP. Users with LA capabilities can access data from both WiFi and LiFi APs concurrently through the CC.

3.2.5.1 Algorithm 3.1 for Link Aggregation

We have incorporated the LA scheme into both FiLA and FoLA architectures, as detailed in [80]. In this setup, LA-enabled users can aggregate data from both WiFi and LiFi access points simultaneously. We assume that the LiFi and WiFi receivers in LA-enabled users operate independently. To account for practical implementation effects, we have introduced an average LA overhead, denoted as β_{oh}. According to the literature [81], β_{oh} is typically valued at 0.8.

Algorithm 3.1 LA Algorithm

1: Input:Given the total number of the users, U.
2: **for** $u = 1, ...,U$ **do**
3: Calculate data rate for each LA enabled user

$$D_u^{LA} = \beta_{oh} \times (D_u^{\text{WiFi}} + D_u^{\text{LiFi}}),$$

4: **end for**

3.2.6 FiLA Architecture

As depicted in Fig. 3.2 (d), the LA scheme, similar to the FoLA architecture, is integrated into the front-end access network of the FiLA architecture, which utilizes a fiber-based back-end network. In the ODN setup, a feeder fiber links the OLT to a passive splitter, which then distributes the signal to ONUs via distribution fibers.

3.3 Channel Model

This section outlines the channel model used for front-end access networks, including WiFi and LiFi, and the various factors influencing their performance. For the performance evaluation of different hybrid architectures,

the FSO channel modeling, introduced in Chapter 2, is also utilized in this Chapter. The FSO channel model accounts for attenuation due to absorption and scattering, turbulence caused by random refractive index fluctuations, and pointing errors resulting from misalignment between transmitter and receiver apertures. The FSO link is treated as a fading channel influenced by atmospheric turbulence (h_{at}), pointing error (h_p), and atmospheric attenuation (h_a). Atmospheric turbulence is modeled as a random process following a Gamma-Gamma distribution, with its corresponding PDF provided in Chapter 2.

3.3.1 WiFi Channel Model

In this subsection, the path loss model used for modeling the WiFi channel in the indoor space is expressed as [82]

$$PL(d) = \begin{cases} PL_{\text{FS}}(d) + \mu_\sigma, & d \leq d_{\text{BP}}, \\ PL_{\text{FS}}(d) + 35\log_{10}\left(\dfrac{d}{d_{\text{BP}}}\right) + \mu_\sigma, & d > d_{\text{BP}}, \end{cases} \tag{3.1}$$

where d corresponds to the distance between the WiFi AP and uth user, d_{BP} denotes the distance between the breakpoint, $\mu_\sigma \sim \mathcal{N}(0, \sigma^2)$. The path loss in free space, PL_{FS} is given as

$$PL_{\text{FS}}(d) = 20\log_{10}(d) + 20\log_{10}(f_c) - 147.5, \tag{3.2}$$

where f_c denotes carrier frequency. Further, we also consider multipath propagation in wireless access channels, which is expressed as

$$G_{\text{WiFi}} = \sqrt{\frac{K}{K+1}}e^{j\phi} + \sqrt{\frac{1}{K+1}}\mu_1, \tag{3.3}$$

where $\mu_1 \sim \mathcal{N}(0, 1)$. The arrival/departure angle of the LoS signal is denoted by ϕ. We have also assumed that before the breakpoint, the Rician factor K is equal to one, and after the breakpoint, K is equal to zero. The channel gain between uth user and WiFi AP is represented as H^u_{WiFi}, and it is calculated as [82]

$$H^u_{\text{WiFi}} = |G_{\text{WiFi}}|^2 \, 10^{-\frac{PL(d)}{10}}, \tag{3.4}$$

where G_{WiFi} is WiFi channel response and PL is path loss of the multipath propagation in WiFi channel. Therefore, the SNR of uth user is given as

$$\text{SNR}^u_{\text{WiFi}} = \frac{H^u_{\text{WiFi}} P_T^{\text{WiFi}}}{N_{\text{WiFi}} \mathcal{B}_{\text{WiFi}}}, \tag{3.5}$$

where P_T^{WiFi} indicates transmit power of WiFi AP, N_{WiFi} denotes power spectral density (PSD) of noise in WiFi channel, and $\mathcal{B}_{\text{WiFi}}$ represents the bandwidth of WiFi AP. The data rate achieved by uth user from WiFi AP can be calculated as given in [82]

$$D_u^{\text{WiFi}} = \varepsilon_u \Upsilon_u \mathcal{B}_{\text{WiFi}}. \tag{3.6}$$

where ε_u corresponds to the fraction of the transmission time that WiFi AP spends on uth user and Υ_u indicates spectral efficiency of the uth user from WiFi AP. Since we consider a single WiFi AP in the room, there will be no interference from other WiFi APs.

3.3.2 LiFi Channel Model

For the indoor LiFi channel model given in [83], we assumed that the LED is deployed at a height L_h from the uth user. The angle of incidence and angle of irradiance are denoted by φ_u and θ_u, respectively. LED's maximum radius can be expressed as $r_e = L_h \tan \Phi_{1/2}$, where $\Phi_{1/2}$ is semi-angle of LED. The LED follows Lambertian emission pattern with emission order m defined as $m = -1/\log_2 \cos \Phi_{1/2}$. The LiFi channel gain of LoS link between uth user and LED is expressed as.

$$H^u_{\text{LiFi}} = \frac{A_{PD}(m+1)\Re}{2\pi {d_u}^2} \cos^m(\theta_u) G(\varphi_u) g(\varphi_u) \cos(\varphi_u), \tag{3.7}$$

where A_{PD} represents PD area, $\Re$ denotes responsivity of PD, d_u represents Euclidean distance between LED and uth user. The PD area is modeled as an active area A_{PD} that collects radiation incident at angles φ_u less than the PD's FoV, Ψ_{FOV}. The effective collection area of the PD is given by

$$A_{eff}(\varphi_u) = \begin{cases} A_{PD}\cos(\varphi_u), & 0 \le \varphi_u \le \pi/2 \\ 0, & \varphi_u > \pi/2, \end{cases} \tag{3.8}$$

The gain of the optical filter is denoted by $G(\varphi_u)$, and the gain of the optical concentrator $g(\varphi_u)$ is given by [83].

$$g(\varphi_u) = \begin{cases} \dfrac{RI^2}{\sin^2(\Psi_{FOV})}, & 0 \le \varphi_u \le \Psi_{FOV} \\ 0, & \varphi_u > \Psi_{FOV}, \end{cases} \tag{3.9}$$

where RI denotes the refractive index. According to geometrical representation of LoS VLC link, $\cos(\varphi_u) = L_h/d_u = L_h/\sqrt{r_u^2 + L_h^2}$ and $\cos(\theta_u) = L_h/\sqrt{r_u^2 + L_h^2}$, where r_u representing horizontal separation distance between LED and the uth user respectively. After substituting all these values in (3.7), LiFi channel gain can be rewritten as

$$H^u_{\text{LiFi}} = \frac{I(m+1)L_h^{m+1}}{(r_u^2 + L_h^2)^{\frac{m+3}{2}}}, \tag{3.10}$$

where $I = \frac{1}{2\pi} A_{PD} \Re G(\varphi_u) g(\varphi_u)$ is constant term.

The PDF of gain of LiFi link between LED and uth user can be obtained as mentioned in [83]

$$f_{H^u_{\text{LiFi}}}(H) = \frac{2(I(m+1)L_h^{m+1})^{2/m+3}}{r_e^2(m+3)} H^{-(2/m+3)-1}. \tag{3.11}$$

The PDF of the instantaneous SNR (γ_{LiFi}) is given as [83]

$$f_{\gamma_{\text{LiFi}}}(\gamma) = \frac{\bar{\gamma}_{\text{LiFi}}^{\frac{1}{m+3}}}{r_e^2(m+3)} (I(m+1)L_h^{m+1})^{2/m+3} \gamma^{-\frac{m+4}{m+3}}, \tag{3.12}$$

where $\bar{\gamma}_{\text{LiFi}}$ denotes average electrical SNR.

We assume that all LiFi links are independent and identically distributed random variables. By applying Binomial approximation, the CDF of the instantaneous SNR for best LiFi link for uth user is expressed as [83]

$$F_{\gamma_{\text{LiFi}}}(\gamma) = \upsilon^{N_{\text{L-AP}}} - N_{\text{L-AP}} \upsilon^{N_{\text{L-AP}}-1} \chi \left(\frac{\gamma}{\bar{\gamma}_{\text{LiFi}}}\right)^{-1/m+3}, \tag{3.13}$$

where $\upsilon = (1 + \frac{L_h^2}{r_e^2})$, $\chi = \frac{1}{r_e^2}(I(m+1)L_h^{m+1})^{2/m+3}$, and $N_{\text{L-AP}}$ denotes the number of LiFi APs. We also assume that the users are connected to one LiFi AP and will experience interference from remaining LiFi APs.

Therefore, signal to interference plus noise ratio (SINR) of the signal received by uth user from lth LiFi AP is given as [82]:

$$\mathrm{SINR}_{\mathrm{LiFi}}^{i,u} = \frac{(\Re H_{\mathrm{LiFi}}^{l,u} P_T^{\mathrm{LiFi}}/\wp)^2}{N_{\mathrm{LiFi}}\mathcal{B}_{\mathrm{LiFi}} + \sum_{j\neq l}(\Re H_{\mathrm{LiFi}}^{j,u} P_T^{\mathrm{LiFi}}/\wp)^2}, \tag{3.14}$$

where $H_{\mathrm{LiFi}}^{l,u}$ is LiFi channel gain between lth LiFi AP and uth user and P_T^{LiFi} is transmit optical power per LiFi AP. Data rate achieved by uth user from lth LiFi AP can be calculated as in [82]

$$D_u^{\mathrm{LiFi}} = \varepsilon_u \Upsilon_u \mathcal{B}_{\mathrm{LiFi}}, \tag{3.15}$$

where $\mathcal{B}_{\mathrm{LiFi}}$ represents the bandwidth of LiFi AP. Given the SINR of the users, the modulation and coding scheme (MCS) is used to determine their spectral efficiency Υ_u. The relationship between SINR, MCS, and spectral efficiency Υ_u is summarized in [82].

3.4 Statistical Characteristics of the Equivalent SNR of End-to-End Link of FoLi Architecture

We derive mathematical expressions for the PDF and CDF of the SNR for the end-to-end link in the proposed FoLi architecture. In this architecture, the OLT is connected to an AOS via an FSO link, while another FSO link connects the AOS to the ONU. Consequently, the signal received at the AOS is expressed as follows:

$$Y_{OLT,splitter} = \zeta_1 h_{FSO_1} x_1 + n_{01}, \tag{3.16}$$

where ζ_1 represents optical-to-electrical conversion ratio of OLT-AOS FSO link, x_1 denotes optical signal transmitted by laser diodes from the OLT, $n_{01} \sim \mathcal{N}(0, \sigma_{n_{01}}^2)$ denotes the additive white Gaussian noise (AWGN) with zero mean and variance $\sigma_{n_{01}}^2$ [22], and h_{FSO_1} denotes channel fading level of FSO link due to atmospheric loss, atmospheric turbulence, and pointing error. The optical signal received at ιth ONU is expressed as

$$Y_{splitter,ONU_m} = \zeta_2 h_{FSO_2}^m \hat{x_2} + n_{02}, \tag{3.17}$$

where ζ_2 represents optical-to-electrical conversion ratio of AOS-ιth ONU FSO link, $\hat{x_2}$ denotes estimated signal at ιth ONU, $n_{02} \sim \mathcal{N}(0, \sigma_{n_{02}}^2)$, and $h_{FSO_2}^m$ denotes FSO channel gain between AOS and ιth ONU. At the user, the PD transforms the optical signal into electrical signal and the signal received at uth user is given as

$$Y_{user_u} = \zeta_3 H_{\mathrm{LiFi}}^{l,u} \hat{x_3} + n_{03}, \tag{3.18}$$

where ζ_3 represents optical-to-electrical conversion ratio of ιth ONU-uth user VLC link, $\hat{x_3}$ denotes decoded signal at uth user, $n_{03} \sim \mathcal{N}(0, \sigma_{n_{03}}^2)$, and $H_{\mathrm{LiFi}}^{l,u}$ denotes LiFi channel gain of VLC link between lth LiFi AP and uth user.

3.4.1 Cumulative Distribution Function

The equivalent SNR of the end-to-end link of the proposed FoLi architecture is expressed as [84]

$$\gamma_{FoLi} \triangleq \min\left\{\gamma_{FSO_1},\ \gamma_{FSO_2},\ \gamma_{\mathrm{LiFi}}\right\}, \tag{3.19}$$

where γ_{FSO_1} is the SNR of FSO link between OLT and AOS, γ_{FSO_2} is the SNR of FSO link between the AOS and ιth ONU. As mentioned before, ONU is colocated/connected with LiFi AP. Therefore, γ_{LiFi} is the SNR of LiFi link between LiFi AP and uth user. Finally, the CDF of SNR γ_{FoLi} of end to end link of the proposed FoLi architecture is expressed as

$$F_{\gamma_{FoLi}}(\gamma) = 1 - \left[\left(1 - F_{\gamma_{FSO_1}}(\gamma)\right) \times \left(1 - F_{\gamma_{FSO_2}}(\gamma)\right) \times \left(1 - F_{\gamma_{\text{LiFi}}}(\gamma)\right)\right], \tag{3.20}$$

where $F_{\gamma_{FSO_1}}$ denotes the CDF of the SNR of FSO link between OLT and the AOS, $F_{\gamma_{FSO_2}}$ denotes the CDF of the FSO link between the AOS and ιth ONU. With the assumption that FSO and LiFi links are independent, we get the expression for CDF of the SNR of the end-to-end link of FoLi architecture by substituting (2.7) and (2.8) in (3.20) as shown in (3.21).

$$\begin{aligned} F_{\gamma_{FoLi}}(\gamma) = 1 - \Bigg[& \left(1 - \frac{2\xi_1^2}{\Gamma(\alpha_{f_1})\Gamma(\beta_{f_1})} G_{2,4}^{3,1}\left(\frac{\alpha_{f_1}\beta_{f_1}\wp_1}{\bar{\gamma}_{FSO_1}}\gamma \middle| \begin{matrix} 1, \xi_1^2+1 \\ \xi_1^2, \alpha_{f_1}, \beta_{f_1}, 0 \end{matrix}\right)\right) \\ & \times \left(1 - \frac{2\xi_2^2}{\Gamma(\alpha_{f_2})\Gamma(\beta_{f_2})} G_{2,4}^{3,1}\left(\frac{\alpha_{f_2}\beta_{f_2}\wp_2}{\bar{\gamma}_{FSO_2}}\gamma \middle| \begin{matrix} 1, \xi_2^2+1 \\ \xi_2^2, \alpha_{f_2}, \beta_{f_2}, 0 \end{matrix}\right)\right) \\ & \times \left(1 - \upsilon^{N_{\text{L-AP}}} - N_{\text{L-AP}}\upsilon^{N_{\text{L-AP}}-1}\chi\left(\frac{\gamma}{\bar{\gamma}_{\text{LiFi}}}\right)^{-1/m+3}\right)\Bigg], \end{aligned} \tag{3.21}$$

In (3.21), ξ_1 and ξ_2 denote pointing error coefficient for FSO link between OLT and the AOS, and between the AOS and ιth ONU, respectively.

3.4.2 Probability Density Function

The PDF of the SNR of the end-to-end link of FoLi architecture can be obtain by differentiating (3.20) as

$$\begin{aligned} f_{\gamma_{FoLi}}(\gamma) = & [f_{\gamma_{FSO_1}}\left(1 - F_{\gamma_{FSO_2}}(\gamma)\right)\left(1 - F_{\gamma_{\text{LiFi}}}(\gamma)\right)] + [f_{\gamma_{FSO_2}}\left(1 - F_{\gamma_{FSO_1}}(\gamma)\right)\left(1 - F_{\gamma_{\text{LiFi}}}(\gamma)\right)] + \\ & [f_{\gamma_{\text{LiFi}}}\left(1 - F_{\gamma_{FSO_1}}(\gamma)\right)\left(1 - F_{\gamma_{FSO_2}}(\gamma)\right)]. \end{aligned} \tag{3.22}$$

where $f_{\gamma_{FSO_1}}$ denotes the PDF of the SNR of the FSO link between OLT and the AOS, $f_{\gamma_{FSO_2}}$ denotes the PDF of the FSO link between the AOS and ιth ONU. The closed form expression of the PDF for the SNR of the end-to-end link of the proposed FoLi architecture can be obtained by substituting (2.7), (2.8), (3.12), and (3.13) in (3.22).

3.5 Results and Discussion

To evaluate the performance of the end-to-end links for the proposed FoLi, FoWi, FiLi, FoLA, FiLA, and FiWi architectures, we employed the VPI Transmission Maker simulation software [85], a powerful tool for designing and analyzing optical networks and their components. Since this tool cannot assess optical signals propagating outside the optical fiber, we utilized VPI's co-simulation capability with MATLAB to analyze signals in free space. For the FSO-based back-end architecture, we assumed the use of an optical source operating at a 1550 nm wavelength at the OLT to generate 10 Gbps OOK data. These data are encoded

Table 3.1: Simulation parameters utilized in fiber and FSO-based architectures

Parameters	Simulation values
Optical Fiber and FSO Channel	
L_F (feeder and distribution section)	2 and 4 Km
P_T	17.78 dBm
a	30 cm
C_n^2 (Weak turbulence)	8×10^{-15} m$^{-2/3}$
C_n^2 (Moderate turbulence)	2×10^{-14} m$^{-2/3}$
C_n^2 (High turbulence)	1×10^{-13} m$^{-2/3}$
Attenuation coefficient of optical fiber	0.2 dB/km
ζ	0.5 A/W
σ_j	30 cm
k_l	0.43
$\sigma_{n_{01}}^2$, $\sigma_{n_{02}}^2$	10^{-14}
WiFi Channel	
User height above floor level	0.85 m
σ (before d_{BP})	3 dB
σ (after d_{BP})	5 dB
d_{BP}	5 m
f_c	2.4 GHz
$\mathcal{N}_{\mathrm{WiFi}}$	-174 dBm/Hz
P_T^{WiFi}	20 dBm
$\mathcal{B}_{\mathrm{WiFi}}$	20 MHz
LiFi Channel	
A_{PD}	1 cm^2
RI	1.5
$\Phi_{1/2}$	60^o
$G(\varphi)$	1
Ψ_{FOV}	90^o
$\Re$	0.53 A/W
P_T^{LiFi}	3 watt
$\wp$	3
$\mathcal{B}_{\mathrm{LiFi}}$	20 MHz
$N_{\text{L-AP}}$	4
$\mathcal{N}_{\mathrm{LiFi}}$	$10^{-21}A^2/Hz$

by a mach zehnder modulator (MZM) and transmitted over an FSO link with a length of 2 km, where it is received by an active/passive splitter. The splitter then connects to 16 ONUs via dedicated FSO links of 4 km. Each ONU converts the optical signal into an electrical signal using a PD. It is assumed that these ONUs are co-located with WiFi/LiFi access points in a room measuring 10 m $\times$ 10 m $\times$ 3 m . The users in the room are distributed according to a uniform probability distribution. To evaluate the performance of the FiWi and FoWi architectures, a single WiFi AP is used to cover the indoor space. In contrast, the FiLi and FoLi architectures utilize 4 LiFi APs to cover the room. The FoLA and FiLA architectures employ 4 LiFi APs and

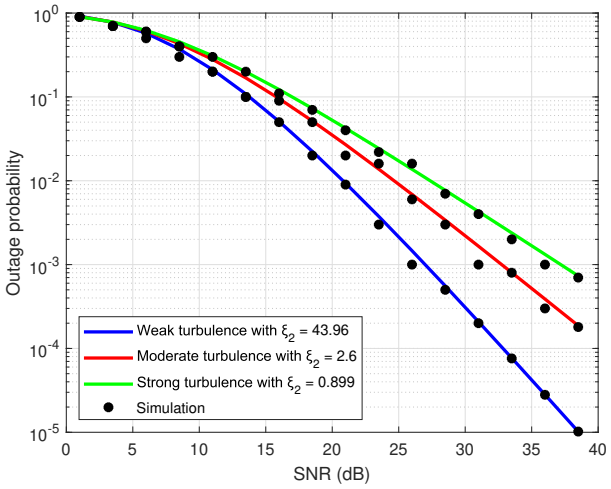

Figure 3.3: Outage probability of FoLi architecture over weak, moderate, and strong turbulence with pointing errors

a single WiFi AP to provide connectivity to all users within the room. The major simulation parameters are listed in Table 3.1.

3.5.1 Outage Analysis

In this subsection, we have analyzed the end-to-end outage probability specifically for FoLi architecture. When the instantaneous SNR of the end-to-end FoLi architecture falls below the SNR threshold γ_{th}, FoLi will suffer an outage. Since no data is received by the user when SNR falls below γ_{th}, the outage probability can be given as $P_{out} = Pr[\gamma_{FoLi} < \gamma_{th}]$. Fig. 3.3 illustrates the outage probability of the end-to-end FoLi architecture as a function of SNR, considering the effects of atmospheric loss, turbulence, and pointing error. The numerical and simulation results align well, validating the analytical derivations provided in (3.21). It is evident that the outage probability is higher under strong and moderate turbulence compared to weak turbulence. Additionally, increased pointing errors in the FSO link led to a greater outage for the FoLi system. For example, an outage probability of 10^{-1} is achieved at a SNR of 14 dB in weak turbulence with minimal pointing error ($\xi_2 = 43.96$). In contrast, this outage probability occurs at 16 dB SNR under moderate turbulence with medium pointing error ($\xi_2 = 2.6$) and at 17 dB SNR under strong turbulence with high pointing error ($\xi_2 = 0.899$). Furthermore, in weak turbulence with small pointing error, an outage probability of 10^{-3} is achievable at 26 dB SNR, while in strong turbulence with large pointing error, the same outage probability requires 37 dB SNR. Moreover, more pointing errors in the FSO link result in greater outages of the proposed FoLi architecture. At 10 dB SNR, the outage probabilities for weak, moderate, and strong turbulence are 0.3, 0.4, and 0.44, respectively.

3.5.2 Performance Comparison

In this subsection, we compare the simulation results of the proposed FoLi, FoWi, FiLi, FoLA, and FiLA architectures with those of the conventional FiWi architecture, focusing on the average data rate and fairness. In addition, we evaluate and compare the CAPEX of these hybrid architectures.

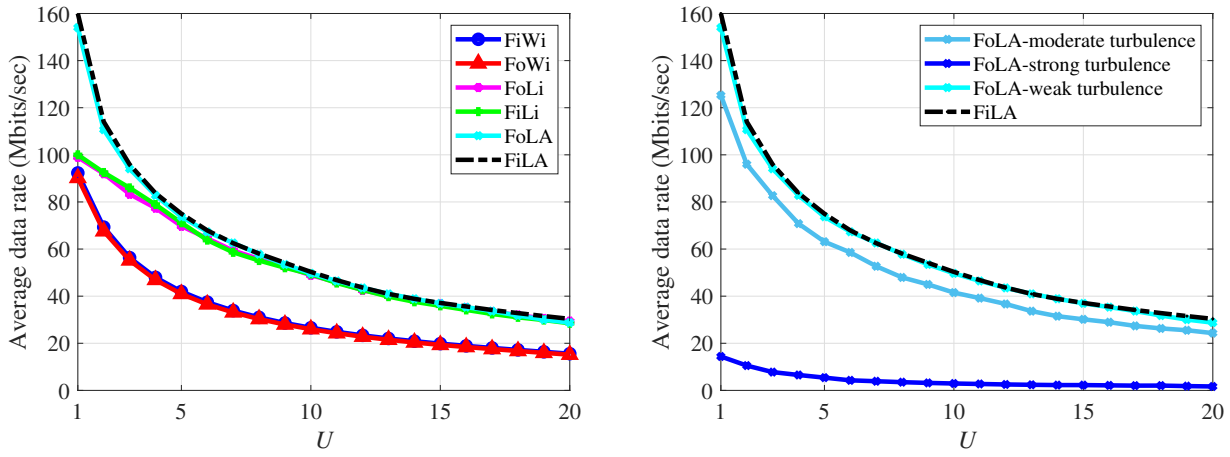

Figure 3.4: (a) Average data rate versus the number of users U. (b) Average data rate versus the number of users U under the impact of atmospheric turbulence.

3.5.2.1 Average Data Rate

Fig. 3.4 (a) shows the average data rate per user as a function of the number of users U for the proposed architectures and the conventional FiWi architecture. As illustrated, the average data rate per user in the downlink decreases with an increase in U. The FiLA architecture outperforms the other hybrid architectures under weak turbulence with minimal pointing error ($\xi_2 = 43.96$). Furthermore, the FiLA and FoLA architectures deliver higher average data rates per user compared to FiLi and FoLi for $N < 10$. However, for $N > 10$, the performance of the FiLi, FoLi, FiLA, and FoLA architectures tends to saturate. The architectures with LiFi and LA front-ends—namely FiLi, FoLi, FiLA, and FoLA—outperform FiWi and FoWi in terms of average data rate, particularly under weak turbulence with lower pointing error. Under ideal atmospheric conditions, under weak turbulence with lower pointing error, the performance of architectures employing FSO in the backhaul is nearly equivalent to those using fiber, particularly when the same front-end access technology is used. This indicates that, in the absence of atmospheric conditions impairments, FSO can serve as a viable alternative to fiber for broadband access.

Fig. 3.4 (b) compares the FiLA and FoLA architectures under weak, moderate, and strong turbulence conditions. It is evident that as the strength of the turbulence increases, the average data rate per user for the FoLA architecture deteriorates relative to the FiLA architecture. The performance of the FoLA architecture under weak turbulence is quite close to that of the FiLA architecture. To mitigate the effects of moderate or strong atmospheric turbulence, implementing spatial diversity techniques, such as repetition coding [86] or orthogonal space-time block codes [87], can be effective. Fig. 3.5 illustrates the complementary cumulative distribution function (CCDF) of user data rates for the different proposed architectures. It can be observed that 50% of users achieve data rates exceeding approximately 26 Mbps and 24 Mbps in the FiWi and FoWi architectures, respectively, indicating better performance in the FiWi configuration under the considered conditions. In contrast, 50% of users in the FoLi, FiLi, FoLA, and FiLA architectures achieve data rates above 46 Mbps. Thus,

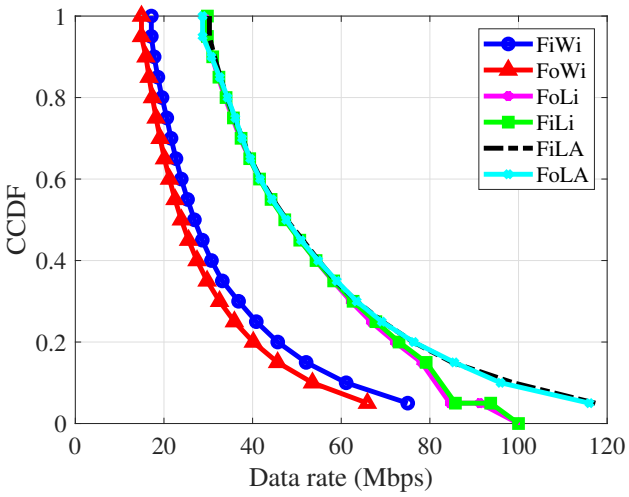

Figure 3.5: CCDF of user's data rate (Mbps) for different proposed architectures and the conventional FiWi architectures.

the CCDF plot indicates that these architectures perform better than FiWi and FoWi. Notably, for smaller numbers of users, FiLA and FoLA perform significantly better than FoLi and FiLi.

3.5.2.2 Fairness Analysis

To compare the performance of the proposed architectures with the conventional FiWi architecture, we have assessed the proposed architectures in terms of fairness. For this analysis, we used Jain's fairness index to measure user fairness, as described in [88].

$$J = \frac{\left(\sum_{u=1}^{U} D_u\right)^2}{U \sum_{u=1}^{U} D_u^2}, \tag{3.23}$$

where D_u represents the individual data rate achieved by the uth user and U denotes the number of users. Fig 3.6 shows that the FiLi, FoLi, FiLA, and FoLA architectures provide better fairness among users compared to the FiWi and FoWi architectures. Specifically, LA-based front-end architectures such as FoLA and FiLA achieve full fairness when $U = 3$. However, as U increases, the fairness between users decreases. For $U = 20$, the LiFi and LA-based front-end architectures—namely FoLi, FiLi, FoLA, and FiLA—attain a fairness index greater than 0.8, in contrast to FiWi and FoWi. Furthermore, FiLA and FoLA outperform LiFi -based front-end architectures such as FiLi and FoLi in terms of fairness. For $U = 10$, FiLA and FoLA achieve a fairness index of 0.94, whereas FiLi and FoLi achieve a fairness index of 0.92.

3.5.2.3 Cost Analysis

We conducted a cost analysis for the proposed hybrid architectures—FoLi, FiLi, FoLA, FiLA—as well as the conventional FiWi architecture, all using the same split ratios. For this analysis, we assumed a split ratio of

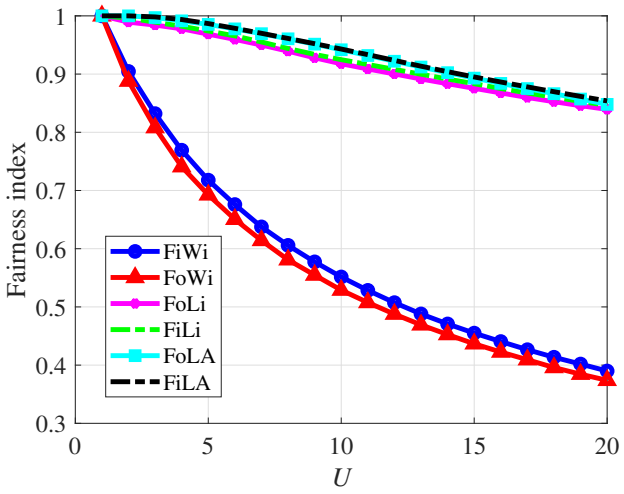

Figure 3.6: Fairness index versus the number of users

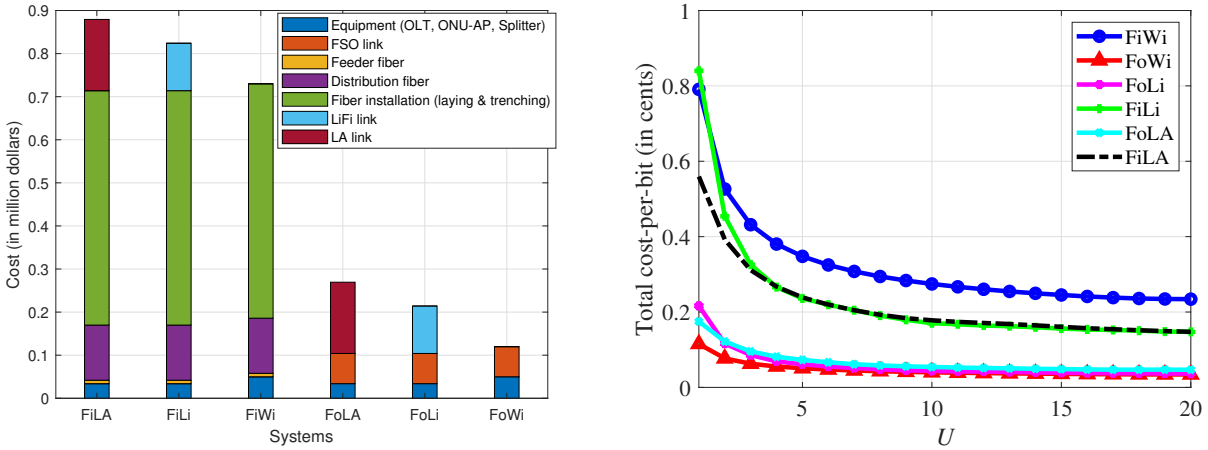

(a) (b)

Figure 3.7: (a) Total deployment cost of the proposed architectures and FiWi architecture. (b) Total cost-per-bit versus the number of users U.

1 : 16. The CAPEX of FiWi architectures C_{FiWi} is given as [89]:

$$C_{\text{FiWi}} = C_{OLT} + C_{splitter} + L_{ff}C_{ff} + \sum_{m \epsilon N_{ONU-AP}} L_{df}^{m} C_{df} + N_{ONU-AP} C_{ONU-AP}, \tag{3.24}$$

where C_{OLT} is the cost of the OLT, $C_{splitter}$ is the cost of the splitter, L_{ff} is the length of the feeder fiber length, C_{ff} is the cost of feeder fiber per kilometer, L_{df}^{m} is distribution fiber length between splitter and ιth ONU, C_{df} is the cost of distribution fiber per kilometer, N_{ONU-AP} is the number of ONU-APs, and C_{ONU-AP} is cost of ONU-AP. For the proposed architectures such as FoWi, FiLi, FoLi, FiLA, and FoLA, equation (3.24) can be adjusted to calculate the CAPEX, C_{PA}, as follows:

$$C_{PA} = C_{OLT} + C_{splitter} + C_{FSO_1} + \sum_{m \epsilon N_{ONU-Eq}} C_{FSO_2}^{m} + N_{ONU-Eq} C_{ONU-Eq}, \tag{3.25}$$

where C_{FSO_1}, $C_{FSO_2}^{m}$ represent the costs of the FSO link between the OLT and the splitter, and between the splitter and the ιth ONU, respectively. N_{ONU-Eq} is the number of equipment units, such as ONU-AP, LiFi-AP, or LA-AP, C_{ONU-Eq} denotes the cost of each type of equipment. Fig. 3.7 (a) compares the total deployment costs of the proposed architectures—FoWi, FiLi, FoLi, FiLA, and FoLA—with the conventional FiWi architecture. For the CAPEX analysis, we utilized the cost values provided in Table 3.2. It is evident that the primary cost component for the conventional FiWi architecture is the fiber infrastructure, including expenses for digging and trenching. Fiber-based back-end architectures, such as FiLA, FiLi, and FiWi, incur high costs for purchasing and installing optical fiber. In contrast, the FoLA, FoLi, and FoWi architectures benefit from reduced fiber and installation costs by employing FSO links in the back-end network. Thus, deploying an FSO-based back-end hybrid architecture can result in nearly 60.9 % savings in CAPEX compared to fiber-based back-end architectures. Fig. 3.7 (b) illustrates the cost efficiency of the proposed architectures—FoLi, FiLi, FoLA, FiLA—and the conventional FiWi architecture, measured in terms of cost-per-bit. Cost-per-bit is defined as the ratio of CAPEX to the architecture's capacity. The inclusion of an FSO link in the back-end of the architecture significantly reduces the cost-per-bit, making the system more cost-effective. Fig. 3.7 (b) clearly shows that FoWi achieves the lowest cost-per-bit at 0.123 cents. However, it also results in the lowest average data rate among the proposed architectures, indicating a trade-off between cost-per-bit and average data rate. Compared to the FoWi architecture, FoLA and FoLi demonstrate better cost-per-bit performance than the fiber-based back-end architectures (FiWi, FiLi, and FiLA).

The cost analysis presented offers valuable insight into the relative CAPEX differences between fiber-based and FSO-based architectures. However, the current evaluation assumes a greenfield deployment scenario, which may not fully reflect practical deployment contexts. In many real-world cases, PONs may already be in place. To address this, Fig 3.8 examines the scenario of upgrading an existing PON to incorporate an FSO-based backhaul. Fig 3.8 indicates that while the ongoing cost of maintaining an existing fiber network is relatively low, the incremental cost of integrating FSO components, LiFi access points, and additional LA links can be even lower. As a result, upgrading with FSO can offer a cost-efficient alternative within a pre-deployed PON framework. Furthermore, the total additional costs associated with FSO-based architectures remain comparable to those of traditional fiber-based solutions. These preliminary findings support the viability of FSO integration

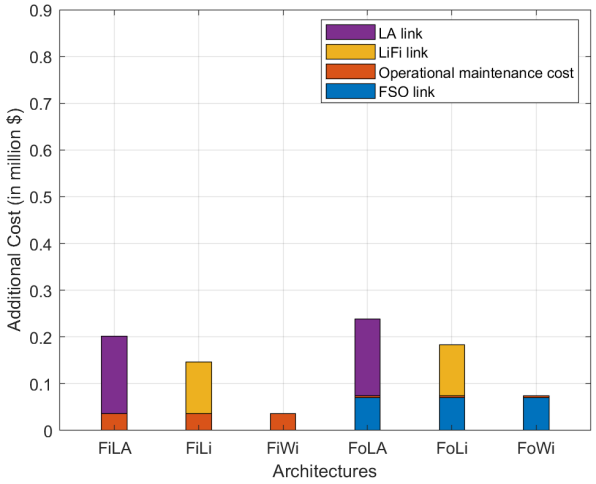

Figure 3.8: Cost comparison under pre-deployed PON framework

as an economical strategy for network expansion or densification, particularly in deployment-constrained areas.

Table 3.2: Cost values of network components

Network Components	Unit cost ($)
OLT	27560
Splitter (1:16)	750
ONU	350
ONU-AP	1350
Fiber (/km)	4000
Fiber laying and trenching (/km)	16000
Operational maintenance cost (annually)	36000
FSO link	4124
Hybrid LiFi and WiFi link (with LA capability)	10337
LiFi link (4 LiFi APs, 4 luminaries, 4 dongles)	6885

3.5.3 Reliability Analysis

In this subsection, we assess the reliability of the proposed FoLi architecture and compare it with the conventional FiWi architecture. In the FiWi architecture, the passive splitter is a more reliable component due to its passive nature [90]. However, the reliability of the conventional FiWi setup can be compromised by link failures such as optical fiber cuts and component failures, including those of the AP and ONU. Similarly, in the proposed FoLi architecture, failures of the FSO link, ONU, AP, and AOS impact its reliability.

Let P_{cut} denote the probability of fiber cuts between the splitter and ONU-AP, and P_F represent the probability of component failures, including those of the ONU, AP, AOS, and FSO link. For evaluating the reliability of both the FiWi and FoLi architectures, we assume a failure probability of 10^{-6} for the ONU, AOS, and AP [91]. Considering advancements in FSO technology, we use a 99.999% availability rate for FSO

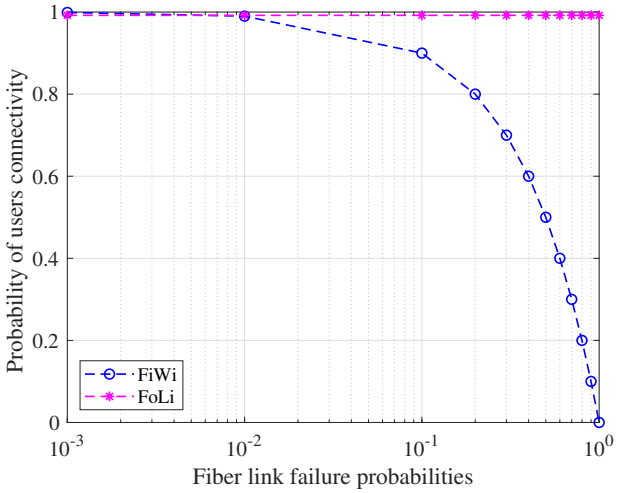

Figure 3.9: Probability of the user's connectivity versus Fiber link failure probabilities

links [92], [93], which translates to a failure probability of 10^{-5} for the FSO link. In the conventional FiWi architecture, the probability of user connectivity to the OLT is given by

$$P_{con}^{U} = (1 - P_{cut}) \times (1 - P_F^O) \times (1 - P_F^{AP}), \tag{3.26}$$

where P_F^O and P_F^{AP} represent the failure probability of ONU and AP, respectively. When fiber is replaced by FSO link and WiFi is replaced by LiFi in the proposed FoLi architecture, the probability of the users connectivity in the case of FSO link, ONU, AOS, and AP failures is depicted in Fig. 3.9 and computed as follows

$$P_{con}^{U} = (1 - P_F^{FSO}) \times (1 - P_F^{AOS}) \times (1 - P_F^{AP}) \times (1 - P_F^O), \tag{3.27}$$

where P_F^{FSO} represents the probability of failure of the FSO link. Figure 3.9 illustrates how the probability of user connectivity to the OLT varies with increasing fiber cut probability in both FiWi and FoLi architectures. It is evident that the FoLi architecture achieves a user connectivity probability of 0.99 when the probability of fiber cut is 0.1, outperforming the FiWi architecture. Thus, the FoLi architecture demonstrates superior reliability compared to FiWi.

3.6 Chapter Summary

This chapter compares the performance of the FiLi, FiLA, FoWi, FoLi, and FoLA architectures with the conventional FiWi architecture. Additionally, we derive and validate a closed-form expression for the outage probability of the FoLi architecture through simulations. The results indicate that FSO-based architectures offer a viable alternative to the conventional FiWi architecture for low-cost and reliable communication, particularly in scenarios where optical fiber installation is impractical. Among FSO-based architectures, FoLA excels in average data rate and fairness. However, when comparing both FSO and fiber-based architectures, FiLA performs better in terms of average data rate and fairness, though it is less cost-effective than FoLA due to the trade-off between data rate and cost efficiency. The findings also show that FoLA remains an attractive option

under weak turbulence conditions compared to the FiWi architecture. For strong or moderate turbulence, the performance of the proposed architectures degrades, but this can be mitigated with the use of appropriate optical amplifiers. Additionally, incorporating FSO links in the back-end network of FSO-based architectures significantly enhances system reliability compared to the FiWi architecture.

Chapter 4

Performance Analysis of Integrated Terrestrial-Air-Underwater Optical Communication Network

This chapter demonstrated that FSO links in the back-end network of FSO-based architectures significantly enhance the performance and reliability of the network compared to conventional fiber-based architectures. As the future 6G network is anticipated to deliver a fully integrated TAU optical communication system, it is crucial to assess the end-to-end performance of an integrated TAU framework that takes into account impairments in both FSO and UWOC channels. This chapter analyzes the performance of a hybrid TAU optical architecture that combines FSO and UWOC technologies, supported by UAV-based relays.

The rest of this chapter is organized as follows: This chapter is introduced in Section 4.1. Section 4.2 discusses the motivation behind this work and highlights our key contributions. In Section 4.3, we explain the system model for the integrated FiWi-based UAV-assisted hybrid FSO and UWOC system. Section 4.4 presents the channel models used in the proposed system. In Section 4.5, we examine the channel statistics for the FSO and UWOC links. The problem formulation for optimizing the divergence angle and the proposed CODAT algorithm 4.1 is detailed in Section 4.6. Section 4.7 provides performance evaluations of the integrated system using both analytical and simulation results. Finally, Section 4.8 offers concluding remarks on the proposed work.

4.1 Introduction

6G wireless networks are anticipated to support high data rate and low latency demands for bandwidth-intensive applications like interactive video on demand, 8K video streaming, and 3D holographic communication. Additionally, with increasing underwater human activities, there is a growing need for reliable, high-throughput communication within underwater networks, particularly for submarines, autonomous underwater vehicle (AUV)s,

The work in this chapter resulted in the following publication:

1. P. Singh, V. A. Bohara and A. Srivastava, “On the Optimization of Integrated Terrestrial-Air-Underwater Architecture Using Optical Wireless Communication for Future 6G Network," in IEEE Photonics Journal, vol. 14, no. 6, pp. 1-12, Dec. 2022, Art no. 7355712, doi: 10.1109/JPHOT.2022.3210481.

and similar devices [94]. Traditionally, RF-based underwater communication is suited for short-range, low-data-rate applications due to its limited bandwidth and high absorption in oceanic environments. While acoustic communication can cover long distances underwater, it comes with higher latency and reduced data rates [95, 96]. In contrast, UWOC presents a promising solution, offering high data rates and secure data transmission with low power consumption in underwater scenarios [97]. Various models have been proposed to facilitate reliable communication between terrestrial and underwater networks. A hybrid FSO and UWOC based communication system has been proposed in [28]. The authors analyzed the performance of the proposed system in terms of outage probability, average BER, and average capacity. In [98], the authors analyzed the performance of a multi-user mixed FSO-UWOC system in terms of outage probability. However, the work is limited to FSO and UWOC based terrestrial-underwater cooperative network. Moreover, employing UAV as a terrestrial relay is foreseen as a viable solution to improve the performance of existing terrestrial-underwater communications systems [27]. UAV assisted relay can also assist in oceanography scenarios, where UAV can facilitate connection between the shore transmitter and an AUV. To improve the efficiency of the terrestrial-underwater cooperative network, UAV can be employed as an aerial relay to increase the communication range between the shore transmitter and AUV. In [27], the authors analyzed the performance of UAV assisted mixed RF and UWOC based communication systems in terms of outage probability, average BER, and average capacity. Furthermore, in [98] and [28], it is assumed that a static over sea surface (OSS) relay transmits the data between the terrestrial ground station and an AUV via FSO-UWOC link. In [27], the authors proposed UAV assisted RF-UWOC based system wherein RF link between UAV and OSS relay and an UWOC link between OSS relay and AUV is considered. Moreover, no communication link between UAV and the ground station is considered.

4.2 Motivation and Contribution

4.2.1 Motivation

With the increasing demand for underwater activities, there is a pressing need for high-throughput communication in underwater networks, particularly for AUVs. To address the requirement for high data rates, such as those needed for video surveillance, we propose a FiWi-based, UAV-assisted hybrid FSO and UWOC system within a terrestrial-underwater cooperative network. While previous research has largely focused on hybrid RF and UWOC links in air-underwater networks, the performance of UAV-assisted hybrid FSO and UWOC systems in terrestrial-underwater networks remains underexplored.

This work leverages optical wireless communication (OWC) technologies, including FSO and UWOC links in an integrated TAU optical network, to ensure high data rate transmission between terrestrial stations and AUVs. The joint evaluation of UAV-assisted FSO and UWOC communication in terrestrial and underwater environments has not yet been fully investigated. Most prior studies have examined mixed RF and UWOC link performance, along with optimal UAV positioning in air-underwater networks. As 6G networks evolve to integrate terrestrial, aerial, and underwater communications, we propose an end-to-end FiWi-based, UAV-assisted hybrid FSO and UWOC system using a decode-and-forward (DF) relaying protocol.

4.2.2 Contributions

The key contributions of this chapter are summarized as follows:

1. We examine the end-to-end performance of an integrated FiWi-based UAV-assisted hybrid FSO and UWOC system, focusing on outage probability. The analysis considers the impact of impairments in both the FSO and UWOC channels on overall outage performance. Furthermore, we derive an analytical expression for the outage probability of the proposed system based on the statistical characteristics of the FSO and UWOC channels.

2. We propose the CODAT algorithm 4.1 to optimize the optical beam's divergence angle, aiming to minimize the outage probability of the FSO link while ensuring that that the AUV's targeted data rate is met. The effect of the mobility of the OSS relay and the UAV on the performance of the proposed system has been thoroughly examined.

3. Additionally, as part of the performance evaluation, the end-to-end outage performance of the proposed system is compared with that of a traditional RF-based TAU communication system.

4.3 System Model

An integrated FiWi-based UAV-assisted hybrid FSO and UWOC network, as shown in Fig. 5.1. In this setup, a UAV-supported front-end network combining FSO and UWOC is linked to a XGPON for the back end. The back-end network includes a feeder fiber connecting the OLT at the central office (CO) to a passive splitter. This splitter then distributes the connection to ONUs via dedicated distribution fiber. The ONU is co-located with a shore transmitter that uses a LD to send information to the UAV via an FSO link. The UAV, acting as an aerial relay, forwards the information to the OSS relay through another FSO link. The OSS relay then transmits the data to an AUV using a UWOC link.

In this section, positions of terminals such as the ONU, UAV, OSS relay, and AUV are defined in 3D Cartesian coordinates (x, y, z). It is assumed that both the UAV and the OSS relay use the global positioning system (GPS) to transmit their location via beacon messages to the ONU and UAV, respectively [99]. Upon receiving the beacon message from the UAV, the ONU estimates the distance to the UAV, and the UAV estimates the distance to the OSS relay. The ONU and the UAV then select divergence angles to transmit optical beams to the UAV and OSS relay, respectively, according to the proposed CODAT algorithm 4.1. Both the OSS relay and AUV are considered to be mobile. The FSO links between the ONU and the UAV and between the UAV and OSS relay are subject to atmospheric turbulence, attenuation, and pointing errors. Additionally, the UWOC link between the OSS relay and AUV is assumed to experience Log-normal fading under weak oceanic turbulence, in line with the existing literature [98].

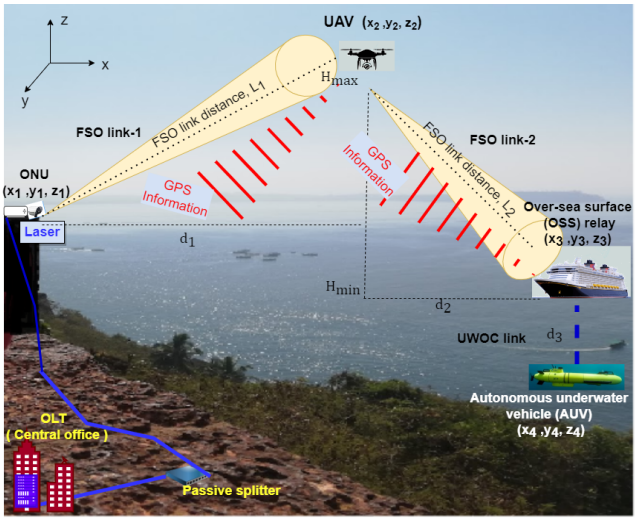

Figure 4.1: The proposed integrated FiWi based UAV assisted hybrid FSO and UWOC system.

4.4 Channel Modeling

This section presents the channel model for the UWOC link along with its associated impairment factors. The UWOC channel is modeled using a log-normal distribution to represent weak oceanic turbulence, incorporating distance-dependent path loss to reflect realistic underwater propagation conditions. The FSO channel model, previously detailed in Chapter 2, accounts for attenuation due to absorption and scattering, turbulence caused by random refractive index fluctuations, and pointing errors resulting from misalignment between transmitter and receiver apertures. The FSO link is treated as a fading channel influenced by atmospheric turbulence (h_{at}), pointing error (h_p), and atmospheric attenuation (h_a). Atmospheric turbulence is modeled as a random process following a Gamma-Gamma distribution, with its corresponding PDF provided in Chapter 2.

4.4.1 UWOC Channel Modeling

In this chapter, UWOC link between OSS relay and AUV is represented as the channel of fading under the impact of oceanic turbulence (h_o) and distance-dependent path loss (h_{PL}). Path loss (h_{PL}) in oceanic scenario can be estimated as in [98]

$$h_{PL} = \frac{A_{PD}\cos\theta_u}{2\pi L_{uwoc}^2\left(1-\cos\left(\theta_{d0}\right)\right)}\exp\left(-\frac{c\left(\lambda_{uwoc}\right)L_{uwoc}}{\cos\theta_u}\right), \tag{4.1}$$

where λ_{uwoc} is the wavelength of the optical beam in the underwater in meters, L_{uwoc} is the length of UWOC link between OSS relay and AUV in meters, and θ_{d0} is beam divergence angle of laser source. θ_u is the angle between the perpendicular to OSS relay plane and AUV-OSS relay trajectory.

Oceanic turbulence (h_o) follows log-normal distribution in weak oceanic turbulence as mentioned in [98]

$$f_{h_o}(h_u) = \frac{1}{2h_u\sqrt{2\pi}\sigma_u}\exp\left(-\frac{\left(\ln h_u - 2\mu_u\right)^2}{8\sigma_u^2}\right), \tag{4.2}$$

where h_u denotes the optical irradiance in the underwater. μ_u and σ_u^2 is the mean and variance of the random variable $\mathcal{X}$, respectively. Random variable $\mathcal{X}$ is expressed as $\mathcal{X} = \frac{1}{2}\ln h_o$. The scintillation index of oceanic

turbulence $\sigma_{h_o}^2$ is related to variance of Log-normal distribution is expressed as $\sigma_{h_o}^2 = \exp(4\sigma_u^2) - 1$. The PDF of the instantaneous SNR (γ_{uwoc}) of UWOC link is given as [98]

$$f_{\gamma_{\text{uwoc}}}(\gamma) = \frac{1}{4\gamma\sqrt{2\pi}\sigma_u} \exp\left(-\frac{\left(\ln\left(\frac{\gamma}{\bar{\gamma}_{\text{uwoc}}}\right) - 4\mu_u\right)^2}{32\sigma_u^2} \right). \tag{4.3}$$

On integrating (4.3), the corresponding CDF of the SNR of UWOC link is expressed as [98]

$$F_{\gamma_{\text{uwoc}}}(\gamma) = \frac{1}{2}\text{erfc}\left(\frac{\ln\left(\frac{\bar{\gamma}_{\text{uwoc}}}{\gamma}\right) + 4\mu_u}{4\sqrt{2}\sigma_u} \right). \tag{4.4}$$

4.4.2 End-to-End Data Rate Analysis

In this subsection, the end-to-end performance of the proposed system is evaluated in terms of the achievable data rate. The end-to-end data rate is constrained by the weakest link, as outlined in [100]. Consequently, the end-to-end data rate for the integrated FiWi-based UAV-assisted hybrid FSO and UWOC system using a DF relaying scheme is expressed as:

$$D_{e2e} = \min\{D_{\text{FSO}_1}, D_{\text{FSO}_2}, D_{\text{uwoc}}\}, \tag{4.5}$$

where D_{FSO_1} and D_{FSO_2} are the instantaneous achievable data rate of FSO links between ONU and UAV, and UAV and OSS relay, respectively. D_{uwoc} indicates the instantaneous achievable data rate of UWOC link between OSS relay and AUV. In the first FSO link between ONU and UAV, the achievable data rate is calculated as

$$D_{\text{FSO}_1} = \mathcal{B}_{FSO_1} \log_2(1 + \gamma_{FSO_1}), \tag{4.6}$$

where $\mathcal{B}_{FSO_1}$ denotes FSO bandwidth and γ_{FSO_1} is the SNR of FSO link between ONU and UAV. Similarly, we can obtain the data rate for FSO link between UAV and OSS relay as

$$D_{\text{FSO}_2} = \mathcal{B}_{FSO_2} \log_2(1 + \gamma_{FSO_2}), \tag{4.7}$$

where $\mathcal{B}_{FSO_2}$ denotes FSO bandwidth and γ_{FSO_2} is the SNR of FSO link between UAV and OSS relay. In the third link between OSS relay and AUV, the achievable data rate is given as

$$D_{\text{uwoc}} = \mathcal{B}_{\text{uwoc}} \log_2(1 + \gamma_{\text{uwoc}}), \tag{4.8}$$

where $\mathcal{B}_{\text{uwoc}}$ denotes bandwidth of UWOC link and γ_{UWOC} is the SNR of UWOC link between OSS relay and AUV.

4.4.3 End to End Outage Probability Analysis

In this section, the end-to-end outage probability of the proposed system is derived from the statistical characteristics, i.e., CDF of the end-to-end SNR.

4.4.3.1 Statistical Characteristics of the Channel Links

In this chapter, we consider the transmission of the optical beam over three independent downlink links. Given that the DF relaying scheme is employed, the analytical expression for the SNR of the end-to-end link in the proposed system is provided as [84].

$$\gamma_{e2e} = \min\left\{\gamma_{FSO_1},\ \gamma_{FSO_2},\ \gamma_{\text{uwoc}}\right\}, \tag{4.9}$$

where γ_{FSO_1}, γ_{FSO_2}, and γ_{uwoc} are the SNRs of FSO link between ONU and UAV, UAV and OSS relay, and UWOC link between OSS relay and AUV, respectively.

4.4.4 Cumulative Distribution Function

Finally, the CDF of SNR γ_{e2e} of the end-to-end UAV assisted FSO and UWOC based communication system is expressed as [101]

$$F_{\gamma_{e2e}}(\gamma) = 1-[\left(1 - F_{\gamma_{FSO_1}}(\gamma)\right) \times \left(1 - F_{\gamma_{FSO_2}}(\gamma)\right) \times (1 - F_{\gamma_{\text{uwoc}}}(\gamma))], \tag{4.10}$$

where $F_{\gamma_{FSO_1}}(\gamma)$ denotes the CDF of the SNR of FSO link between ONU and UAV, $F_{\gamma_{FSO_2}}(\gamma)$ denotes the CDF of FSO link between UAV and OSS relay. The analytical expression of CDF of the SNR of the end-to-end UAV-assisted FSO and UWOC system is calculated by substituting (2.8) and (4.4) in (4.10) and is shown in (4.11). In (4.11), ξ_1 and ξ_2 denote pointing error coefficient for FSO link between ONU and UAV and UAV and OSS relay, respectively.

$$\begin{aligned} F_{\gamma_{e2e}}(\gamma) = 1-\Bigg[&\left(1 - \frac{\xi_1^2}{\Gamma(\alpha_{f_1})\Gamma(\beta_{f_1})} G_{2,4}^{3,1}\left(\frac{\alpha_{f_1}\beta_{f_1}\wp_1}{\bar{\gamma}_{FSO_1}}\gamma \middle| \begin{matrix} 1, \xi_1^2+1 \\ \xi_1^2, \alpha_{f_1}, \beta_{f_1}, 0 \end{matrix}\right)\right) \\ &\times \left(1 - \frac{\xi_2^2}{\Gamma(\alpha_{f_2})\Gamma(\beta_{f_2})} G_{2,4}^{3,1}\left(\frac{\alpha_{f_2}\beta_{f_2}\wp_2}{\bar{\gamma}_{FSO_2}}\gamma \middle| \begin{matrix} 1, \xi_2^2+1 \\ \xi_2^2, \alpha_{f_2}, \beta_{f_2}, 0 \end{matrix}\right)\right) \\ &\times \left(1 - \frac{1}{2}\text{erfc}\left(\frac{\ln\left(\frac{\bar{\gamma}_{\text{UWOC}}}{\gamma}\right) + 4\mu_u}{4\sqrt{2}\sigma_u}\right)\right)\Bigg], \end{aligned} \tag{4.11}$$

4.4.5 Probability Density Function

To derive the PDF of the end-to-end SNR γ_{e2e} from the CDF given in (4.10), we begin by rewriting the CDF expression as:

$$\begin{aligned} F_{\gamma_{e2e}}(\gamma) &= 1 - \left(1 - F_{\gamma_{FSO_1}}(\gamma)\right)\left(1 - F_{\gamma_{FSO_2}}(\gamma)\right)\left(1 - F_{\gamma_{\text{uwoc}}}(\gamma)\right) \\ &= 1 - A(\gamma)B(\gamma)C(\gamma), \end{aligned} \tag{4.12}$$

where we define for brevity:

$$A(\gamma) = 1 - F_{\gamma_{FSO_1}}(\gamma),$$
$$B(\gamma) = 1 - F_{\gamma_{FSO_2}}(\gamma),$$
$$C(\gamma) = 1 - F_{\gamma_{\text{uwoc}}}(\gamma).$$

Differentiating both sides with respect to γ yields the PDF:

$$f_{\gamma_{e2e}}(\gamma) = \frac{d}{d\gamma} F_{\gamma_{e2e}}(\gamma) = -\frac{d}{d\gamma}\left[A(\gamma)B(\gamma)C(\gamma)\right]. \tag{4.13}$$

Applying the product rule for derivatives:

$$\frac{d}{d\gamma}[ABC] = A'BC + AB'C + ABC'. \tag{4.14}$$

We now use:

$$A'(\gamma) = -f_{\gamma_{FSO_1}}(\gamma),$$
$$B'(\gamma) = -f_{\gamma_{FSO_2}}(\gamma),$$
$$C'(\gamma) = -f_{\gamma_{\text{uwoc}}}(\gamma),$$

to obtain:

$$f_{\gamma_{e2e}}(\gamma) = f_{\gamma_{FSO_1}}(\gamma)B(\gamma)C(\gamma) + f_{\gamma_{FSO_2}}(\gamma)A(\gamma)C(\gamma) + f_{\gamma_{\text{uwoc}}}(\gamma)A(\gamma)B(\gamma). \tag{4.15}$$

Substituting back the expressions for $A(\gamma), B(\gamma), C(\gamma)$, we finally obtain:

$$\begin{aligned} f_{\gamma_{e2e}}(\gamma) =& [f_{\gamma_{FSO_1}}(\gamma)\left(1 - F_{\gamma_{FSO_2}}(\gamma)\right)\left(1 - F_{\gamma_{\text{uwoc}}}(\gamma)\right)] + [f_{\gamma_{FSO_2}}(\gamma)\left(1 - F_{\gamma_{FSO_1}}(\gamma)\right)\left(1 - F_{\gamma_{\text{uwoc}}}(\gamma)\right)] \\ &+ [f_{\gamma_{\text{uwoc}}}(\gamma)\left(1 - F_{\gamma_{FSO_1}}(\gamma)\right)\left(1 - F_{\gamma_{FSO_2}}(\gamma)\right)], \end{aligned} \tag{4.16}$$

where $f_{\gamma_{FSO_1}}(\gamma)$ denotes the PDF of the SNR of FSO link between the ONU and the UAV, $f_{\gamma_{FSO_2}}(\gamma)$ denotes the PDF of FSO link between the UAV and the OSS relay. The closed form expression of the PDF for the SNR of the end-to-end link of UAV-assisted FSO and UWOC communication system can be obtained by substituting (2.7), (2.8), (4.3), and (4.4) in (4.16).

4.4.6 Outage Probability

In this subsection, we analyze the outage probability of the integrated FiWi-based UAV-assisted hybrid FSO and UWOC system. Specifically, for a given data rate, the system experiences an outage when the instantaneous SNR of the end-to-end link falls below the SNR threshold γ_{th}. As no data is successfully received by the AUV when the received SNR is below γ_{th}, the outage probability P_{out} is expressed as:

$$P_{out} = Pr[\gamma_{e2e} < \gamma_{th}]. \tag{4.17}$$

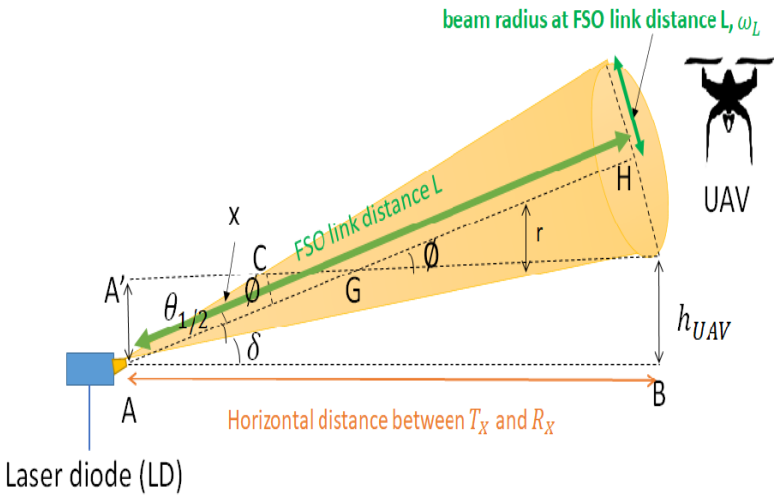

Figure 4.2: Geometry for Gaussian beam propagation model.

4.5 Optimal Divergence Angle Analysis

In this chapter, we assume that the optical beam of the FSO link incident on the detector's plane follows a Gaussian power intensity profile, as described in [46]. A Gaussian beam from a laser source is directed toward the detector's plane, which is perpendicular to the beam's propagation direction [46]. Here, L_F represents the FSO link distance between the laser source and the center of the beam footprint on the detector's plane. Fig. 4.2 illustrates the geometry of the Gaussian beam transmission from the laser source to the UAV, where the FSO link distance L_F along the optical beam axis is calculated as

$$L_F = x\cos(\theta_{d_{1/2}}) + AB\cos(\phi) - A'C\cos(\phi), \tag{4.18}$$

where $\phi = \delta + \theta_{d_{1/2}}$ is tilt angle and $\theta_{d_{1/2}}$ represents half of the divergence angle, is crucial in calculating the geometry of the system. x represents the distance between points A and C, while AB denotes the horizontal distance between the laser source and the detector. The vertical height of the UAV from the top of the tower, where the ONU is installed, is indicated by AA'. The variable r is calculated as $r = L_F\sin(\phi) - x\sin(\theta_{d_{1/2}})$. The elevation angle δ is estimated as

$$\delta = \arctan\left(\frac{AA'}{AB}\right), \tag{4.19}$$

The Gaussian beam radius of the optical beam ω_{L_F} is calculated as given in [46]

$$\omega_{L_F} = \omega_0\sqrt{1 + \left(1 + \frac{2\omega_0^2}{\vartheta^2(L_F)}\right)\left(\frac{\lambda L_F}{\pi\omega_0^2}\right)^2}, \tag{4.20}$$

where $\omega_0 = \frac{\lambda}{(\pi\theta_{d_{1/2}})}$ is the radius of the laser beam at the transmitter. The coherence length in meters is expressed as $\vartheta(L_F) = 0.55C_n^2\left(\frac{2\pi}{\lambda}\right)^2 L_F^{-3/5}$. Hence, the received optical power P_{rec} on the detector's plane from the beam footprint is calculated as given in [102].

$$P_{rec} = \frac{2\,P_T A_{PD}}{\pi\,(\omega_{L_F}^2)}\exp\left(-\frac{2r^2}{\omega_{L_F}^2}\right)10^{\left(\frac{-k_l L_F}{10}\right)}, \tag{4.21}$$

where P_T is transmitted optical power from the laser source.

4.5.1 Problem Formulation

The primary aim of this work is to optimize the divergence angle such that the outage probability of the FSO link is minimized while ensuring the targeted end-to-end data rate is met. The outage probability of the FSO link, caused by beam misalignment between the laser source and the detector, is calculated as follows [43].

$$P_{FSO}^{outage} = \exp\left(\frac{-(a+\omega_{L_F})^2}{2\sigma_{FSO}^2}\right), \tag{4.22}$$

where σ_{FSO}^2 is the variance of displacement of the optical beam and a is the radius of detector's area. Specifically, the optimization problem is formulated as the minimization of the outage probability of FSO link by optimizing the divergence angle of the optical beam as follows:

$$\begin{aligned}
\mathbf{P1} \quad & \min_{\theta_{d_1},\theta_{d_2},\delta_1,\delta_2} P_{FSO}^{outage} \\
s.t. \ & D_{e2e} \geq D_{req}, \\
& 0^o < \delta_1 \leq 90^o, \ 0^o < \delta_2 \leq 90^o, \\
& \theta_d^{\min} \leq \theta_{d_1} \leq \theta_d^{\max}, \ \theta_d^{\min} \leq \theta_{d_2} \leq \theta_d^{\max}, \\
& H^{\min} \leq H_{UAV} \leq H^{\max},
\end{aligned} \tag{4.23}$$

where D_{e2e} represents the achieved end-to-end data rate at the AUV, while D_{req} denotes the required data rate, set at 100 Mbps for digital video surveillance in oceanic environment monitoring systems [103]. The elevation angles at the ONU and UAV are given by δ_1 and δ_2, respectively, and θ_{d_1} and θ_{d_2} represent the beam divergence angles at the ONU and UAV, respectively. H^{min} and H^{max} define the minimum and maximum height of the UAV, while θ_d^{min} and θ_d^{max} are the minimum and maximum divergence angles of the optical beam at the laser source.

4.5.2 COgnition-based Divergence Angle Tracking Algorithm

To efficiently solve (**P1**), we propose the CODAT algorithm 4.1 to determine the optimal divergence angle of the optical beam, minimizing the outage probability of the FSO link while ensuring the targeted data rate for the AUV. The core idea behind the algorithm 4.1 is to leverage the knowledge of the thresholds for both end-to-end data rate and outage probability to optimize the beam's divergence angle.

By optimizing the divergence angle at the laser source, the performance of the proposed integrated FiWi-based UAV-assisted hybrid FSO and UWOC system can be further enhanced. Using algorithm 4.1, both the ONU and UAV can estimate the optimal divergence angle for transmitting the optical beam to the UAV and OSS relay, respectively. In this chapter, we assume that the divergence angles at the ONU and UAV can be adjusted through either mechanical or non-mechanical beam divergence adjustment techniques, as discussed in [104], [105]. These techniques offer a wide range of divergence angles, precise control, and rapid response times. According to algorithm 4.1, GPS beacon messages are used to estimate the locations of the UAV and OSS relay at the ONU and UAV, respectively. With this location data, the distance between the ONU and UAV can be determined, and δ_1 can be calculated using equation (4.19). The CODAT algorithm 4.1 then dynamically adjusts the values of θ_{d_1} and θ_{d_2} within the range of beam divergence angles, from θ_d^{min} to θ_d^{max}.

Algorithm 4.1 COgnition-based Divergence Angle Tracking (CODAT) Algorithm

Input: d_1, d_2.

1: Calculate δ_1 and δ_2
2: Initialize $\theta_{d_1}^k = \theta_{d_2}^k = [\theta_d^{min}, \theta_d^{max}]$
3: **for** k=0, 1, 2...,K **do**
4: Estimate L_{F_1} and L_{F_2}
5: Calculate $\omega_{L_{F_1}}$ and $\omega_{L_{F_2}}$ using (4.20)
6: Compute P_{FSO}^{outage} from (4.22)
7: **if** $P_{FSO}^{outage} \leq P_{th}$ **then**
calculate D_{e2e}
8: **else**
θ_d^k=θ_d^{k+1}, Go to step 4
9: **end if**
10: **if** $D_{e2e} \geq D_{req}$ **then**
$\theta_d^{optimal}$=θ_d^k
11: **else**
$\theta_d^k = \theta_d^{k+1}$, Go to step 4
12: **end if**
13: **end for**

Return: $\theta_1^{optimal}, \theta_2^{optimal}$

The FSO link distance between the ONU and UAV, denoted as L_{F_1}, is calculated using equation (4.18). For the FSO link distance between the UAV and OSS relay, L_{F_2}, and δ_2, we assume that AB represents the height of the UAV above the sea surface and AA' is the distance between the UAV and the OSS relay. Using equation (4.18), the beam radii at the UAV $\omega_{L_{F_1}}$ and OSS relay $\omega_{L_{F_2}}$ are determined. The maximum allowable outage probability for the UAV-assisted FSO link, P_{th}, is set to 10^{-3}. In each iteration, P_{FSO}^{outage} and D_{e2e} are computed using equations (4.22) and (4.5), respectively. The iteration continues until $P_{FSO}^{outage} \leq P_{th}$ and $D_{e2e} \geq D_{req}$. Finally, the optimal values of θ_{d_1} and θ_{d_2} are updated at the ONU and UAV using beam divergence adjustment techniques.

4.6 Results and Discussions

This section presents the end-to-end performance of the integrated FiWi-based UAV-assisted hybrid FSO and UWOC system, along with the performance of the proposed CODAT algorithm 4.1, evaluated through Monte Carlo simulations. For the end-to-end outage analysis, the SNR threshold is set at $\gamma_{th} = 2$ dB, as per [27]. The simulation parameters used in the analysis are listed in Table 4.1.

4.6.1 Outage Probability Analysis

Fig. 4.3 (a) presents the end-to-end outage probability as a function of the SNR for the complete link, accounting for the effects of atmospheric loss, pointing error, and atmospheric turbulence on both FSO links between the ONU and UAV, and the UAV and OSS relay. The analytical result derived in (4.11) is validated through simulations. The proposed system demonstrates significantly better outage performance in weak and moderate turbulence compared to strong turbulence, which degrades system performance. For instance, an outage probability of 10^{-1} is achieved at 15 dB SNR under moderate turbulence with pointing error ($\xi_1 = 1.01$,

Table 4.1: Simulation parameters considered in RF, FSO, UWOC, RF-based underwater channel

Parameters	Simulation values
FSO Channel	
λ	1550 nm
(x_1, y_1, z_1)	(0, 0, 100) m
(x_2, y_2, z_2)	(500, 0, 150) m
(x_3, y_3, z_3)	(1000, 0, 4) m
P_T	40 mW
$C_n^2(0)$ (moderate turbulence)	5×10^{-14} $m^{-2/3}$
$C_n^2(0)$ (strong turbulence)	1×10^{-13} $m^{-2/3}$
$C_n^2(0)$ (weak turbulence)	8×10^{-15} $m^{-2/3}$
(θ_d^{min})	0.05 mrad
(θ_d^{max})	1.5 mrad
a	5 cm
$\mathfrak{R}$	0.5 A/W
σ_j	30 cm
A_{PD}	7 mm^2
ΨFoV	5.15^o
$G(\varphi)$	1
k_l	0.43
$\sigma_{n_{01}}^2$	10^{-14}
$\mathcal{B}_{FSO}$	625 MHz
UWOC Channel	
λ_{uwoc}	532 nm
d_3	1-10 m
(x_4, y_4, z_4)	(1000, 0, d_3) m
θ_{d0}	10^o
θ_u	5^o
$C(\lambda_{uwoc})$ for clear ocean water	0.151
P_T	0.1 W
A_{PD_u}	1.7×10^{-4} per m^2
$\mathfrak{R}$	1 A/W
$\mathcal{B}_{uwoc}$	150 MHz
$\mathcal{N}_{uwoc}$	1.6×10^{-14} W/Hz
RF Channel	
P_T	0.1 W
$\mathcal{B}_{RF}$	625 MHz
Pathloss coefficients (A, B)	(-1.5, 3.5)
K(0)	5 dB
$\mathcal{N}_{RF}$	2.57×10^{-12} W/Hz
K(π/2)	15 dB
RF based underwater Channel	
$f_{c_{uwoc}}$	420 MHz
σ_{uwoc}	0.075 m^{-1}
μ_{uwoc}	1.2566×10^{-6} Hm^{-1}
ϵ_{uwoc}	6.8588×10^{-10} Fm^{-1}
P_T	0.1 W
$\mathcal{B}_{RF_{uwoc}}$	100 MHz
$\mathcal{N}_{RF_{uwoc}}$	4.0×10^{-13} W/Hz

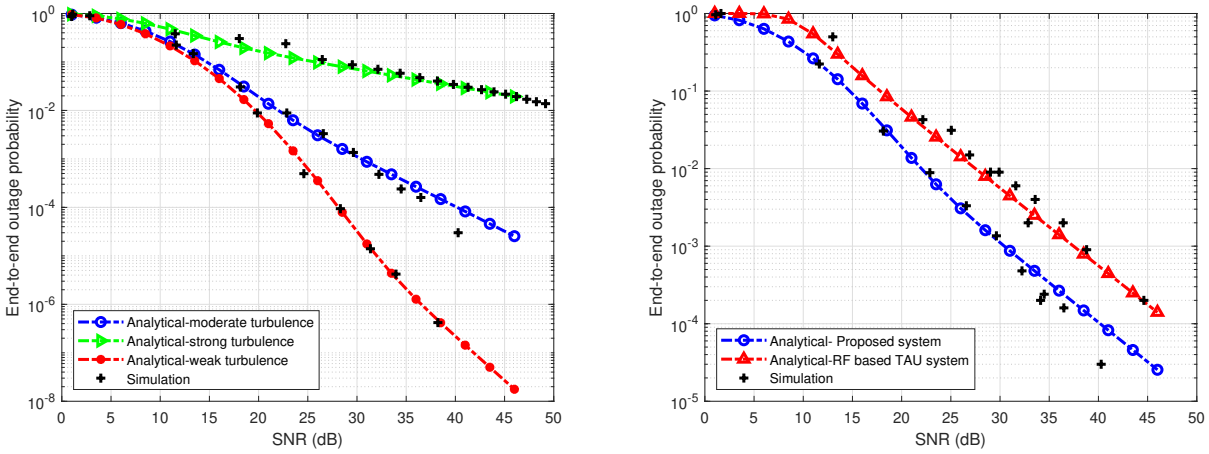

(a) (b)

Figure 4.3: (a) End-to-end outage probability of an integrated FiWi based UAV assisted hybrid FSO and UWOC framework over weak, moderate and strong turbulence with pointing errors. (b) Comparison of end-to-end outage probability of an integrated FiWi based UAV assisted hybrid FSO and UWOC system with conventional RF based TAU communication framework.

$\xi_2 = 0.7$), and at 13.5 dB SNR under weak turbulence with pointing error ($\xi_1 = 1.45$, $\xi_2 = 1.03$). In contrast, for strong turbulence with pointing error ($\xi_1 = 0.6$, $\xi_2 = 0.47$), an outage probability of 10^{-1} requires 25 dB SNR. Moreover, in moderate turbulence, an outage probability of 10^{-3} is achieved at 30 dB SNR.

For comparison, a conventional RF-based TAU communication framework is considered, where the channels between the ONU and UAV, and the UAV and OSS relay, are RF links. Additionally, the OSS relay is connected to the AUV through an RF-based underwater link. The RF channels between the ONU and UAV, and the UAV and OSS relay, are assumed to experience Rician fading due to a strong LoS path, following the model in [106]. The RF-based underwater link between the OSS relay and AUV is modeled according to [107]. Fig. 4.3 (b) compares the end-to-end outage performance of the integrated FiWi-based UAV-assisted hybrid FSO and UWOC system with that of the conventional RF-based TAU communication framework. The proposed system outperforms the RF-based framework, particularly under moderate turbulence with pointing error. An outage probability of 10^{-3} is achieved at 30 dB SNR for the proposed system, while the conventional RF-based framework requires 37 dB SNR to achieve the same outage probability.

4.6.2 Performance Evaluation of CODAT Algorithm 4.1

To assess CODAT's performance under moderate turbulence with pointing errors ($\xi_1 = 1.01$, $\xi_2 = 1.01$), we use a beam displacement standard deviation of $\sigma_{FSO} = 0.015$. Furthermore, the distance between the UAV and the OSS relay is assumed to fluctuate dynamically due to the OSS relay's movement. Fig. 4.4 (a) illustrates the variation in FSO outage probability (P_{FSO}^{outage}) as a function of d_2, with $d_1 = 455$ m and $\theta_{d_1} = 0.05$ mrad. From Fig. 4.4 (a), it is clear that P_{FSO}^{outage} decreases as the beam divergence angle (θ_{d_2}) increases. However, for shorter distances between the UAV and the OSS relay, an outage probability of less than 10^{-3} can be achieved. By reducing θ_{d_2}, longer distances between the UAV and the OSS relay become possible. For example, at $\theta_{d_2} = 0.05$

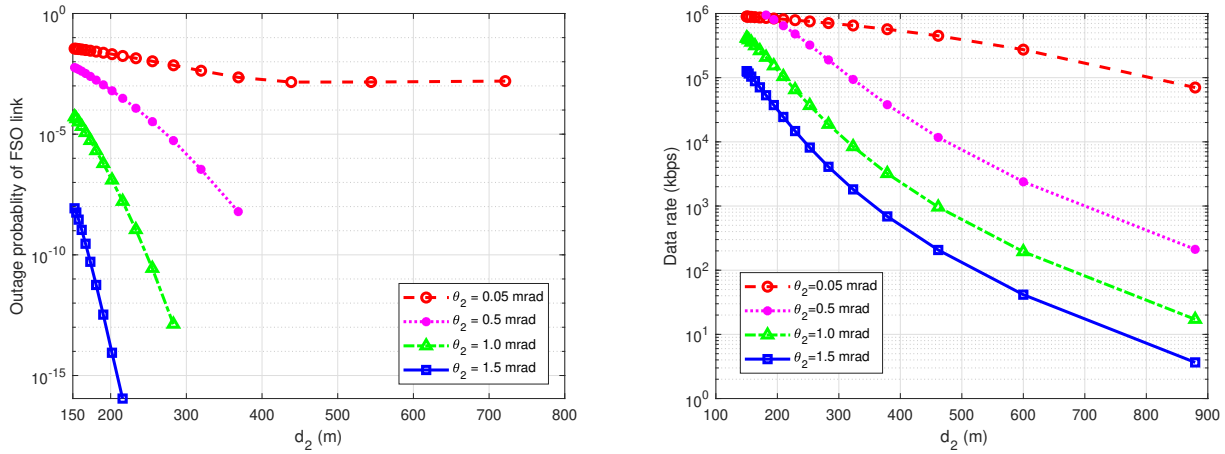

Figure 4.4: (a) End-to-end outage probability of FSO link versus FSO link distance between UAV and OSS relay, d_2 for different divergence angles. (b) Data rate between OLT and OSS relay versus FSO distance between UAV and OSS relay, d_2.

mrad and $d_2 = 720$ m, an outage probability of 10^{-3} is reached. In contrast, for $\theta_{d_2} = 1.5$ mrad, $P_{FSO}^{outage} \leq 10^{-3}$ is only achieved for much shorter distances, around $d_2 = 220$ m. Thus, a trade-off exists between transmission distance and FSO outage probability.

Fig. 4.4 (b) illustrates the end-to-end data rate for different values of θ_{d_2}, with $d_1 = 455$ m and $\theta_{d_1} = 0.05$ mrad. It is evident that the target data rate of 100 Mbps can be achieved at the OSS relay when $\theta_{d_2} = 0.05$ mrad is used, as a smaller beam divergence angle results in reduced pointing errors. Conversely, larger values of θ_{d_2} increase pointing errors, preventing the system from reaching the 100 Mbps target at higher divergence angles. Additionally, smaller values of θ_{d_2} allow for an extended distance between the OSS relay and the UAV. For instance, at $\theta_{d_2} = 0.05$ mrad, the 100 Mbps data rate requirement is met at the OSS relay with $d_2 = 800$ m.

As shown in Fig. 4.5 (a), the end-to-end data rate decreases as the underwater distance between the OSS relay and AUV (d_3) increases from 1 m to 10 m. When $d_3 = 5$ m and $\theta_{d_2} = 0.05$ mrad, the system achieves an end-to-end data rate exceeding 200 Mbps at $d_2 = 415$ m. Furthermore, a higher data rate can be achieved at shorter distances between the UAV and OSS relay. However, when d_2 exceeds 600 m, the desired data rate at the AUV is not reached.

For comparison, the performance of the proposed system is benchmarked against a conventional RF-based TAU communication framework. The results indicate that the conventional RF-based framework performs poorly, particularly in terms of end-to-end data rate, and fails to meet the required data rate. In contrast, the integrated FiWi-based UAV-assisted hybrid FSO and UWOC system significantly outperforms the RF-based framework, particularly for small beam divergence angles. At a fixed $d_3 = 5$ m, the integrated FiWi-based system achieves superior performance, providing data rates up to 100 Mbps. At $d_2 = 415$ m with $\theta_d = 0.05$ mrad, more than 100 Mbps is achieved at the AUV. For $\theta_{d_2} = 0.1$ mrad, a 100 Mbps data rate is achieved at a shorter distance of $d_2 = 205$ m. In comparison, the conventional RF-based system delivers less than 40 Mbps

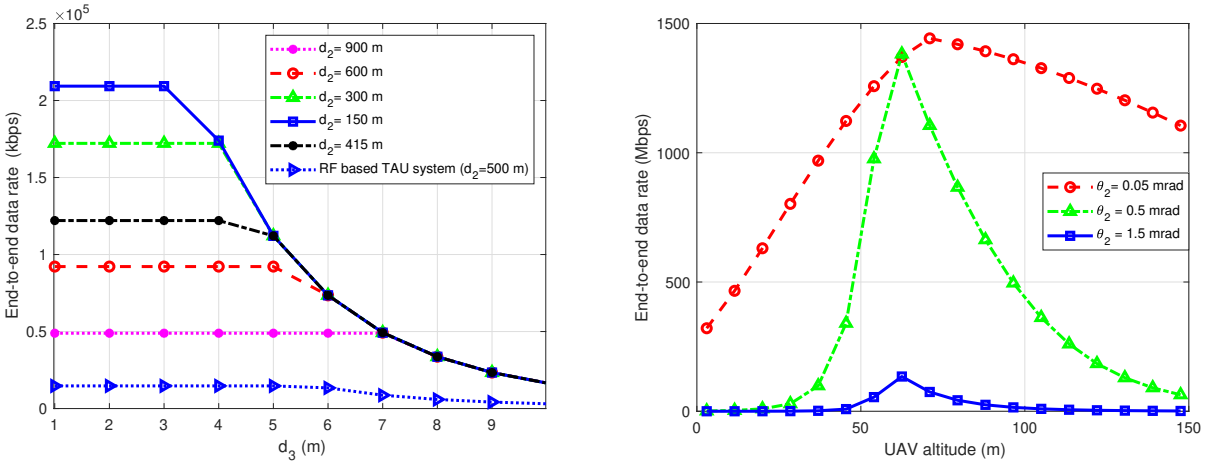

Figure 4.5: (a) End-to-end data rate of an integrated FiWi based UAV assisted hybrid FSO and UWOC system versus underwater link distance between OSS relay and AUV, d_3 with $\theta_{d_2} = 0.05$ mrad. (b) Data rate of FSO link between OLT and OSS relay versus UAV altitude.

at $d_2 = 500$ m and $d_3 = 6$ m. Thus, there is a clear trade-off between the end-to-end data rate and the distance between the UAV and OSS relay (d_2) in both systems.

To examine the effect of UAV altitude on the data rate at the OSS relay, Fig. 4.5 (b) shows the data rate versus UAV altitude when $d_1 = 455$ m and $d_2 = 550$ m. At a beam divergence angle of $\theta_{d_2} = 0.05$ mrad, the data rate at the OSS relay reaches its peak when the UAV is at an altitude of 70 m. This is due to the strong LoS between the ONU and UAV, and the relatively short distance between the UAV and OSS relay. However, at higher UAV altitudes, the data rate performance at the OSS relay deteriorates as the distance between the ONU and UAV, as well as between the UAV and OSS relay, increases. For larger divergence angles, the data rate decreases more significantly with increased UAV altitude. Fig. 4.6 (a) shows the end-to-end data rate performance of the proposed system as a function of UAV altitude with $\theta_{d_1} = \theta_{d_2} = 0.05$ mrad. For $d_3 = 1$ m, an end-to-end data rate of 450 Mbps can be achieved when the UAV operates at an altitude between 56 m and 95 m. In the case of $d_3 = 5$ m, an end-to-end data rate exceeding 100 Mbps is achieved when the UAV altitude increases from 45 m to 130 m.

Fig. 4.6 (b) compares the end-to-end data rate versus d_2 for both the UAV-assisted FSO and UWOC system and the conventional RF-based communication framework, with $d_3 = 5$ m. It is observed that the proposed system can achieve more than 100 Mbps up to $d_2 = 415$ m with a beam divergence angle of $\theta_{d_2} = 0.05$ mrad. With a larger angle of $\theta_{d_2} = 0.1$ mrad, the same data rate is reached at a shorter distance of $d_2 = 200$ m. In contrast, the conventional RF-based TAU communication system consistently delivers less than 20 Mbps.

4.7 Chapter Summary

In this chapter, we analyzed the end-to-end performance of a UAV-assisted hybrid FSO and UWOC system integrated with a FiWi network, focusing on the outage probability under the influence of FSO and UWOC channel impairments. We derived and validated the analytical expression for the system's outage probability

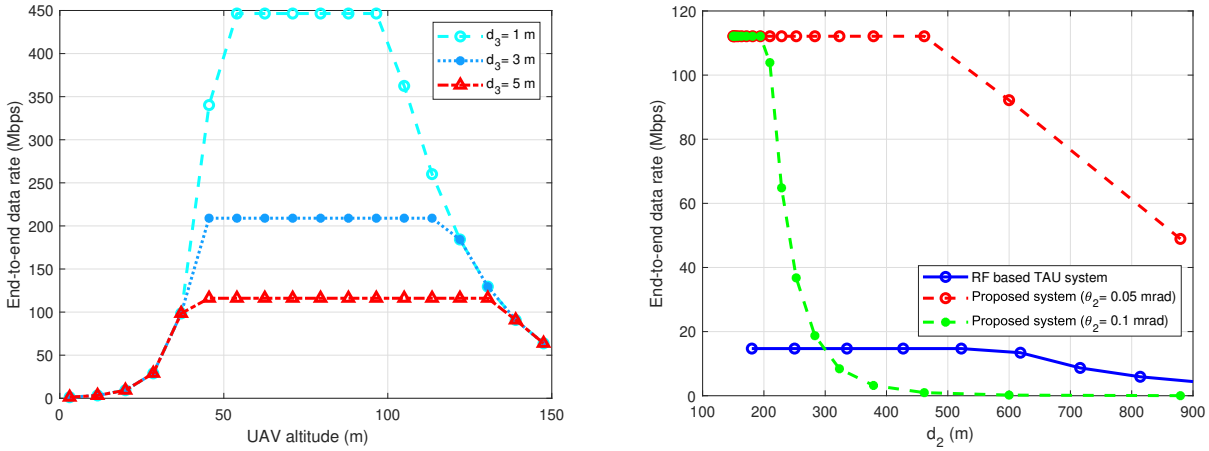

Figure 4.6: (a) End-to-end data rate of an integrated FiWi based UAV assisted hybrid FSO and UWOC system versus UAV altitude with $\theta_{d_2} = 0.05$ mrad. (b) Comparison of end-to-end data rate of an integrated FiWi based UAV-assisted FSO and UWOC system against conventional RF based TAU communication framework.

through simulations. Furthermore, we formulated an optimization problem to minimize the outage probability of the FSO link between the ONU and OSS relay by optimizing the divergence angle of the optical beam, ensuring the AUV's target data rate. The problem was solved using a novel CODAT algorithm 4.1. Our analysis demonstrated that using a small beam divergence angle mitigates beam misalignment caused by UAV movement. However, the end-to-end data rate is limited by the transmission distance between the UAV and OSS relay, as there is a trade-off between distance and achievable data rate. Simulation results identified the optimal transmission ranges between the UAV, OSS relay, and AUV for improved end-to-end performance.

Chapter 5

Optimal Resource Allocation in FSO-based Communication Networks

In previous chapters, the application of FSO communication technology in hybrid OWC-based architectures has been shown to significantly boost overall performance. However, when obstacles are present, achieving a reliable LoS between communicating devices becomes challenging, critically impacting the efficacy of the FSO link. Recently, OIRS and UAVs have emerged as innovative solutions to address challenges posed by non-LoS links in FSO communication networks. The integration of OIRS-assisted UAVs into FSO-based networks offers a viable approach to overcoming non-LoS link issues. Furthermore, optimizing resource allocation in OIRS-assisted UAV-based FSO networks has the potential to significantly enhance overall network performance. Part I of this chapter explores an optimal mirror-element assignment scheme, known as signal strength aware multiple mirror element assignment (SMA), which performs simultaneous mirror-element allocation for multiple users. Additionally, a performance comparison between the SMA scheme and other methods, such as equal mirror element assignment (EMA), exhaustive search, non-orthogonal multiple access (NOMA), and TDMA, is presented. The results highlight the superiority of the SMA scheme over existing reference schemes.

Part II of this chapter analyzed the integration of laser-based OWC technology with an OIRS-assisted UAV to support the QoS requirements of 6G-based indoor wireless networks. Specifically, in this part, a joint user selection and mirror element assignment problem is developed to maximize the number of users served subject to QoS and OWC-related design constraints. To realize optimization in a distributed manner, a batch-based user-selection and mirror-element assignment (batch-based user-selection and mirror-element assignment (BMEA)) scheme is proposed and analyzed that performs simultaneous mirror-element assignment decisions for several contending users in part II.

The work in this chapter resulted in the following publication:

1. P. Singh, V. A. Bohara and A. Srivastava, "On the Optimal Assignment of Mirror Element in UAV and OIRS-Assisted OWC based Architecture," 2023 IEEE 97th Vehicular Technology Conference (VTC2023-Spring), Florence, Italy, 2023, pp. 1-7, doi: 10.1109/VTC2023-Spring57618.2023.10199990.

2. P. Singh, H. B. Salameh, V. A. Bohara, A. Srivastava and M. Ayyash, "Optimizing Connectivity in OIRS-Assisted UAV Indoor Optical Networks: Efficient Admission Control and Mirror-Element Assignment," in IEEE Transactions on Network Science and Engineering, vol. 11, no. 3, pp. 2890-2900, May-June 2024, doi: 10.1109/TNSE.2024.3353671.

5.1 Challenges and Opportunities in FSO Networks: The Role of OIRS-Assisted UAVs

The important challenge of FSO is to provide LoS between the communicating devices. The network's overall performance degrades if physical blockages obstruct the FSO link. Recently, IRS has emerged as a potential solution to alleviate the effects of non-LoS or blockages [55], [56], [13]. Recently, IRS has been utilized for significant performance improvement in cellular networks in the event of non-availability of LoS and skip-zone problems. OIRS can reflect or beamform the signal in the user's desired direction. Integrating UAVs and OIRS as OIRS-assisted UAVs could be a viable solution to mitigate the effect of non-LoS as well as blockages. Furthermore, the LoS requirement can be alleviated by installing an OIRS-assisted UAV as a mobile relay between the optical transmitter and the optical receiver [53]. The OIRS-assisted UAVs are intended to enhance the performance of FSO-based networks.

Several works on UAV-assisted FSO-based networks have been reported in the literature [42, 46]. UAV-assisted aerial relays could be deployed in difficult terrains to offer users the required QoS. The overall performance of a UAV-assisted FSO-based network is evaluated by taking into account the combined effects of AoA fluctuation, pointing errors, atmospheric attenuation, and atmospheric turbulence in [42]. Subsequently, the performance of OIRS for OWC-based systems has been analyzed in [17, 18, 53, 57, 108]. In [17], the authors compared the performance of phased array and mirror-based OIRS performance in FSO-based networks. Specifically, the authors evaluated power assignment and beam-splitting algorithms for PA and mirror-based OIRS. In [53, 57], the authors evaluated the performance of an IRS-assisted UAV-based hybrid RF/FSO-based network under the effects of effect of the channel impairments. In [108], the authors quantified the pointing errors and analytically analyzed the FSO-based channel under the combined effect of the IRS element's size, orientation, and position.

Therefore, from the above, it is evident that both OIRS-assisted UAV and laser-based communication can significantly enhance the performance of conventional OWC-based wireless networks. However, such system integration possesses several design challenges regarding optimal user selection and OIRS-assisted UAV mirror element assignment so that system performance is enhanced.

5.1.1 Motivation

Most prior works have focused on the performance of OIRS-assisted UAV-based FSO networks. However, the optimization framework for mirror element allocation to serve multiple users in OIRS-assisted UAV-based FSO networks has not yet been introduced. In recent works, it is assumed that all the resource elements of OIRS, i.e., mirror elements, are assigned to a desired user. Moreover, prior works do not consider assignments of mirror elements. In this chapter, we investigate the performance of the OIRS-assisted UAV-based FSO network under the impact of the four channel impairments: atmospheric path loss, atmospheric turbulence, misalignment error due to hovering of OIRS-assisted UAV, and AoA fluctuations. In particular, the mirror assignment problem under QoS design constraints is investigated. Further, we propose a SMA scheme, where multiple mirror elements are intelligently assigned to the desired users. We compare the performance of the SMA scheme with

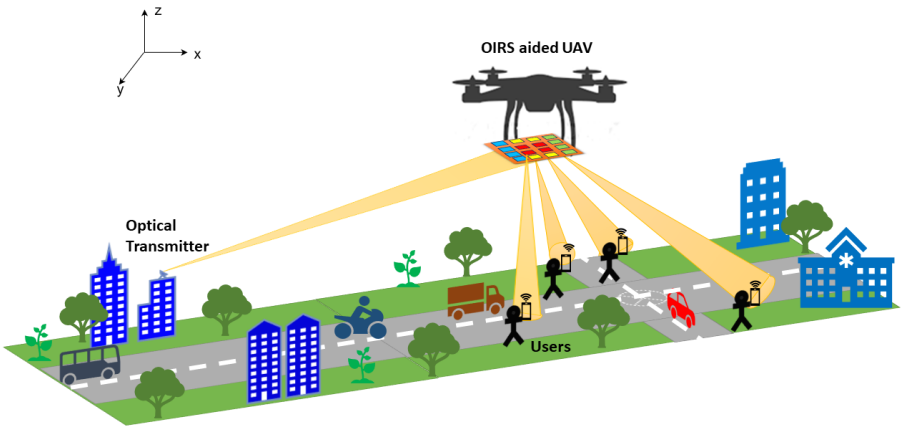

Figure 5.1: System model

respect to the EMA scheme and the most commonly used multiple access benchmark schemes, such as NOMA and TDMA. The results demonstrate our proposed scheme's potential gains over TDMA, NOMA, and EMA schemes.

5.1.2 Contributions

The major contributions of part I of this chapter are outlined as follows.

1. We investigate the performance of OIRS-assisted UAV-based FSO networks by employing our mirror element assignment scheme, i.e., SMA, in terms of average user rate, sum rate, outage probability, and fairness.

2. The performance of the proposed SMA scheme is compared with the EMA scheme, where an equal number of mirrors are assigned to the users for simultaneous transmission.

3. The performance of the SMA scheme is also compared with the conventional multiple access schemes such as TDMA, NOMA, and exhaustive search. The SMA outperforms other schemes, and its performance does not show significant degradation with changes in network parameters.

5.2 System Model and Channel Modeling

5.2.1 System Model

We assume OIRS-assisted UAV-based FSO networks, where an OIRS-assisted UAV provides coverage and resolves the Non-LoS problem so that fairness in terms of rate is guaranteed to the users, as shown in Fig. 5.1. Further, we consider OIRS-assisted UAV-based FSO networks with set of $\mathcal{U}$ users, where $U = |\mathcal{U}|$ denotes the number of users. In the outdoor space, U contending users are distributed in 3D coordinates (x, y, z). Let $\mathcal{M}$ be defined as the set of M mirror elements, where $M = |\mathcal{M}|$ represents the number of mirror elements. Without loss of generality, we also assume that $M > U$. Further, we consider that the optical transmitter in

the network is equipped with a laser source for transmitting information to the OIRS-assisted UAV via an FSO link. The mirror-based OIRS is installed on UAV so that the optical beam is beamformed and reflected in the direction of the desired user as in [17, 53]. The divergence angle of the transmitted optical beam from the laser source is chosen and focused in such a way that the Gaussian beam's footprint covers the entire surface of the OIRS. In addition, we assume the optical transmitter transmits information to U mobile users through optical signals. A PD is used at the user's receiver to convert the received signal from an optical signal to an electrical signal. The position of the OIRS-assisted UAV, optical transmitter, each mirror element, and users are expressed in terms of 3D coordinates (x, y, z). Furthermore, we assume that the OIRS-assisted UAV utilizes an outdoor localization system to transmit its location to the transmitter through beacon messages [99, 109]. As per the location information of the UAV, the optical beam is directed toward the OIRS-assisted UAV. Moreover, in this chapter, we assume that the movement and orientation of each mirror element are regulated by a CC of an OIRS-assisted UAV. Further, we assume that the FSO-based communication link between the optical transmitter and OIRS-assisted UAV, and OIRS-assisted UAV and each user experiences atmospheric turbulence with attenuation, misalignment error due to hovering OIRS-assisted UAV, and AoA fluctuations [46]. Furthermore, in this chapter, we assume that the orientation angle of each mirror element θ_i is rearranged such that the optical beam is beamformed in a particular direction, and θ_i is already defined in Chapter 2. Additionally, we assume that the beam incident on the OIRS surface follows a Gaussian power profile, as described in [17, 46]. The geometry of the beam path from the optical transmitter to the OIRS-assisted UAV is illustrated in Fig. 5.2.

5.2.2 Channel Model

We assume that the optical transmitter is transmitting data to OIRS-assisted UAV via an FSO link, and further transmitted data is reflected from OIRS-assisted UAV to users via the FSO link. The FSO link is affected by FSO channel impairments such as atmospheric attenuation (h_a), atmospheric turbulence (h_{at}), and pointing error (h_{pe}), beam misalignment error due to hovering OIRS-assisted UAV (h_{be}), and FSO link disruption by virtue of AoA fluctuations (h_{AoA}). The FSO communication link is impacted by atmospheric turbulence (h_{at}), atmospheric attenuation (h_a), and the pointing error (h_{pe}), and their PDF is expressed as in Chapter 2. The beam misalignment due to hovering of OIRS-assisted UAV (h_{be}) is modeled as zero-mean Gaussian random variable, and its PDF is given as in [108, 110]

$$f_{h_{be}}(h_{be}) = \frac{\sqrt{\varpi}}{2\sqrt{\pi}A_0}\left[\ln\left(\frac{A_0}{h_{be}}\right)\right]^{-1/2}\left(\frac{h_{be}}{A_0}\right)^{\varpi-1}, (0 \le h_{be} \le A_0), \tag{5.1}$$

where $A_0 = [\mathrm{erf}(v)]^2$ and $v = \frac{\sqrt{2}a\cos\theta_{ul}}{\omega_{L_{F_2}}}$. θ_{ul} represents the angle between the reflected beam and the normal vector at the user. Further, we have

$$\varpi = \frac{\sqrt{\pi}}{8}\frac{\mathrm{erf}(v)}{v\exp(-v^2)\cos^2(\theta_{ul})\sigma_u^2}, \tag{5.2}$$

$$\sigma_u^2 = \frac{1}{\cos^2(\theta_{ul})}\left(\frac{\sin^2(\theta_i+\theta_r)}{\cos^2(\theta_i)}\right)\sigma_{OIRS}^2 \tag{5.3}$$

where σ_{OIRS}^2 denotes the variance of OIRS-assisted UAV fluctuations. θ_i and θ_r represent the incident and reflected angles of the beam at the OIRS plane. As a result of the hovering of OIRS-assisted UAV, AoA

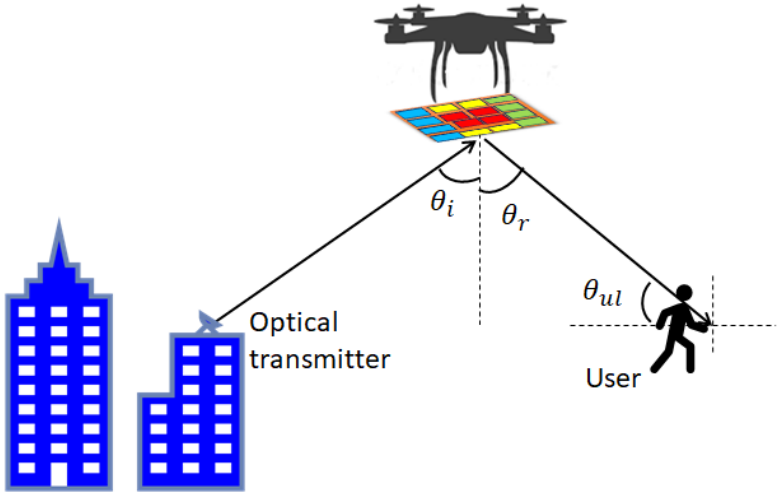

Figure 5.2: Schematic illustration of the FSO link between optical transmitter-to-OIRS-assisted UAV-to-user

fluctuations also occurred, which degrades the received signal strength at the user's receivers. Nevertheless, with the help of the lens, the received optical beam is focused toward the photodiode's plane, and AoA still deviates from the normal because of random orientation fluctuations of the OIRS-assisted UAV. The AoA fluctuations can be modeled as in [111] and expressed as $h_{AoA} = \Pi\left(\theta_{AoA}/\Psi_{FoV}\right)$, where $\Pi(\varkappa) = 1$ if $|\varkappa| \leq 1$, and $\Pi(\varkappa) = 0$ otherwise. Ψ_{FoV} represents the FoV of the receiver. θ_{AoA} represents incidence angle of the optical beam, and its PDF is expressed in [111, 112]. The PDF of AoA fluctuations can be written as in [111]

$$f_{h_{AoA}}(h_{AoA}) = \exp\left(\frac{-\theta_{FoV}^2}{2\sigma_{AoA}^2}\right)\delta(h_{AoA}) + \left(1 - \exp\left(\frac{-\theta_{FoV}^2}{2\sigma_{AoA}^2}\right)\right)\delta(h_{AoA} - 1), \tag{5.4}$$

where $\delta(.)$ is Dirac delta function.

5.3 Rate, Fairness, and Rate Outage Probability Analysis

In this subsection, the performance of the proposed networks is investigated in terms of performance metrics such as rate, fairness, and rate outage probability. When the set of selected mirror elements ($\Omega_j \subseteq \mathcal{M}$) are targeted at a jth user, received power density distribution $\mathcal{P}_j(x, y)$, can be given as

$$\mathcal{P}_j(x,y) = \frac{\mathcal{K}A_c^2}{\omega_{L_F}^2} \sum_{i\in\Omega_j} exp\left[-\frac{2((x + x_i - x_j)^2 + (y + y_i - y_j)^2)}{\omega_{L_F}^2}\right] cos\theta_i. \tag{5.5}$$

Thus, the SNR of a user is computed as

$$\gamma_j = \frac{\left[\mathfrak{R}_j \mathcal{P}_j(x,y) A_{PD_j} h_{F_2}\right]^2}{n_1 \mathcal{B}}, \tag{5.6}$$

where $\mathfrak{R}_j$ represents the responsivity of the jth PD, A_{PD_j} denotes effective area of the jth PD [113], $\mathcal{B}$ is bandwidth, and n_1 is the AWGN with zero mean and variance σ_n^2. Hence, the achievable transmission rate (in bits/s/Hz) of jth user is calculated as

$$R_j = \log_2(1 + \gamma_j). \tag{5.7}$$

In order to perform the fairness evaluation, we assume Jain's fairness index, which is expressed as [88], $F_j = \frac{\left(\sum_{j=1}^{N} R_j\right)^2}{N \sum_{j=1}^{N} R_j^2}$. When fairness index reaches approximately unity, all the users in the proposed network acquire a uniform transmission rate. We assume that the communication link between the communicating devices is in outage if the R_j falls below the required demand rate R_D. Hence, the rate outage probability ϕ_{CO} is expressed as

$$\phi_{CO} = \Pr\left(R_j < R_D\right). \tag{5.8}$$

5.3.1 Performance Comparison

Different multiple-channel access schemes, such as power-domain NOMA and TDMA, have been proposed in the prior literature. For benchmark comparison, the performance of the SMA scheme is evaluated with respect to power-domain NOMA and TDMA. The simplest of these schemes is the TDMA, wherein in the context of OIRS-assisted transmission, all M transmit the same data to serve a single targeted user at one instant of time. In the case of TDMA, (5.7) is modified as $R_j = \alpha_j \log_2(1 + \gamma_j)$, where the proportion of the transmission time that OIRS spends on jth user is denoted by α_j, which is constrained to $\sum_{j \epsilon U} \alpha_j \leq 1$. Hence, in OIRS-assisted TDMA, all U are served in equal time slots. While in NOMA scheme, the data of each user is multiplexed in the power domain by utilizing the superposition coding at the transmitter, and different transmit power levels are assigned to different users [114]. In NOMA, the users having low SNR are assigned with higher powers as follows $P_{j_1} \geq P_{j_2} \geq ..... \geq P_{j_{U-1}} \geq P_U$. The transmit powers assigned to successive users ($j > 1$) are expressed as

$$P_j = a_j P_{j-1}, \tag{5.9}$$

where $0 < a_j \leq 1$ is the allocated power coefficient to the jth user. Because of the total transmit power constraint, the below-given power constraint should be satisfied

$$\sum_{j=1}^{U} P_j = P_T, \tag{5.10}$$

where P_T is the total power transmitted by the optical transmitter.

5.4 Problem Formulation

5.4.1 Problem Statement

Our problem statement for the proposed system model is defined as follows: For the given set of users $\mathcal{U}$, set of mirror elements $\mathcal{M}$, required fairness index F^*, and orientation angle $\theta_j^{(i)}$, our main objective is to find appropriate mirror-elements i^* (conduct mirror-element assignment) that achieves design objective of maximizing the rate of the downlink transmissions subject to given below design constraints:

C1) **Fairness constraint**: This fairness constraint guarantees that the fairness index should be higher than F^*.

C2) **Mirror element constraint**: This constraint assures that each mirror element is only assigned to a single

user.

C3) **Power constraint**: This constraint ensures that users with poor channel conditions are assigned suitable mirror elements that can reflect higher optical power.

C4) **Orientation angle constraint**: This constraint guarantees that the orientation angle of every mirror element should lie within the given defined range.

C5) **Divergence angle constraint**: This constraint ensures the optical transmitter's divergence angle θ_d is selected such that the beam's footprint covers the entire surface of OIRS.

5.4.2 Problem Formulation

In our optimization framework, we defined $\chi_j^{(i)}$ as the binary decision variable, which is expressed as:

$$\chi_j^{(i)} = \begin{cases} 1, & \text{if mirror element } i \text{ is assigned to contending user } j \\ 0, & \text{otherwise.} \end{cases} \tag{5.11}$$

To maintain uniform fairness in terms of rate among users, analytically, our mirror element assignment problem can be formulated as follows:

$$\begin{aligned} \mathbf{P1}: & \max_{\chi_j^{(i)}} R_j \\ s.t.\ & F_j \geq F^*,\ \forall j \in \mathcal{U} \\ & \sum_{j \in \mathcal{U}} \chi_j^{(i)} \leq 1,\ \forall i \in \mathcal{M} \\ & P_{n_s}^{(i)} \ll P_{n_w}^{(i)},\ \forall i \in \mathcal{M} \\ & -\pi/2 < \theta_j^{(i)} < +\pi/2,\ \forall i \in \mathcal{M} \\ & \theta^{\min} \leq \theta_d \leq \theta^{\max}, \\ & \chi_j^{(i)} \in \{0,1\},\ \forall i \in \mathcal{M},\ \forall j \in \mathcal{U} \end{aligned} \tag{5.12}$$

where R_j is the achievable transmission rate of jth user, which is function of $\chi_j^{(i)}$ and given in (5.7). $P_{n_w}^{(i)}$ and $P_{n_s}^{(i)}$ represent the reflected optical power of the allocated mirror element for the user having poor and good channel condition, respectively. We assume that θ_d should lie between θ^{min} and θ^{max}. The solution to this problem tries to maximize the average rate per user while distributing mirror elements proportionally to maintain fairness regarding users' channel conditions. An observation of the objective function of (5.12) and the design constraints exhibit that this problem formulation constitutes a binary linear programming (BLP) problem. The above problem is analogous to a cellular network consisting of many users and fewer base stations, where a single user gets a connection from the base station at a given time. With the consideration of fairness among users, the problem of assigning multiple users to the base station is an NP-hard problem. Consequently, it is not possible to find the optimum solution in polynomial time [115]. The optimal solution to such a BLP problem can be attained via an exhaustive search of all possible combinations of mirror elements-user assignments. In an exhaustive search, the search of possible combinations exponentially grows with the number of users U and the number of available mirror elements M. Therefore, the polynomial time complexity of an

exhaustive search is high. Thus, we adopted a heuristic SMA scheme to find a near-optimal polynomial-time solution for such mirror element assignment problems.

5.4.3 Proposed Solution

Algorithm 5.1 Proposed signal strength based mirror element assignment (SMA) scheme

Input: M_j, F^*, and $\mathcal{P}_i$.
Output: A feasible mirror element assignment i^*
Let $M_j^f = M_j$

for all $i \in M_j$ **do**
  if $F_j < F^*$ **then**
    $M_j^f = M_j$-{i}
  else
    Compute $\mathcal{P}_i$ of each mirror element
  end if
end for
for all $i \in M_j$ **do**
  Sort the mirror elements in decreasing order of $\mathcal{P}_i$
end for
Let $\mathbb{G}$ be the sorted mirror elements list
if $\mathbb{G} = \phi$ **then**
  Identify the mirror elements that are on the top of $\mathbb{G}$, say k
  Return $i^* = k$
end if

An observation of our formulated optimization problem in (5.12) reveals that this formulation is established as a BLP problem, where the optimal solution to such optimization problem is NP-hard. Therefore, we propose a heuristic SMA scheme to solve efficiently (5.12), where appropriate mirror elements i^* are simultaneously assigned to each user so that the maximum average rate is achieved, subject to maintaining uniform fairness among users. To perform the optimal mirror element allocation, the CC of an OIRS-assisted UAV is required to know the user's location. The user's location information is sent to the CC via the uplink RF channel. Let M_j^f represent the feasible mirror element set. The proposed SMA scheme can be executed in polynomial time as follows: first, as per the user's location information, the proposed scheme assigns appropriate mirror elements to the users. The selection of the appropriate mirror elements is a function of the channel quality in order to keep a fair rate among the users. The proposed scheme adjusts mirror element assignment according to the current channel quality changes within the network's limits and maximizes the data transmission rate while ensuring fairness among the users. In our proposed scheme, when the user's channel condition is excellent, a lower number of mirror elements are assigned; thereby, the efficacy of transmission and OIRS utilization is improved. On the contrary, the higher number of mirror elements M is allocated to the users when the user's channel condition is not good. If all the users have excellent channel conditions, at least two mirror elements are assigned to users to maintain a fair rate among the users. The proposed scheme iterates until all M are assigned. As shown later, the SMA scheme is a fairer assignment of mirror elements because it considers the user's channel condition. Algorithm 5.1 shows the pseudocode of the SMA scheme.

Table 5.1: Simulation parameters for performance evaluations

Parameters	Simulation values
P_T	60 mW
$\Re$	0.5 A/W
A_{PD}	7 mm^2
λ	1550 nm
a	5 cm
$\mathcal{B}$	100 MHz
$G(\varphi)$	1
$C_n^2(0)$	1×10^{-13} $m^{-2/3}$
E_l in case of clear air	0.43
E_l in case of light fog	4.2
E_l in case of moderate rain	5.8
E_l in case of heavy rain	9.2
σ_j	30 cm
σ_n^2	$10^{-15} A^2/Hz$
θ^{min}	0.05 mrad
θ^{max}	1.5 mrad

5.5 Performance Evaluation and Discussions

In this section, we show the validation of closed-form expressions via Monte Carlo simulations. For the performance evaluation, the average rate, fairness index, rate outage probability, and average sum rate are computed via Monte Carlo simulations. In addition, we investigate and compare the performance of our proposed scheme with respect to benchmark schemes such as EMA, NOMA, and TDMA. The considered simulation parameters are summarized in TABLE 5.1. In this chapter, we consider OIRS-assisted UAV-based FSO networks with $U = |\mathcal{U}|$ user and $M = |\mathcal{M}|$ mirror elements of the OIRS. We assume that mirror-based OIRS is deployed on the UAV, and the OIRS-assisted UAV is hovered at 100 m vertical height. The distance between the optical transmitter and the OIRS-assisted UAV is assumed to be 500 m, and the optical transmitter is located at a height of 10 m. U mobile users are distributed in the outdoor region of 400 m $\times$ 400 m. We consider that the receiver of the user is at a height of 0.85 m. To investigate the outage performance, this chapter considers the SNR threshold of $\gamma_{th} = 5$ dB.

Table 5.2: Performance comparison of different schemes

Schemes	For $M = 9$ & $U = 3$		For $M = 16$ & $U = 4$	
	Average sum rate (bps/Hz)	Fairness index	Average sum rate (bps/Hz)	Fairness index
Exhaustive search	12.1	0.97	12.5	0.99
SMA	3.2	0.95	4.6	0.98
EMA	2.6	0.90	3.5	0.97

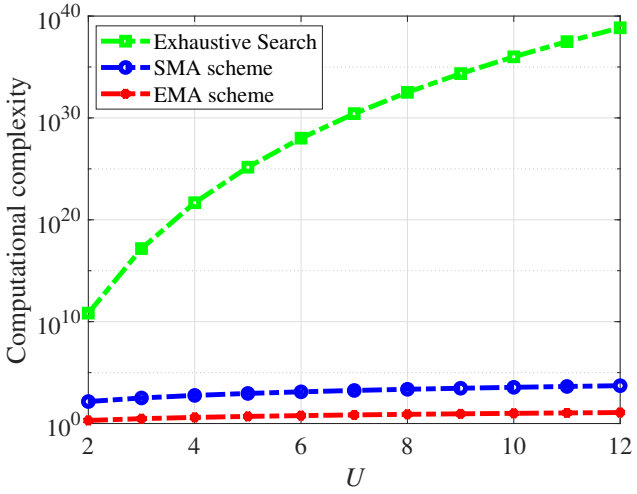

Figure 5.3: Computational complexity comparison of different schemes.

5.5.1 Mirror Element assignment with Small Configuration

In this subsection, for the simulations, two types of mirror-based OIRS configurations are considered with dimensions of $M = 9$ and $M = 16$ mirror-based OIRS. The proposed system model with the mentioned OIRS configurations for $U = 3$ and $U = 4$ is simulated. The fairness and sum rate performance of the proposed system in the case of exhaustive search, SMA, and EMA schemes are shown in TABLE 5.2. The exhaustive search takes an exponentially longer duration for the higher U and M. Therefore, it is hard to simulate the considered scenario with many users and mirror elements by exhaustive search. The running time of different schemes with the exhaustive search is compared and shown in Fig. 5.3, further validating that the exhaustive search is infeasible to implement even with fewer users. In TABLE 5.2, we list the values of the average rate and the fairness index in the case of exhaustive search, SMA, and EMA when $U = 3$ and $U = 4$.

Fig. 5.3 depicts the computational complexity of exhaustive search, SMA, and EMA schemes. We use big-$\mathcal{O}$ notation for the computational complexities analysis as it offers a generalized upper bound performance. It can be observed that the running time for exhaustive search is exponentially growing when U increases. An exhaustive search is computationally expensive as it searches over all the possibilities for mirror element assignment of the users. Therefore, the complexity is $\mathcal{O}(U^M)$. There are U^M different likelihoods to allocate mirror elements to each user, which needs U^M iterations. Furthermore, compared to the EMA, the time complexity of the SMA scheme is remarkably higher. The computational time for SMA is $\mathcal{O}(U^2 \times M)$. The algorithm 5.1 has two loops, and n is the total number of iterations. In the case of the EMA, the running time is proportional to n. Therefore, its time complexity is $\mathcal{O}(n)$.

5.5.2 Mirror Element assignment with Large Configuration

In this sub-section, we present a comparative evaluation of the SMA, EMA, NOMA, and TDMA performance when $M = 36$. The performance comparison is evaluated in terms of average rate per user, fairness, rate outage probability, and sum rate. Fig. 5.4 (a) illustrates the average rate per user as a function of U for all schemes

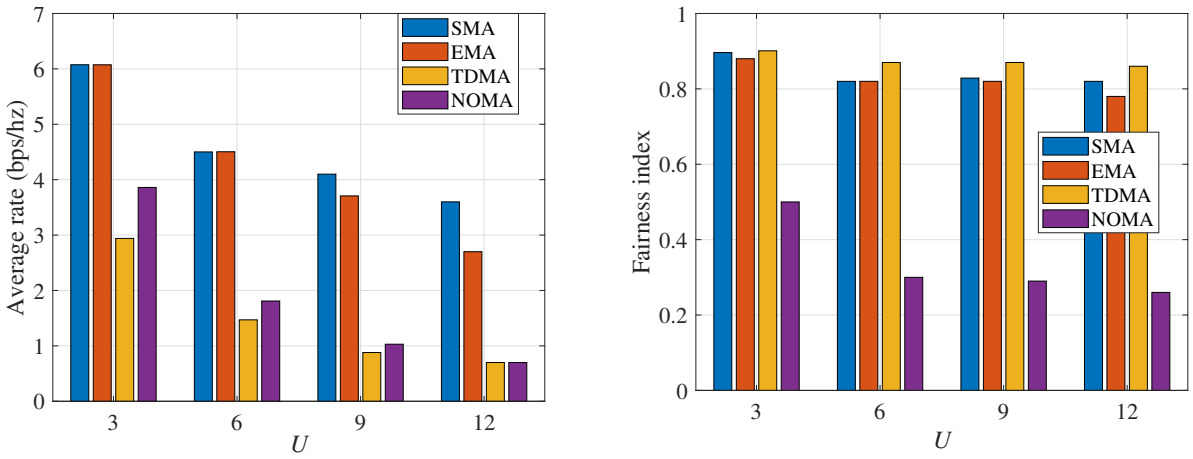

Figure 5.4: (a) Average rate performance of the SMA, NOMA, EMA, and TDMA scheme versus the number of users U. (b) Fairness index of the SMA, NOMA, EMA, and TDMA scheme versus the number of users U.

when $M = 36$. The proposed SMA scheme has remarkable rate improvements over other schemes. It is also noted that the average rate per user degrades as U increases. However, the SMA significantly performs better, even when U is high. This is because the proposed SMA assigns each user the best M mirror elements. For instance, the SMA provides an average rate of 3.6 bps/Hz when $U = 12$. On the other hand, the EMA achieves an average rate of 2.85 bps/Hz when $U = 12$. It is also noted that the TDMA offers lower rate performance, followed by the NOMA, irrespective of U. For instance, NOMA and TDMA provide an average rate per user of less than 1 bps/Hz when $U = 12$. Therefore, the SMA scheme improves the average rate and achieves a rate by up to 26% compared to the EMA scheme.

In Fig. 5.4 (b), we plot the fairness index of SMA, NOMA, EMA, and TDMA for the numbers of users $U =$ 3, 6, 9, and 12 when $M = 36$. This figure indicates that TDMA, EMA, and SMA schemes obtain maximum fairness for $U = 3$. It is evident that the TDMA offers remarkably improved fairness performance compared to other schemes. This fairness enhancement is because all the mirror elements are simultaneously assigned to the particular user. It can be seen that the SMA scheme achieves a uniform transmission rate with respect to NOMA and EMA. This is due to adoption of a fair assignment strategy of mirror elements in the proposed scheme. For instance, the proposed scheme offers a higher than 0.85 fairness index when $U = 12$. Fig. 5.5 (a) illustrates the rate outage probability as a function of R_D for the SMA, EMA, NOMA, and TDMA schemes when $U = 12$. The proposed SMA scheme acquires a rate outage probability of 10^{-3} for a lower demand rate R_D. However, as the demand rate R_D increases from 3 to 7 bps/Hz, all schemes do not significantly reduce the rate outage probability. The SMA can support the R_D of 2.5 bps/Hz when the rate outage probability is 10^{-2}. On the other hand, the EMA can support only up to 2 bps/Hz. However, When $R_D > 3$ bps/Hz, NOMA and TDMA offer rate outage probability close to 1. Therefore, it is evident that compared to other schemes, the SMA scheme enables the network to support required demand rates R_D for a given QoS constraint. Fig. 5.5 (b) shows the average sum rate as a function of U for all schemes when $M = 36$. It is shown that the highest sum rate performance can be achieved by utilizing our proposed scheme. The achieved average sum rate in

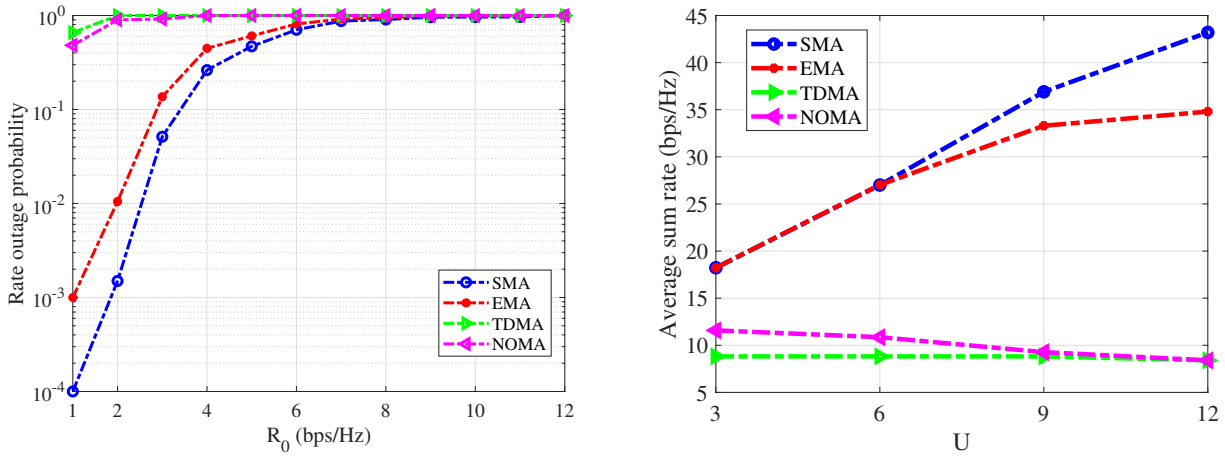

Figure 5.5: (a) Rate outage probability performance of the SMA, EMA, NOMA, and TDMA scheme versus required demand rate R_D, when $U = 12$. (b) Achieved sum rate of the SMA, NOMA, EMA, and TDMA scheme versus the number of users U.

the case of SMA and EMA persistently improves when U increases. In the case of the EMA, an equal M is assigned to the user without considering the channel quality. The EMA offers less sum rate improvement even at higher U due to the inadequate number of mirror elements. However, when $U = 12$, the SMA remarkably enhances the sum rate to 43.2 bps/Hz. On the other hand, EMA can only provide a sum rate of 36 bps/Hz. However, the average sum rate degrades for NOMA as U increases. This is expected as the rising U increases the inter-user interference. In that case, approximately equal power is distributed among the interfering users, as corroborated in (5.9) and (5.10). TDMA offers the lowest average sum rate among users compared to other schemes since all the mirror elements serve only one user at a time.

Fig. 5.6 illustrates the achieved sum rate of the SMA and other schemes with respect to transmit power P_T when $U = 12$. It can be observed that the average sum rate increases with an increase in P_T. This figure also indicates that the SMA scheme offers a maximum average sum rate over EMA, NOMA, and TDMA. For instance, SMA provides an average sum rate of 41.6 bps/Hz when $P_T = 20$ dBm, whereas the EMA achieves an average sum rate of 37.9 bps/Hz. Fig. 5.6 reveals that NOMA and TDMA do not show substantial improvement even with an increase in P_T. The sum rate performance is confined to 9.95 bps/Hz at $P_T = 20$ dBm in the case of NOMA and TDMA. However, there is a significant sum rate gain at a lower P_T, and the sum rate increases more slowly at a higher P_T. It's worth noting that the performance of NOMA and TDMA would reach their peak as the maximum transmission power increases to a certain threshold. Therefore, our proposed SMA scheme improves the average sum rate in OIRS-assisted UAV-based FSO networks compared to conventional schemes.

5.6 A Use case: Emergency Communication in Post-Disaster Zones

After a major earthquake in a dense urban area, traditional cellular infrastructure is heavily damaged or non-functional. Emergency teams need a rapid-deployment communication system to maintain situational awareness and coordinate relief efforts. A fleet of UAV equipped with FSO transceivers and OIRS is deployed

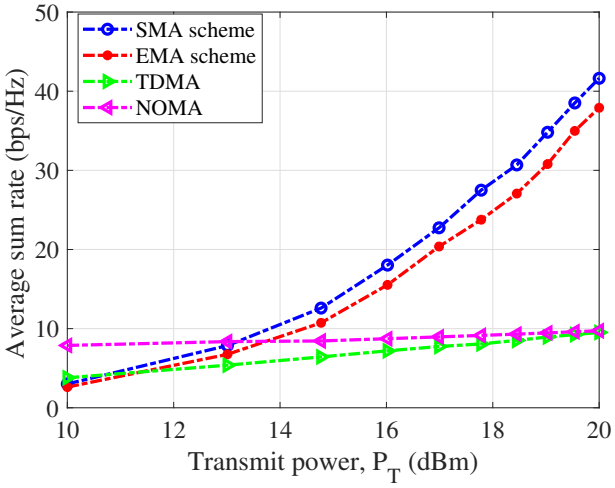

Figure 5.6: Achieved sum rate performance of the SMA, NOMA, EMA, and TDMA scheme versus transmit power P_T, when $U = 12$.

over the disaster zone. These UAVs establish high-throughput, low-latency optical communication links between temporary ground stations and mobile emergency response units. The SMA algorithm is used in this case to dynamically allocate mirror elements to multiple emergency units (ambulances, drones, field officers), optimizing the signal strength and ensuring that each unit receives sufficient bandwidth to transmit live video feeds, medical data, and GPS coordinates.

5.7 Optimizing OIRS-Assisted UAV-based FSO Networks: Key Findings and Insights

In this chapter, we investigate the performance of a downlink OIRS-assisted UAV-based FSO network. In the proposed network, we assumed an FSO link between the optical transmitter, the OIRS-assisted UAV, and between the OIRS-assisted UAV and the user. The FSO link is impacted by four channel impairments: atmospheric turbulence, atmospheric attenuation, beam misalignment error, and AoA fluctuations. Furthermore, we have derived the closed-form expression for the outage probability of the proposed network under the impact of channel impairments, which is further validated through simulations. Furthermore, we investigated the problem of mirror-element assignment in the proposed networks. We developed an optimization problem that maximizes the average rate per user while satisfying the user fairness and QoS design constraints. In order to offer a higher average rate with uniform fairness among the users, an efficient mirror element assignment scheme, i.e., SMA, is suggested, where mirror elements are optimally assigned to the users. In addition, we compared the SMA scheme's performance against another heuristic scheme, i.e., the EMA scheme, and conventional benchmark schemes like TDMA and power-domain NOMA. The reported results showed that the proposed SMA appreciably improves the rate per user, especially for more users. Our simulation results exhibited that SMA scheme has the potential to offer a fair data rate among multiple users.

5.8 Enhancing Indoor OWC Systems: Laser-Based Communication and OIRS-Assisted UAV Integration

In recent years, indoor OWC-based systems have been realized in which a LED is utilized as the source for downlink communication and illumination. On the other hand, RF or infrared light has been used for uplink communication. In some recent works, the laser diode has also been used as an optical source for downlink communication in place of the LED. The laser diode has its benefits, such as wide electrical bandwidth. However, this advantage comes at the expense of the strict transmit optical power limitation per the eye safety regulations IEC 60825-1. To deal with such transmit power limitation, vertical-cavity surface-emitting laser (VCSEL) can achieve a higher rate while maintaining eye safety limits [116, 117].

In indoor scenarios, the received optical power of the user's receiver depends on the distance between the optical source and the user. Furthermore, in a multi-user indoor scenario, objects inside the room act as blocks, resulting in a sudden drop in the optical power received, as it can block the signal from the optical source to the desired user [118]. Consequently, the network can suffer significant data loss if the blockages obstruct the direct optical link. UAV and OIRS are potential solutions to alleviate the effect of blockages and non-LoS in 6G indoor wireless communication networks [55], [56]. Subsequently, the performance of OIRS has been analyzed for OWC-based systems in [18]. OIRS is envisioned to improve the performance of indoor communication networks, specifically in the case of the non-availability of LoS links [18]. Furthermore, the LoS requirement can be alleviated by installing an OIRS-assisted UAV as a mobile relay between the optical transmitter and the optical receiver [53]. Therefore, from the above, it is evident that both OIRS-assisted UAV and laser-based communication can significantly enhance the performance of conventional OWC-based indoor wireless networks. However, such system integration possesses several design challenges in terms of optimal user selection and OIRS-assisted UAV mirror element assignment to improve system performance.

There is considerable literature on laser-based OWC technology for indoor communication networks [116, 117, 119–123]. In [116], the authors investigated the performance of a high-speed imaging receiver that can aid mobility under the effects of two widely known trade-offs, i.e., gain FoV and area-bandwidth. In [117], the authors analyzed the OWC backhaul system designed for indoor applications, aiming at a data rate of at least 1 Tbps under the constraint of eye safety. In [120], the authors demonstrated an ultrahigh-speed OWC transmission with a simultaneous beam tracking and steering capability system that can achieve a data rate of more than 1 Tbps in the indoor communication network. In [119], the OWC link based on VCSEL arrays provides data rates above 1 Tbps for the backhaul of 6G indoor wireless networks. The authors presented comprehensive analytical modeling of the misalignment for OWC links with Gaussian beams. In [121], the all-optical bidirectional optical communication system is analyzed, incorporating the beam steering transmitter, the wide FoV optical receiver, and the localization of the user's devices to support up to 128 optical beams transmitting up to 112 Gbps per beam. In [122], the authors presented the design, implementation, and performance evaluation of fiber-wireless-fiber terminals for OWC with realistic coverage that provides a bi-directional free-space connection between fiber optic transceivers. The performance of a hybrid laser-LED-based transmitter to achieve a total data rate of 5.15 Gbps for the diffuse laser beam with steering is analyzed in [123].

5.8.1 Motivation

As evident from the above, although there has been considerable work on laser-based indoor wireless communication networks, the performance of OIRS-assisted UAV and laser-based communication in indoor networks has not yet been well investigated. Most existing studies emphasized the realization of optical transmitters using an array of VCSEL or LED. The future 6G indoor communication network will provide users with a high data rate. Therefore, in this chapter, we propose to utilize a laser-based source that can provide a high data rate to mobile users. However, one of the potential drawbacks of the laser-based source is that it always needs to maintain a LoS between the optical transmitter and the optical receiver due to its coherent nature. The deployment of OIRS-assisted UAVs between the optical transmitter and the optical receiver can mitigate this LoS requirement in indoor scenarios. The OIRS converges the optical beam toward the required direction by changing the orientation of each mirror element.

5.8.2 Contributions

The key contributions of Part II of this chapter are outlined as follows:

- We analytically formulate the batch-based mirror-element assignment problem as a non-linear binary programming optimization problem and reformulate the optimization problem as a BLP, which is generally NP-hard.
- For a given coverage of an OIRS-assisted UAV system, we propose a sub-optimal solution based on batch-based polynomial-time sequential-fixing linear programming (BSFLP), where the mirror elements are iteratively assigned to a subset of the contending users simultaneously by solving a sequence of linear programs.
- Also, we measure the number of served users, sum rate, and fairness for the BMEA scheme and compare its performance with respect to the SMA and EMA schemes mentioned in [12].

5.9 System Model and Power Analysis

5.9.1 System Model

We consider OIRS-assisted UAV and laser-based indoor communication networks as shown in Fig. 5.1. The optical transmitter is equipped with a VCSEL array installed at one of the side walls to send the data to the particular OIRS-assisted UAV via an optical link. Further, we consider an OIRS-assisted UAV and laser-based indoor communication network of a cluster with a set of $\mathcal{U}$ users, where $U = |\mathcal{U}|$ is the number of contending users. The U users are distributed in an indoor space of 3D coordinate systems (x, y, z). Suppose $\mathcal{M}$ is the set of M mirror elements in the OIRS, where $M = |\mathcal{M}|$ is the number of mirror elements of the OIRS. We consider that a set of $\mathcal{U}$ users are competing to access a set of $\mathcal{M}$ mirror elements. The maximum number of mirror elements assigned to each user is limited to $\kappa \leq M$ mirror elements. Further, we assume that the large indoor space is divided into clusters, and one OIRS-assisted UAV provides coverage in the entire cluster space such that the QoS is guaranteed to the users. We assume that in each cluster, the optical transmitter

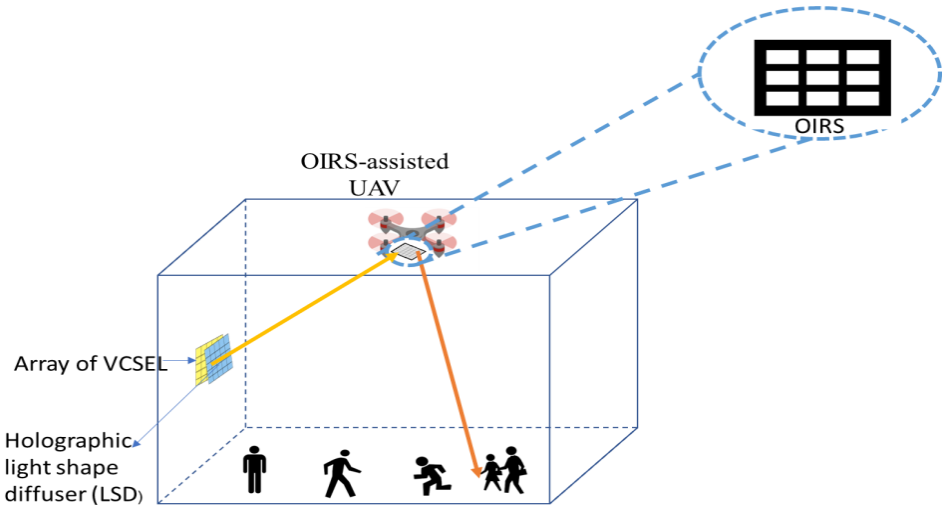

Figure 5.7: The proposed OIRS-assisted UAV and laser-based indoor communication network

is equipped with a VCSEL array that is installed at one of the side walls to send the data to the particular OIRS-assisted UAV via an optical link as shown in Fig. 5.7. The UAV is equipped with the OIRS to beamform and reflect the beam toward the targeted user as in [53], [17]. The optical signal transmitted from the VCSEL array passes through a holographic light-shaped diffuser (LSD) to obtain a uniform optical power distribution on the OIRS's surface as shown in Fig. 5.7. The maximum permissible transmit power of the VCSEL is set as per the eye safety regulations standard such that $P_T = P_{t_{max}}$. The eye safety details considered to obtain $P_{t_{max}}$ can be found in [124]. It is worth mentioning that a laser source is said to be eye-safe if the fraction of incident optical power into the eye aperture at the most hazardous position for an exposure time should not be greater than the maximum permissible exposure multiplied by the aperture area of the eye [116]. Further, we assume a downlink transmission scenario, where a VCSEL array simultaneously transmits data to several mobile users via optical signals in a broadcasting mode. The position of each VCSEL, UAV, user, and mirror element of the OIRS is given in a 3D coordinate system (x, y, z). Further, we assume that the incoming optical light from the hovering OIRS-assisted UAV is focused on the surface of the PD of user's receiver the with the help of the converging lens [125]. When an incident beam passes through a converging lens, the width of the beam footprint in the PD is approximately equal to 2.4λ, and it is much smaller than the conventional radius of the PD that is commonly in the order of mm [126]. We consider that the UAV employs an indoor localization mechanism to transmit its location information to the optical transmitter in the form of beacon messages [127]. The optical transmitter extracts the beacon message from an OIRS-assisted UAV to compute the distance between the VCSEL and OIRS-assisted UAV. According to the UAV's location, VCSEL aims the optical beam toward the OIRS plane of OIRS-assisted UAV. Further, the orientation of each mirror element is controlled by a CC of an OIRS-assisted UAV via an error-free RF link. Moreover, CC facilitates uplink RF reception from contending users to announce their control and location information.

5.9.2 Power and Rate Analysis in OIRS-assisted UAV and Laser-based Indoor Communication Network

The optical beam incident from the VCSEL follows a Gaussian power intensity profile [128]. Initially, at the beam waist, the wavefront of the optical beam is planar and expands further in the beam's propagation direction. The wavefront radius of curvature at a distance L_1 from the VCSEL is defined by ω_{L_1} and is computed as [119]:

$$\omega_{L_1} = \omega_0 \sqrt{1 + \left(\frac{\lambda L_1}{\pi \omega_0^2}\right)^2}, \tag{5.13}$$

The optical intensity distribution at a distance L_1 from the VCSEL is expressed as [119], [128]:

$$P(x,y) = \frac{2P_T}{\pi \omega_{L_1}^2} \exp\left(-\frac{2\varepsilon^2(x,y)}{\omega_{L_1}^2}\right), \tag{5.14}$$

where ε $(x,\ y)$ represents the Euclidean distance of the point $(x,\ y)$ from the center of beam footprint and P_T is the transmitted optical power. We also consider that the optical beam from VCSEL is passed through the holographic LSD to improve the radius of the beam's footprint on the OIRS's surface. Holographic LSDs, along with different angles, are utilized to expand the beam footprint of the VCSEL with uniform optical power distribution [129]. The effective divergence angle of the light source can be extended by using holographic LSD to $\theta_e \approx \sqrt{(\theta_d)^2 + (\theta_{LSD})^2}$, where θ_e is the effective divergence angle of the optical beam, θ_d is the divergence angle of VCSEL, and θ_{LSD} is the angle of LSD. The calculation of beam intensity through holographic LSD has been simplified in [129], where LSD is divided into an array of pixels, and the beam intensity is assumed to be uniform for a tiny beam profile after passing via a single pixel. Therefore, the effective radius of beam footprint by a VCSEL after passing via LSD at a distance L_1 can be obtained as:

$$\omega_{L_e} = L_1 \tan(\theta_e). \tag{5.15}$$

Recall that the considered OIRS comprises an array of mirror elements reflecting the optical signal from the optical transmitter to the optical receivers and their orientation angle θ_i is already defined in Chapter 2. The received power density distribution P_i on the surface of OIRS is computed as in [17]:

$$P_i(x,y) = \frac{\mathcal{K} A_c^2}{\omega_{L_e}^2} exp\left[-\frac{2((x+x_i)^2 + (y+y_i)^2)}{\omega_{L_e}^2}\right], \tag{5.16}$$

where A_c represents the central amplitude of the optical signal and $\mathcal{K}$ is power factor. When the set of selected mirror elements $(\Omega_j \subseteq \mathcal{M})$ are focused at jth user, power density distribution $P_j(x,y)$ at jth user is given as [17].

$$P_j(x,y) = \frac{\mathcal{K} A_c^2}{\omega_{L_F}^2} \sum_{j=1}^{j=U} \sum_{i \in \Omega_j} \exp\left[-\frac{2((x+x_i-x_j)^2 + (y+y_i-y_j)^2)}{\omega_{L_F}^2}\right] \cos\theta_i, \tag{5.17}$$

where Ω_j is the set of assigned mirror elements to the jth user. Therefore, the SNR of the jth user is calculated as

$$\gamma_j = \frac{\left[\Re_j P_j(x,y) A_{PD_j} h_{AoA}\right]^2}{n\mathcal{B}}, \tag{5.18}$$

where n_c is the AWGN with zero mean and variance σ_n^2. h_{AoA} denotes link interruption due to AoA fluctuations and $\mathcal{B}$ is the bandwidth. Due to the hovering of the UAV, AoA fluctuations are introduced in the proposed system, which degrades the performance as the user's receivers have limited FoV [111]. Although the optical beam is focused on the PD's plane with the help of the lens, the AoA of the optical beam diverges from the normal line due to the random orientation deviation of the OIRS-assisted UAV. Therefore, to capture the effect of AoA fluctuations due to the hovering of the OIRS-assisted UAV, the optical channel under AoA fluctuations (h_{AoA}) is modeled as [111]: $h_{AoA} = \Pi\left(\theta_{AoA}/\Psi_{FoV}\right)$, where $\Pi(w) = 1$ if $|w| \leq 1$, and $\Pi(w) = 0$ otherwise. Ψ_{FoV} is the FoV angle of the user's receiver. θ_{AoA} is the incidence angle of the beam on the normal axis of the user's receiver plane, and its PDF follows the Beckmann distribution with variance σ_{AoA}^2 [111]. Accordingly, the achievable rate of jth user is calculated as in [130]:

$$R_j = \frac{1}{2}\log_2(1+\gamma_j). \tag{5.19}$$

5.10 Problem Statement and Problem Formulation

5.10.1 Problem Statement

Given the above system model of a cluster, our problem statement is as follows: given the set of contending users $\mathcal{U}$, required rate demand R_j^D for each user $j \in \mathcal{U}$, the set of available mirror elements $\mathcal{M}$, the total allowable mirror elements per user K, and the optimal orientation angle of each mirror element $\theta_j^{(i)*}$ as given in [17], our objective is to determine the appropriate users-selection and mirror-element assignment that jointly achieve the design objective of simultaneously serving the maximum possible number of users subject to the following design constraints:

C.1.) **Rate demand satisfaction**: This constraint ensures that the rate demand of each user j (R_j^D) is satisfied by assigning the required mirror elements for that user.

C.2.) **Mirror element exclusive-use constraint**: This constraint ensures that each mirror element cannot be assigned to more than one user.

C.3.) **Hardware constraint**: This hardware constraint ensures that each user can be assigned at most $\kappa \leq |\mathcal{M}|$ elements.

5.10.2 Problem Formulation

To proceed with our analysis, the binary decision variable $\chi_j^{(i)}$ is defined as follows:

$$\chi_j^{(i)} = \begin{cases} 1, & \text{if mirror element } i \text{ is allocated to user } j \\ 0, & \text{otherwise.} \end{cases} \tag{5.20}$$

Let $R_j^{(i,\theta_j^{(i)*})}$ represent the achieved rate of jth user with respect to mirror element i at an orientation angle $\theta_j^{(i)*}$. Mathematically, our objective function can be written as:

$$\sum_{j\in\mathcal{U}} \mathbf{1}\left[\sum_{i=1}^{M} \chi_j^{(i)} \geq 1\right], \tag{5.21}$$

where $\mathbf{1}[.]$ represents the indicator function. Given the objective function in (6.21) and design constraints given in (C1–C3), our optimization problem for the $|\mathcal{U}|$ contending users can be formulated as:

$$\begin{aligned}
\mathbf{P1}: &\max_{\chi_j^{(i)}} \sum_{j\in\mathcal{U}} \mathbf{1}\left[\sum_{i=1}^{M} \chi_j^{(i)} \geq 1\right] \\
s.t.\ &\sum_{i\in\mathcal{M}} R_j^{(i,\theta_j^{(i)*})} \chi_j^{(i)} \geq R_j^D \text{ or } \sum_{i\in\mathcal{M}} R_j^{(i,\theta_j^{(i)*})} \chi_j^{(i)} = 0,\ \forall j \in \mathcal{U} \\
&\sum_{j\in\mathcal{U}} \chi_j^{(i)} \leq 1,\ \forall i \in \mathcal{M} \\
&\sum_{i\in\mathcal{M}} \chi_j^{(i)} \leq \kappa,\ \forall j \in \mathcal{U}.
\end{aligned} \tag{5.22}$$

It may be noted that it is difficult to optimize the indicator function. Therefore, we linearize our objective function by introducing a new binary variable ν_j and adding two linear constraints as follows:

$$\nu_j = \mathbf{1}\left[\sum_{i=1}^{M} \chi_j^{(i)} \geq 1\right],\ \forall j \in \mathcal{U}, \tag{5.23}$$

$$\begin{aligned}
\frac{\sum_{i\in\mathcal{M}} \chi_j^{(i)}}{|\mathcal{M}|} - \nu_j \leq 0,\ \forall j \in \mathcal{U}, \\
\nu_j - \sum_{i\in\mathcal{M}} \chi_j^{(i)} \leq 0,\ \forall j \in \mathcal{U}.
\end{aligned} \tag{5.24}$$

It may be noted that if any of the $\chi_j^{(i)}$ of the jth user is not 0, the jth user is going to be served. While if all $\chi_j^{(i)}$'s of the jth user are 0, no feasible mirror element assignment can be obtained for user j, and therefore, that jth user will not be served. If several feasible solutions with the same maximum number of served users exist for the optimization problem, we seek to find the solution that can achieve the highest rate. For achieving this, we add the following term $[\frac{\sum_{j\in\mathcal{U}}\sum_{i\in\mathcal{M}} \chi_j^{(i)} R_j^{(i,\theta_j^{(i)*})}}{\mathbb{R}}] < 1$ to the objective function, where $\mathbb{R} = \sum_{j\in\mathcal{U}}\sum_{i\in\mathcal{M}} R_j^{(i,\theta_j^{(i)*})}$. It may be noted that the added term is always less than one, ensuring that it only impacts those mirror element assignments with the same maximum number of served users. To further simplify our optimization problem, we introduce two more auxiliary binary variables $y_1^{(j)}$, $y_2^{(j)}$ and replace the either/or constraint in (6.29) with the following set of linear constraints:

$$\begin{aligned}
&\sum_{i\in\mathcal{M}} -R_j^{(i,\theta_j^{(i)*})} \chi_j^{(i)} \leq -R_j^D + \Xi y_1^{(j)}, \forall j \in \mathcal{U} \\
&\sum_{i\in\mathcal{M}} R_j^{(i,\theta_j^{(i)*})} \chi_j^{(i)} \leq 0 + \Xi y_2^{(j)}, \forall j \in \mathcal{U} \\
&y_1^{(j)} + y_2^{(j)} = 1, \forall j \in \mathcal{U},
\end{aligned} \tag{5.25}$$

where $\Xi \gg 1$. Based on (6.30),(6.31),(6.32), and adding the constraints, the optimization problem in (6.29) can be rewritten as:

$$
\begin{aligned}
\mathbf{P1}: \max_{\chi_j^{(i)}} & \sum_{j\in\mathcal{U}} \nu_j + \frac{\sum_{j\in\mathcal{U}}\sum_{i\in\mathcal{M}} \chi_j^{(i)} R_j^{(i,\theta_j^{(i)*})}}{\mathbb{R}} \\
s.t. \ & \sum_{i\in\mathcal{M}} -R_j^{(i,\theta_j^{(i)*})}\chi_j^{(i)} \leq -R_j^{D} + \Xi y_1^{(j)}, \forall j \in \mathcal{U} \\
& \sum_{i\in\mathcal{M}} R_j^{(i,\theta_j^{(i)*})}\chi_j^{(i)} \leq 0 + \Xi y_2^{(j)}, \forall j \in \mathcal{U} \\
& \sum_{j\in\mathcal{U}} \chi_j^{(i)} \leq 1, \ \forall i \in \mathcal{M} \\
& \sum_{i\in\mathcal{M}} \chi_j^{(i)} \leq \kappa, \ \forall j \in \mathcal{U} \\
& \frac{\sum_{i\in\mathcal{M}} \chi_j^{(i)}}{|\mathcal{M}|} - \nu_j \leq 0, \ \forall j \in \mathcal{U}, \\
& \nu_j - \sum_{i\in\mathcal{M}} \chi_j^{(i)} \leq 0, \ \forall j \in \mathcal{U} \\
& y_1^{(j)} + y_2^{(j)} = 1, \forall j \in \mathcal{U}.
\end{aligned} \tag{5.26}
$$

5.11 The Proposed User-Selection and Mirror-Element Assignment Scheme

The formulated problem in (6.33) is a BLP, a combinatorial multi-mirror elements multi-user matching problem, which is NP-hard. The optimal solution to this optimization problem can be derived by an exhaustive search of all possible combinations of mirror-user assignments, exponentially growing with the number of competing users U and the number of available mirror elements M. Thus, the BSFLP approach is adopted to obtain near-optimal polynomial-time solutions for our optimization problem in (6.33). The BSFLP approach has been followed by several research efforts to resolve the same BLP problems, by which sub-optimal solutions with polynomial time complexity were exhibited [131], [132], [133]. The BSFLP procedure adopted for such a BLP problem is carried out as follows:

Step 1: Relax all unfixed binary variables $\chi_j^{(i)}$ to real values in the range [0, 1], forming a relaxed linear programming (RLP) problem.

Step 2: Solve the RLP problem. If the RLP has no feasible solution, then the BLP in (6.33) also has no feasible solution. If the RLP has a feasible solution, identify the user's transmission with the highest $\chi_j^{(i)}$ sum among the U users.

Step 3: The decision variable with the highest value among all unfixed χ's of the identified user is assigned a value of 1. Subsequently, the RLP is updated and resolved with the fixed χ. If no solution is found, then fixing it to 1 is incorrect, and instead, the highest χ must be fixed to 0.

Step 4: Repeat **Steps 2** and **3** until the required rate is met with the highest sum of χ values in **Step 3**. Then, fix all remaining unfixed χ values related to this user's transmission to 0. If all χ values associated with this user's transmission are fixed without meeting the required rate, this user's transmission will be blocked (set all

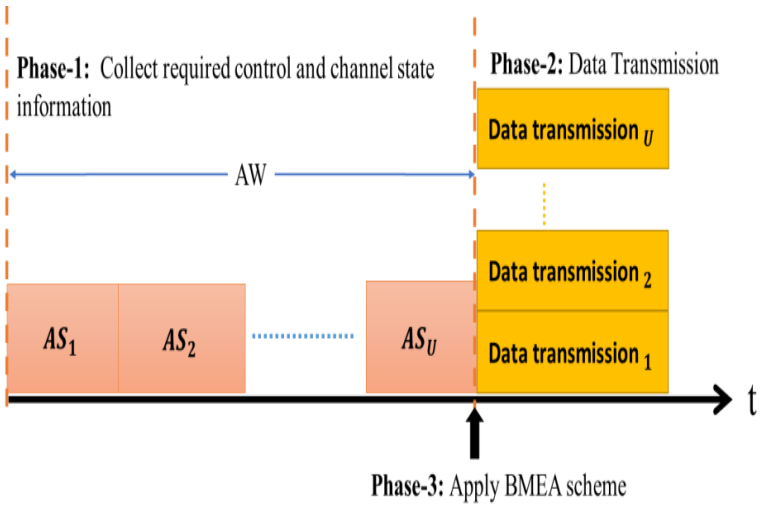

Figure 5.8: The procedure of the proposed BMEA scheme

χ values for this user's transmission to 0).

Step 5: Identify the next unserved user's transmission with the highest summation of unfixed χ values. Then, repeat **Steps 3-4** for the selected user, taking into account the mirror element assignments of previously served users.

Step 6: Repeat **Step 5** until each user is either assigned a set of mirror elements that satisfies its QoS demands or it is determined that no feasible mirror element assignment is possible.

The time complexity of the BSFLP scheme is bounded by the complexity of the RLP solver. Because an RLP solver has a polynomial complexity, the complexity of our BSFLP algorithm is also polynomial. In the worst case, the RLP produces a non-feasible solution at each iteration. Therefore, one variable is always fixed to 0. The complexity of each RLP instant is $\mathcal{O}(f(n))$, where $f(n)$ is a polynomial function of n. Therefore, the computational complexity of the BSFLP scheme is n times the complexity of the RLP, resulting in the polynomial complexity in n. It is worth noting that admission control based on access window (AW) is based on passive learning [131, 134]; therefore, it does not introduce any time complexity to the proposed user-selection and mirror-element assignment scheme. To realize our proposed user-selection and mirror-element assignment optimization in a distributed way, we develop an AW-based admission control strategy with U access slots (AS) with a fixed duration, where $U \subseteq \mathcal{U}$ and $\mathcal{U}$ is the total number of contending users in the networks. Each AS is enough to exchange the control and channel state information required for each user j to the CC. The size of the AW can be adaptively adjusted according to the dynamics of user traffic. Users contend to access each AS over the RF control channel using a carrier sense multiple access with collision avoidance (CSMA/CA) approach. As stated above, our proposed protocol allows AW to be dynamically formed. Specifically, a potential user who senses a free RF control channel and is not aware of any active AW starts its own AW. Users contend to access the next AS using a CSMA/CA approach, as shown in Fig. 5.8. This process continues until the last AS in the AW. After all control and channel state information exchanges occur, the CC will have all the necessary information to perform the proposed user selection and mirror element assignment optimization. After that, data transmission proceeds according to the computed mirror element assignment and user selection decision

Table 5.3: Simulation parameters considered in OIRS-assisted UAV and laser-based indoor communication network.

Parameters	Simulation values
λ	950 nm
P_T	10 mW
$\Re_j$	0.5 A/W
A_{PD_j}	2 cm^2
Noise figure of the TIA	5 dB
Temperature	300 K
Load resistance	500 ohm
Ψ_{FoV}	40 mrad

outcomes.

5.12 Results and Discussion

This section investigates and compares the performance of the BMEA scheme against the reference SMA and EMA schemes [12]. In the EMA scheme, the total mirror elements of the OIRS are equally scaled for the total number of users. Each user receives the reflections from a set of an equal number of mirror elements. Furthermore, mirror elements are allocated to each user to maximize the rate and ensure user fairness. However, the SMA scheme is a heuristic algorithm that does not guarantee to ensure the user's required rate demand while assigning mirror elements to the users. Moreover, in the SMA scheme, the selection of users is not made for the optimal mirror element assignment. We investigate the performance of the proposed system in terms of the average sum rate, number of served users, and fairness. For fairness evaluation, Jain's fairness index is considered and is expressed as [135].

5.12.1 Simulation Setup

We consider an OIRS-assisted UAV and laser-based indoor communication network with $U = |\mathcal{U}|$ contending users and $M = |\mathcal{M}|$ mirror elements of the OIRS. We also consider a VCSEL transmitter, which operates at 950 nm with a beam radius of 5 m. A holographic LSD is placed before the VCSEL source to generate an optical beam spot on the OIRS's surface. The maximum permissible transmit power of 10 mW is considered according to the eye safety limits, which fulfill a power-limited policy [124]. We consider a large indoor space with a side length of 20 m, as shown in Fig. 5.7. We assume that VCSEL is installed on the side wall of the indoor space of 20 m $\times$ 20 m $\times$ 5 m at a height of 2 m. The OIRS-assisted UAV is assumed to be located at a height of 4 m. We consider that mirror-based OIRS is deployed on the UAV, and U users are uniformly distributed in an indoor area of 20 $\times$ 20 m^2. The height of the user's receiver is assumed to be 0.85 m. In this chapter, we assume that each mirror element can be regarded as a square with a side length of 2 mm [17]. The practical spacing between the adjacent mirror elements is demonstrated in [17] to be 1 mm. We set $R_j^D = R_D, \forall j \in U$. The proposed network is enforced and simulated using MATLAB programs. The rest of the simulation parameters adopted for performance evaluation are presented in TABLE 6.2.

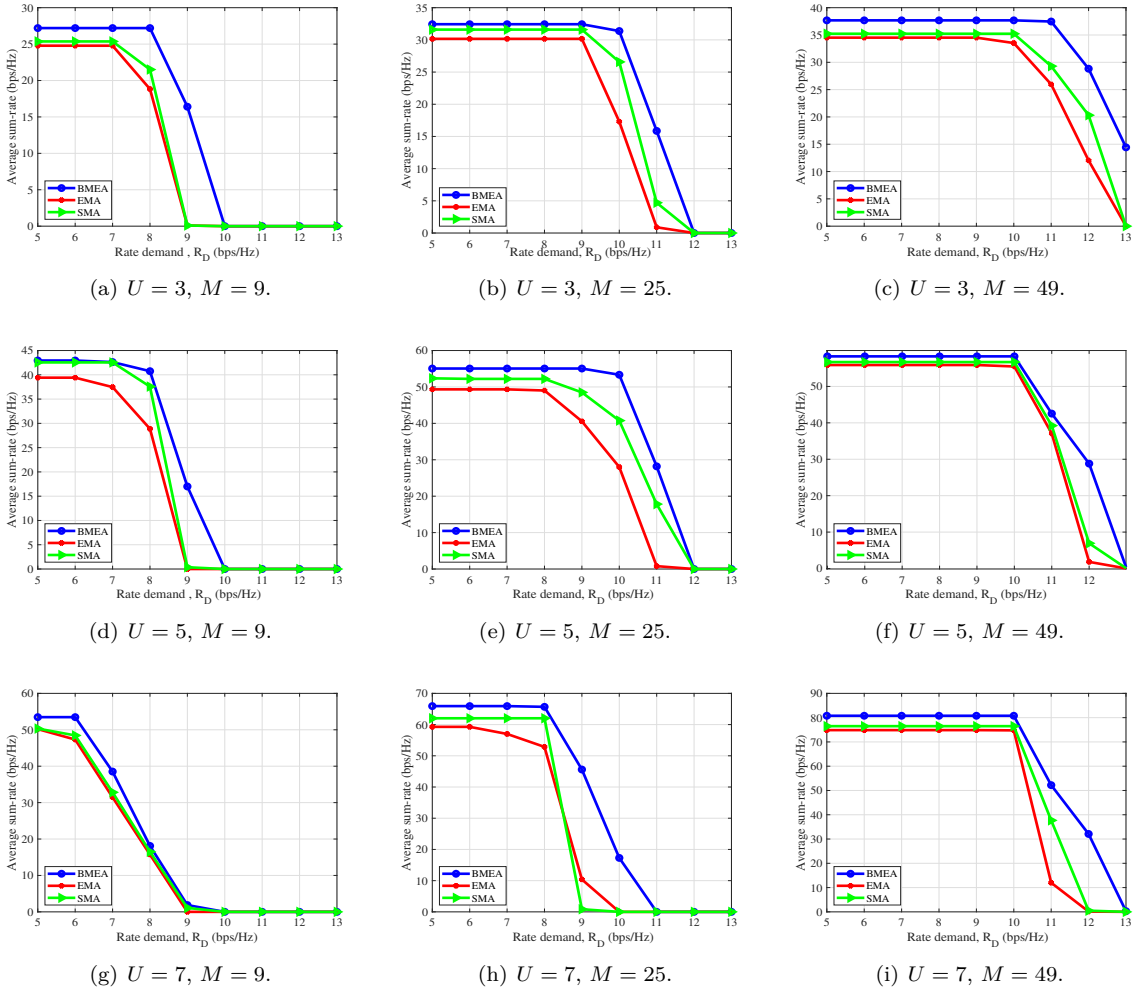

(a) $U = 3$, $M = 9$. (b) $U = 3$, $M = 25$. (c) $U = 3$, $M = 49$.

(d) $U = 5$, $M = 9$. (e) $U = 5$, $M = 25$. (f) $U = 5$, $M = 49$.

(g) $U = 7$, $M = 9$. (h) $U = 7$, $M = 25$. (i) $U = 7$, $M = 49$.

Figure 5.9: Average sum rate performance of the proposed BMEA, SMA, and EMA versus rate demand R_D.

5.12.2 Simulation Results

The reported results are an average of 10 experiments lasting 1000 optimization instances. We first evaluate the impact of the required rate demand on the sum rate performance of OIRS-assisted UAV and laser-based indoor communication networks under various schemes. Fig. 5.9 illustrates the average sum rate versus the rate demand R_D, with values of M ($M = 9, 25, 49$) when $U = 3, 5, 7$. It is evident that as R_D increases, the average sum rate decreases for the BMEA, EMA, and SMA schemes. The probability of seeking suitable mirror elements for supporting higher rate demands decreases; consequently, the number of served users decreases. As a result, the overall average sum rate decreases. It is also observed that BMEA, EMA, and SMA provide comparable performance for lower values of R_D. However, the BMEA scheme significantly outperforms SMA and EMA for higher values of R_D. Because the BMEA scheme assigns the most appropriate mirror elements so that the rate demand R_D is satisfied. Generally, as M increases, the achieved sum rate increases due to the availability of more mirror elements. Under low values of M, the sum rate performance concerning R_D degrades for all schemes. The BMEA scheme significantly outperforms the SMA and EMA schemes with respect to the

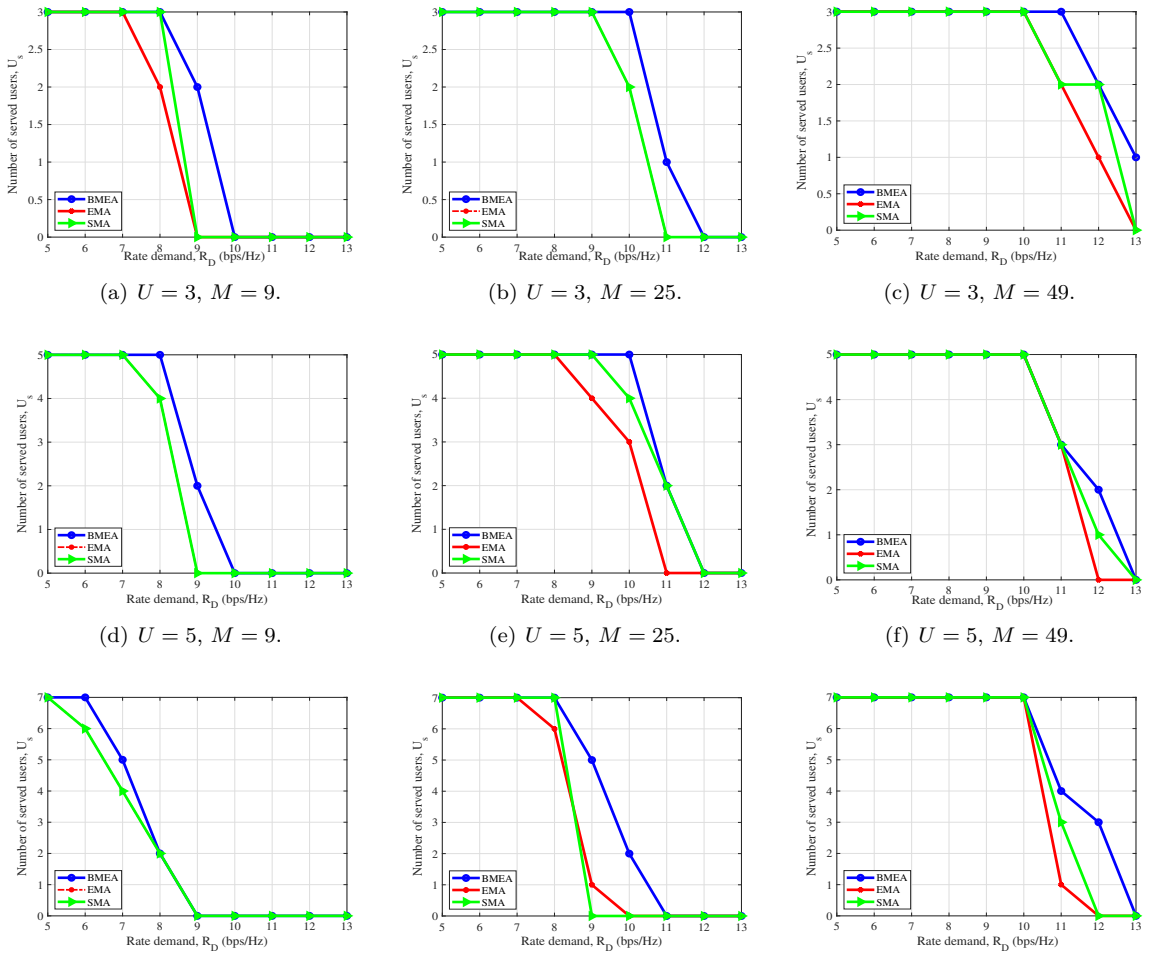

(a) $U = 3$, $M = 9$. (b) $U = 3$, $M = 25$. (c) $U = 3$, $M = 49$.

(d) $U = 5$, $M = 9$. (e) $U = 5$, $M = 25$. (f) $U = 5$, $M = 49$.

(g) $U = 7$, $M = 9$. (h) $U = 7$, $M = 25$. (i) $U = 7$, $M = 49$.

Figure 5.10: Number of served users in case of proposed BMEA, SMA, and EMA versus rate demand R_D.

achievable sum rate for higher values of R_D when M is large. When more mirror elements are available, BMEA can allocate more mirror elements to users according to their R_D. Furthermore, the BMEA scheme allows users to allocate the mirror elements concurrently to satisfy their rate demands. Fig. 5.9 (a)–(i) also indicates that as U increases, the sum rate performance increases for the three schemes, especially for low values of R_D. Under low values of M, none of the schemes significantly improves the average sum rate at high values of R_D. However, when M is increased, BMEA significantly outperforms EMA and SMA for higher values of R_D, regardless of U.

Fig. 5.10 plots the number of served users with respect to R_D under different values of M when $U = 3$, 5, 7. Generally, as R_D increases, the probability of serving more users decreases for all schemes. All schemes provide comparable performance in terms of the number of users served when R_D is low. In contrast, when R_D is high, the BMEA scheme significantly outperforms the other two due to its inherent rate demand awareness. At low values of M, the BMEA scheme achieves a comparable performance for high U. This is because of the limited availability of mirror elements; hence, BMEA tends to utilize only one mirror element per user. When the availability of mirror elements increases, the BMEA scheme satisfies more user rate demands even when U

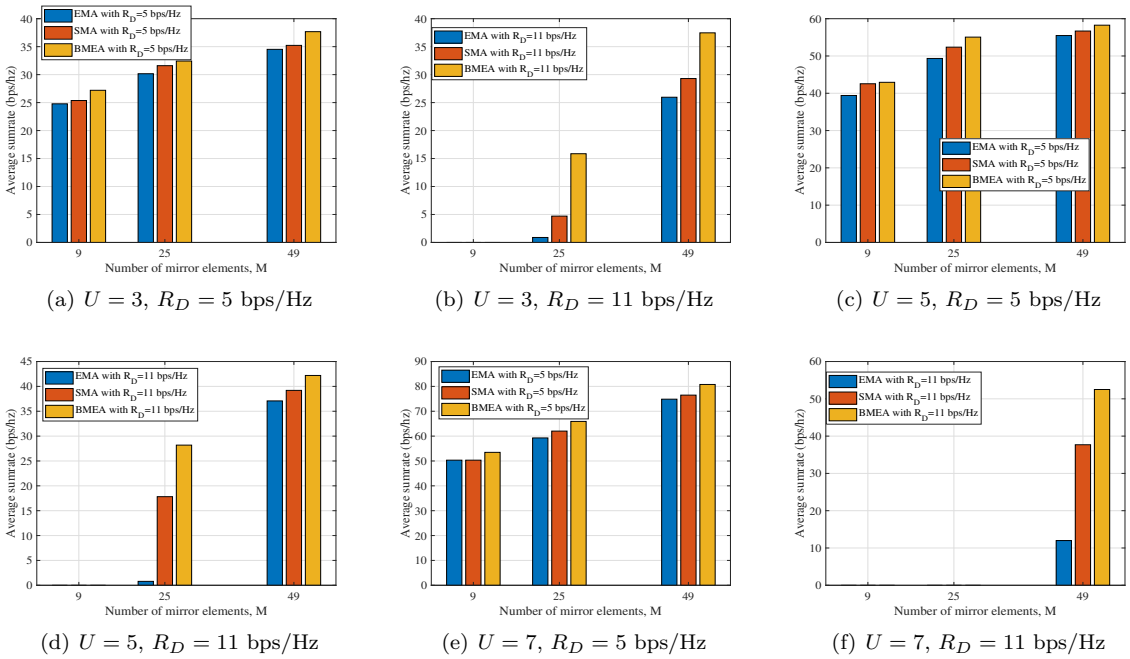

(a) $U = 3$, $R_D = 5$ bps/Hz (b) $U = 3$, $R_D = 11$ bps/Hz (c) $U = 5$, $R_D = 5$ bps/Hz

(d) $U = 5$, $R_D = 11$ bps/Hz (e) $U = 7$, $R_D = 5$ bps/Hz (f) $U = 7$, $R_D = 11$ bps/Hz

Figure 5.11: Average sum rate performance of BMEA, SMA, and EMA versus the number of mirror elements M.

is high. Therefore, the BMEA scheme outperforms the other two schemes when using more mirror elements, regardless of U. Fig. 5.11 illustrates the average sum rate versus the number of mirror elements M for $U = 3$, 5, 7 when $R_D = 5$ and 11 bps/Hz. The BMEA scheme exhibits the highest sum rate performance compared to SMA and EMA. However, the SMA and EMA schemes persistently enhance the sum rate performance when the number of mirror elements M increases. For a lower rate demand R_D, the sum rate performance improves for all three schemes with an increase in the number of mirror elements M. This is because more users can be served when R_D is low. Therefore, the overall performance of the network is improved in terms of the average sum rate. The BMEA scheme outperforms other schemes for low R_D values.It may also be noted that the sum rate performance of the SMA scheme is very close to the EMA scheme under lower values of M. When the number of mirror elements is low, i.e., $M = 9$, the sum rate performance of BMEA for $R_D = 5$ bps/Hz is much greater than that for $R_D = 11$ bps/Hz. This is because each user requires more mirror elements; therefore, the chances of achieving $R_D = 11$ bps/Hz using fewer mirror elements are small. It is noted that SMA and EMA do not significantly improve the average sum rate even with high values of M, especially for high demand rates (i.e., $R_D = 11$ bps / Hz). However, the BMEA scheme provides significant performance gains in the average sum rate when $M = 49$, even in case of a higher rate demand $R_D = 11$ bps/Hz utilizing greater availability of elements.

In Fig. 5.12, we evaluate the fairness performance of the proposed BMEA, SMA, and EMA schemes with respect to the number of mirror elements M for the different numbers of users U and a rate demand of $R_D = 8$ bps/Hz. It is observed that the BMEA scheme outperforms SMA and EMA schemes in terms of fairness. It is revealed that the BMEA and SMA schemes can achieve high fairness performance for the greater value of M

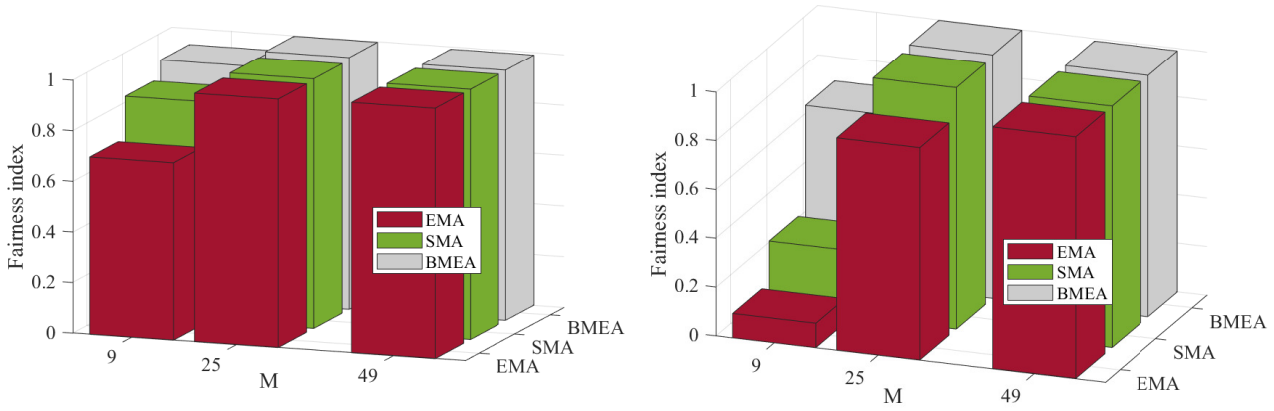

(a) $U = 5$ (b) $U = 7$

Figure 5.12: Fairness index performance of BMEA, SMA, and EMA versus number of mirror elements M for rate demand $R_D = 8$ bps/Hz.

(that is $M = 49$), regardless of U. However, it is observed that in the case of the BMEA scheme, an almost uniform rate is obtained compared to the SMA and EMA schemes, even in the case of a small number of mirror elements M (that is, 9) and a large number of users (i.e., $U = 7$). It is also observed that the BMEA scheme can achieve a uniform rate compared to other schemes. This is because the BMEA scheme adopts a fair user selection and allocation strategy of mirror elements of OIRS. Hence, using the BMEA scheme, more than 0.9 fairness index is attained under different values of M and U. Depending on the rate demand of users, the probability of the number of users served increases with the increase in U for all schemes. Consequently, it produces a higher sum rate and fairness with respect to the increase in U. Furthermore, for the computation of the sum rate and fairness, we considered the rates of the users served whose rate demands are satisfied. It is also observed that the proposed BMEA scheme always allocates the best available M mirror elements to each served user to satisfy their rate demands. Therefore, it is evident that the proposed BMEA scheme remarkably outperforms the other two schemes. As the number of mirror elements M increases, the sum rate achieved increases because a larger number of mirror elements M is available for assignment to serve more competing users U.

5.13 Optimizing Indoor OIRS-Assisted UAV FSO Networks: Key Findings and Insights

In part II of this chapter, we investigated the problem of joint user selection and mirror-element assignment in a downlink OIRS-assisted UAV and laser-based indoor communication networks. We developed an optimization framework that ensures that the maximum number of users is served while satisfying the rate demand and the mirror element constraints. The proposed BMEA scheme employs a batch-based user-selection and mirror-element assignment that allows simultaneous multi-mirror element allocation for multiple contending users to maximize the number of served users. Furthermore, we analyzed the BMEA scheme's performance and

compared it with reference heuristic schemes, i.e., SMA and EMA schemes. The proposed BMEA scheme is a sub-optimal and computationally efficient solution. The reported results depicted that the BMEA scheme significantly outperforms the SMA and EMA schemes in terms of the number of served users, average sum rate, and fairness. Furthermore, the BMEA scheme provides remarkable performance enhancement in the achieved average sum rate while maintaining fairness, especially for a higher number of users and a higher number of mirror elements.

5.14 A Use case: Smart Connectivity Solutions for Indoor Events

A large indoor sports arena hosts a real-time AR/VR-enhanced live event. Thousands of users are connected to immersive content through wearable devices, demanding extremely high data rates and low latency. The arena's ceiling and walls are equipped with laser-based OWC transmitters. A UAV equipped with an OIRS hovers overhead to ensure optimal light beam redirection toward user clusters in the crowd. The BMEA scheme can be deployed to manage user selection and mirror element allocation for dynamic clusters of users, like a group of users in a certain section or media personnel streaming live content.

5.15 Chapter Summary

This chapter presents key insights into the efficient allocation of mirror elements in UAV and OIRS-assisted OWC architectures. In Part I, we examine the performance of a downlink OIRS-aided UAV-based FSO network under various FSO channel impairments. The mirror element assignment problem within this architecture is investigated. To address this, we formulate an optimization problem that aims to maximize the average user data rate while meeting essential design constraints. To achieve high performance and fairness across users, we propose the SMA scheme, which optimally allocates mirror elements. We benchmark the SMA scheme against both heuristic and conventional approaches, with simulation results showing that SMA significantly improves throughput and ensures a fairer distribution of data rates.

Part II shifts focus to the challenges of maintaining reliable OWC in indoor environments, especially in the presence of obstructed LoS conditions. Here, we develop an optimization framework designed to serve the maximum number of users while satisfying rate and mirror element constraints. To this end, we introduce a BMEA, which enables the simultaneous allocation of multiple mirror elements to contending users. This strategy maximizes user coverage in indoor scenarios. Performance evaluations reveal that the BMEA scheme outperforms reference schemes, including SMA and the EMA scheme, in terms of the number of users served, average sum rate, and overall fairness.

Chapter 6

Optimal Resource Allocation in FSO-based Communication Networks under Jamming Attacks

In the previous chapter, the performance of an OIRS-assisted UAV-based FSO network was examined, with a focus on optimizing the assignment of mirror elements to maximize the number of users served while meeting QoS constraints. This chapter extends the analysis to the resilience of FSO-based communication networks under jamming attacks.

Part I of this chapter addresses the mirror-element allocation problem in OIRS and UAV-assisted FSO networks facing proactive jamming, with the goal of enhancing network resilience and reliability amid adversarial interference. Additionally, we compare the performance of the jamming-aware mirror allocation scheme with other reference models. Part II generalizes the scenario to address reactive jamming attacks. Here, we analyze and benchmark the performance of a reactive jamming-aware mirror element allocation scheme against other existing approaches.

6.1 Securing OIRS and UAV-assisted FSO networks under Proactive Jamming

In many realistic applications, delivering messages between communicating devices on time is always required. These applications are often associated with critical human tasks such as health care, road safety, and defense, where a high level of security is crucial. Unfortunately, due to the specific characteristics of the FSO-based network, achieving security is more complex than in traditional networks. The inherent technical limiting fac-

The work in this chapter resulted in the following publication:

1. P. Singh, H. B. Salameh, V. A. Bohara, A. Srivastava and M. Ayyash, “Jamming-Resilient Mirror Element Allocation Scheme for OIRS-aided UAV-based FSO Networks," in *IEEE Transactions on Intelligent Vehicles*,2024, doi: 10.1109/TIV.2024.3450191.

2. P. Singh, H. B. Salameh, V. A. Bohara, A. Srivastava and M. Ayyash, "On Mitigating Reactive Jamming with Dynamic Resource Allocation in OIRS and UAV-assisted FSO-based Networks" in *Physical Communication*, 2024, 102520, ISSN 1874-4907, doi: 10.1016/j.phycom.2024.102520.

tors of FSO-based networks can lead to signal jamming, which can severely affect reliable data transmission. Jamming in FSO-based networks is the most challenging threat, for which limited research has been conducted so far. It is widely known that FSO-based communication links are not easy to disrupt, resulting in a minimal investigation of jamming in FSO-based networks [64]. The jammer intentionally transmits the optical signals to jam the legitimate transmission between the communicating devices. In FSO-based networks, malicious optical transmitters, such as jammers, deliberately use the optical signal to disrupt the communication between the legitimate transmitter and the receiver, which can result in higher-layer security problems, such as DoS. Jamming is an intentional disturbance that differs significantly from interference or an unintentional disruption [19, 20]. Therefore, a jamming attack is a potential threat that a jammer can easily implement to disrupt performance in FSO-based networks. Compared to jamming attacks in FSO-based networks, jamming attacks in RF have been widely studied and explored in [60, 61]. RF jamming is a frequency-dependent phenomenon in which jammers utilize an RF transmitter to transmit jamming signals tuned to the operating frequency. Jamming attacks in FSO-based networks can be caused by either proactive or reactive jammers. Proactive jammers indiscriminately transmit interference without needing prior knowledge of the network infrastructure or user traffic. In contrast, reactive jammers monitor the network and initiate jamming only upon detecting activity on a communication channel. Reactive jamming is an energy-efficient technique as it optimally utilizes its transmit power to disrupt legitimate transmissions. Part I of this Chapter considers the most common type of security attack, i.e., proactive jamming attacks, where jammers are not required to have any prior knowledge about the legitimate transmissions. Jamming attacks are detected by evaluating performance metrics such as the packet loss ratio (PLR), the received optical signal strength, and the signal-to-jamming noise ratio (SJR). In [67], the authors analyzed the performance of a SISO FSO-based network in the presence of a jammer. A MISO FSO-based network is proposed to mitigate the impact of jamming attacks. The performance of the MISO and SISO FSO-based network is evaluated in terms of BER. In [68], the authors proposed a threshold-based detection mechanism to detect legitimate transmission in the presence of a jammer. An MISO FSO-based network is utilized to mitigate the impact of a jamming attack. Performance comparison of MISO and SISO FSO-based networks in the presence of a jammer is studied in terms of BER, outage probability, and diversity order. The jamming attack is investigated under the effect of FSO channel impairments such as atmospheric turbulence and pointing errors over Gamma-Gamma fading channels, along with the pointing error. In [20], the authors developed a non-cooperative game where two players, the jammer and legitimate users, interact competitively to maximize secrecy capacity and minimize energy consumption. In this non-cooperative game model, energy-efficient attack and defense are considered utility functions for both players, the jammer and the legitimate user. In [69], the authors proposed using a buffer at the relay node to combat the effects of jamming attacks in FSO-based networks. The authors compared the performance of buffer-aided and non-buffer-aided in terms of BER and outage probability. In [70], the authors analyzed the effect of jamming on the UAV-assisted FSO link. The authors employ threshold-based detection to detect jamming activity in legitimate transmission. The BER expression for UAV-assisted FSO-based networks in the presence of a random jammer is analytically derived and analyzed. The performance of the UAV-assisted FSO-based network is examined under the com-

bined effect of jamming activity, pointing error, and atmospheric turbulence. In [71], the authors compared a sub-optimal and an approximate threshold-based detector to detect jamming activity in the relay-assisted FSO-based network. Both a suboptimal and an approximated threshold-based detector are derived from a maximum likelihood detector. Moreover, the authors analytically derived and analyzed the BER and diversity gain expressions for a relay-based FSO-based network with an arbitrary number of relays in the presence of a random jammer. In the aforementioned research work, the jammer is considered a stationary entity. However, in [72], the authors considered mobile UAV as a jammer in IRS-assisted UAV and FSO-based networks. In addition, the authors compared two types of scenarios. In one scenario, the UAV acts as a jammer, corrupting the received signal at the UAV as a relay from the source. On the other hand, in the second scenario, the UAV, as a jammer, jams the received signal at the destination. Furthermore, in the presence of a random jammer, analytical expressions for the BER and the outage probability for both scenarios have been derived. To mitigate the jamming effect, an IRS is utilized, and the performance of the proposed system in the presence and absence of IRS is also demonstrated for different scenarios. In [13], the authors introduced a new scheme to allocate mirror elements optimally in indoor optical wireless communication networks. However, in this mirror element assignment scheme, only indoor optical channel conditions are considered to guarantee demand rates to the users under a non-jamming environment. The authors evaluate the effectiveness of the scheme by measuring performance metrics such as fairness index, sum rate, and number of served users.

6.2 Motivation and Contribution

6.2.1 Motivation

It is well known that FSO channel impairments and their aforementioned limiting factors make FSO-based networks prone to intrusion by adversaries. In the presence of an adversary/intruder, FSO technology may not be able to support the key requirements of future communication networks. To the best of our knowledge, the preliminary investigation of the optimal mirror element allocation scheme without accounting for jamming attacks was first conducted in an OIRS-assisted UAV-based indoor optical network in [13]. However, in the proposed work, we demonstrate a novel mirror element allocation scheme that mitigates jamming attacks in an OIRS-assisted UAV-based outdoor optical network. This novel mirror element allocation scheme considers the FSO channel's characteristics and users' demand rate requirements while being jamming aware. The main aim of the proposed scheme is to maximize the number of users served while satisfying the design constraint requirements, such as rate demand and unsuccessful transmission constraints, by performing simultaneous jamming-aware mirror element allocation decisions. Furthermore, in this chapter, we propose a novel jamming Aware-Mirror element Allocation (JA-MEA) scheme to satisfy the user's rate demand requirement while considering the security requirements of FSO-based networks.

6.2.2 Contribution

The major contributions of the proposed work in this chapter are outlined as follows:

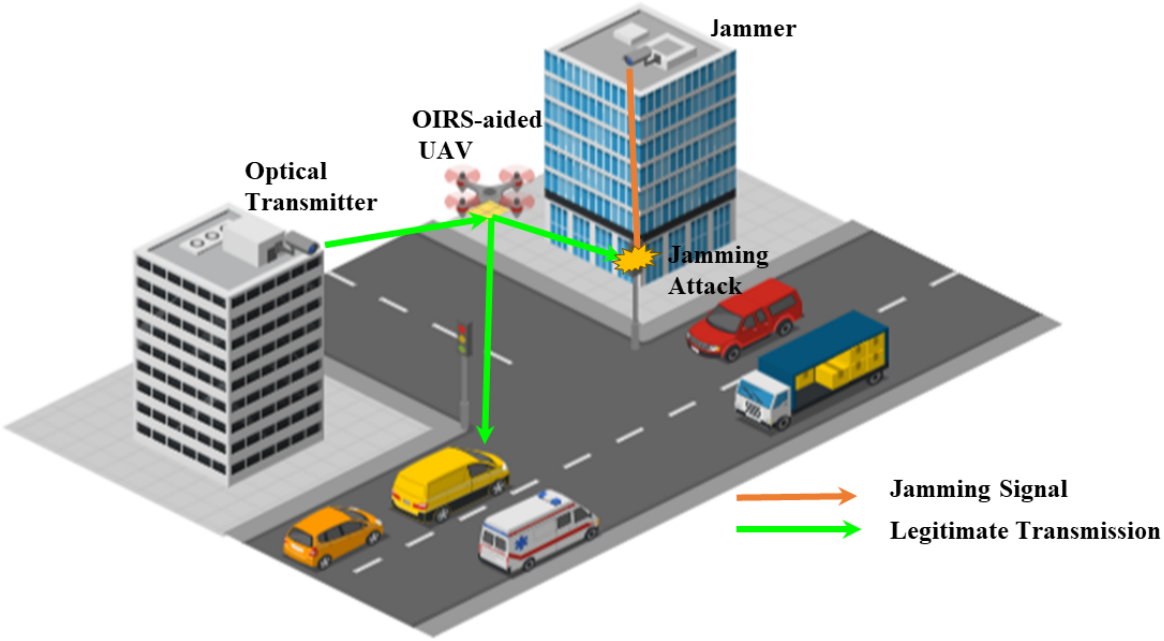

Figure 6.1: System model

1. Formulation of batch-based multi mirror-element allocation problem that considers FSO channel conditions and rate demand of the user while being aware of proactive jamming attacks. The derived problem turns out to be a non-linear binary linear programming problem (NLBP).

2. By mathematical manipulation, the NLBP is linearized into a BLP. Also, we propose and utilize the JA-MEA scheme based on a polynomial-time sequential-fixing linear programming (SFLP) procedure to iteratively assign suitable mirror elements to the legitimate users simultaneously while being 'jamming aware'.

3. We execute rigorous simulations to evaluate the proposed JA-MEA scheme under various conditions such as rate demand, sum rate, blocking probability, and jamming severity.

4. Further, we compare the performance of the JA-MEA scheme with respect to benchmark schemes such as jamming Aware-Equal Mirror element Allocation (JA-EMA), jamming Unaware-Mirror element Allocation (JU-MEA) [13], and jamming Unaware-Equal Mirror element Allocation (JU-EMA) [13] schemes.

6.3 System Model

We consider an OIRS-assisted UAV-based FSO network operating in a proactive jammed environment in which an optical transmitter transmits the information to legitimate users (vehicle and roadside units) at road intersections using an OIRS-assisted UAV (see Fig. 6.1). To meet QoS requirements in vehicular communication

networks, we employ FSO communication for infrastructure-to-vehicle transmissions, enabling the efficient delivery of emergency messages to vehicles at intersections. We assume that an optical transmitter transmits emergency or safety-critical messages to users via an OIRS-assisted UAV and assume that each user is equipped with an optical transceiver. A proactive jammer obstructs legitimate transmissions between the optical transmitter and users by directly jamming the receiver aperture. The proactive jamming model is mathematically presented using a predefined strategy $G(T_{Jam})$, where T_{Jam} denotes the jamming interval [136]. The jamming interval T_{Jam} is the period between the two consecutive jamming signals [136]. Further, we assume that an OIRS-assisted UAV provides coverage to legitimate users and resolves the network's non-LoS problem in FSO-based networks. We consider the optical transmitter in the network to be equipped with a laser source to transmit information to the OIRS-assisted UAV through an FSO link. The mirror-based OIRS is deployed on the UAV so that the optical beam is beamformed and reflected in the desired user direction as in [17, 53]. The divergence angle of the transmitted optical beam from the laser source is chosen and focused so that the Gaussian beam's footprint covers the entire surface of the OIRS. We assume an OIRS and UAV-assisted FSO networks, serving a set of $\mathcal{U}$ users, where $U = |\mathcal{U}|$ denotes the number of user receivers distributed in an outdoor scenario under a proactive jammed environment, in which the attackers transmit jamming packets to corrupt the ongoing legitimate transmissions based on a predefined strategy. Consider $\mathcal{M}$ as the set comprising M mirror elements, where $M = |\mathcal{M}|$ represents the total count of mirror elements in OIRS. The position of the OIRS-assisted UAV, optical transmitter, each mirror element, and the user are expressed in terms of 3D coordinates $(x,\ y,\ z)$. As per the location information of the UAV, the optical beam is directed toward the OIRS-assisted UAV. Moreover, in this chapter, we assume that an OIRS-assisted UAV controller regulates the movement and orientation of each mirror element. Furthermore, we assume that the FSO-based communication link between the optical transmitter and OIRS-assisted UAV, and OIRS-assisted UAV and each user experience atmospheric turbulence with atmospheric attenuation, misalignment error due to hovering OIRS-assisted UAV, AoA fluctuations [46].

In this chapter, we explore the application of OIRS in FSO-based networks, which is explained in Chapters 2 and 5. The optical transmitter transmits legitimate information to an OIRS-assisted UAV through an FSO link, and further transmitted information is reflected from an OIRS-assisted UAV to users through the FSO link. The FSO communication channel between the optical transmitter and the user's receiver is considered a fading channel under the effect of atmospheric attenuation, atmospheric turbulence, and the pointing error due to beam misalignment (h_{pe}), and FSO link interruption due to AoA fluctuations (h_{AoA}). The atmospheric turbulence (h_{at}) follows the Gamma-Gamma distribution model, and its PDF is defined as in [137]. Attenuation h_a over the FSO link is estimated according to the Beer-Lambert law as given in [46, 137]. Due to the misalignment of the beam between the fixed optical transmitter and the hovering OIRS-assisted UAV, the pointing error (h_{pe}) arises and is computed as given in [137]. The AoA fluctuations are also considered due to the hovering of OIRS-assisted UAVs, which degrade the network's performance. The AoA fluctuation h_{AoA} is modeled as in [111]. Thus, for legitimate information transmission, the OIRS-assisted UAV-based FSO channel is modeled as the product of all the aforementioned impairments and is represented as $h_F = h_{at}h_a h_{pe}h_{AoA}$. Thus, the

achieved SNR of a user is computed as follows:

$$\gamma_j = \frac{\left[\Re_j \mathcal{P}_j(x,y) a_j h_F\right]^2}{n\mathcal{B}}. \tag{6.1}$$

Therefore, the achievable transmission rate (in bits/s/Hz) of the jth user can be computed as [130]:

$$R_j = \frac{1}{2}\log_2(1+\gamma_j). \tag{6.2}$$

6.3.1 Probabilistic Modeling of Jamming Attack

The probability of packet failure due to a jamming attack is considered an important metric in evaluating any communication system. To derive an expression for the failure probability of packet transmission P_f under a proactive jamming attack, we note that when a packet is transmitted during a jamming attack, the transmission will be successful if three independent events occur jointly:

- In the presence of jamming, transmission will be successful if there is no user present in the coverage area of the beam footprint of the jammer in a given $A_j = \pi\omega_{L_F}^2$ beam area. The total number of users in the beam footprint area of the jammer beam area is modeled as a Poisson distributed random variable with mean $A_j\rho$, where ρ is the spatial density.
- Jamming interval between two consecutive jamming signals T_{Jam} is longer than the needed packet transmission duration t_x.
- Transmission survives when the direction of the transmission of the jammer is not in the direction of the user (a miss event occurs) in the given region. The direction of the jamming attack is uniformly impacting different sub-regions in a given area, that is, $\Pr\{u_r\} = 1/U$ for $1 \le u_r \le U$.

A closed-form expression for the probability of successful transmission for a given user density ρ in the presence of a jammer can be derived as follows:

$$\begin{aligned} P_s &= (\Pr(\text{No user under } A_j)) \times \Pr\left(\{T_{Jam} \ge t_x\}\right) \times (1 - \Pr(u_r)), \\ &= [1 - (1 - \exp^{-A_j\rho})] \times (\exp^{-\frac{t_x}{T_{Jam}}}) \times (1 - \Pr(u_r)), \\ &= \exp^{-(\frac{A_j\rho T_{Jam} + t_x}{T_{Jam}})} \times (1 - (1/U)). \end{aligned} \tag{6.3}$$

Accordingly, the expression for the failure probability after N_r re-transmission attempts is computed as,

$$P_f = (1 - P_s)^{N_r} = ((1 - \exp^{-(\frac{A_j\rho T_{Jam} + t_x}{T_{Jam}})}) \times (1/U))^{N_r}. \tag{6.4}$$

Under proactive jamming, we consider that failure probability after N_r re-transmission attempts should be less than a certain threshold Λ as given in [136]. Hence,

$$P_f \le \sqrt[N_r]{\Lambda}. \tag{6.5}$$

After some algebraic manipulation, the failure probability constraint for a given mirror element allocation can be written in terms of the jamming and transmission parameters as follows:

$$(1 - \exp^{-(\frac{A_j\rho T_{Jam} + t_x}{T_{Jam}})}) \le (U\sqrt[N_r]{\Lambda}),\ \ln\left(1 - (U\sqrt[N_r]{\Lambda})\right) T_{Jam} + A_j\rho T_{Jam} \le -t_x.$$

6.4 Problem Statement and Formulation

6.4.1 Problem Statement

Our problem statement can be defined as follows: given the set of mirror elements $\mathcal{M}$ with an optimal deflection angle $\theta_j^{(i)*}$, the legitimate users $\mathcal{U}$ with rate demand R_j^D, our objective is to find the jamming-resilient mirror-element allocation to maximize the number of simultaneously serving users subject to the following design constraints:

C.1.) **Rate demand**: This constraint allows each jth user to select more than one mirror element so that the required rate demand R_j^D is guaranteed.

C.2.) **Failure probability constraint**: This constraint ensures that the failure probability P_f of a link should be less than a predefined threshold value Λ.

C.3.) **Mirror element constraint**: This constraint permits that each mirror element is allocated to only one user.

C.4.) **Resource constraint**: This limitation allows each user to be allocated a maximum κ number of mirror elements.

6.4.2 Problem Formulation

Our objective is to maximize the number of served users under proactive jamming, which is mathematically formulated as:

$$\sum_{j\in\mathcal{U}} \mathbf{1}\left[\sum_{i=1}^{M} \chi_j^{(i)} \geq 1\right], \tag{6.6}$$

where $\mathbf{1}[.]$ denotes the indicator function. For the given data transmission, the design constraints can be rewritten in terms of a binary decision variable $\chi_j^{(i)}$ described as follows:

$$\chi_j^{(i)} = \begin{cases} 1, & \text{When a mirror element i is assigned to user j} \\ 0, & \text{or else.} \end{cases} \tag{6.7}$$

Under proactive jamming, the failure probability constraint in (6.6) can be rewritten in terms of the binary decision variable $\chi_j^{(i)}$ as follows

$$\ln\left(1-(U\sqrt[N_r]{\Lambda})\right)T_{Jam} + A_j\rho T_{Jam} \leq -\sum_{i\in\mathcal{M}} t_x\chi_j^{(i)}, \tag{6.8}$$

where $t_x = \frac{L}{\sum_{i\in\mathcal{M}} R_j^{(i,\theta_j^{(i)*})}\chi_j^{(i)}}$, L is data packet length and $R_j^{(i,\theta_j^{(i)*})}$ denote rate of jth user.

After some algebraic manipulation, (6.8) can be rewritten in a linear form as:

$$\sum_{i\in\mathcal{M}} \left(R_j^{(i,\theta_j^{(i)*})}\left(\ln\left(1-(U\sqrt[N_r]{\Lambda})\right)T_{Jam} + A_j\rho T_{Jam} + L\right)\chi_j^{(i)} \leq 0. \tag{6.9}$$

Let $(R_j^{(i,\theta_j^{(i)*})}(\ln\left(1-(U\sqrt[N_r]{\Lambda})\right)T_{Jam}+A_j\rho T_{Jam}+L) = \mathcal{A}_j^{(i)}$, then it can be re-written in given form $\sum_{i\in\mathcal{M}}\mathcal{A}_j^{(i)}\chi_j^{(i)} \leq 0$. Given the main objective function in (6.21) with design constraints in (C1–C4), our problem can be formu-

lated as follows:

$$\begin{aligned}
\mathbf{P1}: &\max_{\chi_j^{(i)}} \sum_{j\in\mathcal{U}} \mathbf{1}\left[\sum_{i=1}^{M} \chi_j^{(i)} \geq 1\right] \\
s.t.\ &\sum_{i\in\mathcal{M}} R_j^{(i,\theta_j^{(i)*})} \chi_j^{(i)} \geq R_j^D \text{ or } 0,\ \forall j \in \mathcal{U} \\
&\sum_{i\in\mathcal{M}} \mathcal{A}_j^{(i)} \chi_j^{(i)} \leq 0,\ \forall j \in \mathcal{U} \\
&\sum_{j\in\mathcal{U}} \chi_j^{(i)} \leq 1,\ \forall i \in \mathcal{M} \\
&\sum_{i\in\mathcal{M}} \chi_j^{(i)} \leq \kappa,\ \forall j \in \mathcal{U} \\
&-\pi/2 < \theta_j^{(i)} < +\pi/2\ \forall i \in \mathcal{M}. \\
&\chi_j^{(i)} \in \{0,1\},\ \forall i \in \mathcal{M},\ \forall j \in \mathcal{U}
\end{aligned} \tag{6.10}$$

To optimize the indicator function, it is essential to introduce a new binary variable ν_j and linearize the objective function. This can be achieved by incorporating two more linear constraints as follows:

$$\nu_j = \mathbf{1}\left[\sum_{i=1}^{M} \chi_j^{(i)} \geq 1\right],\ \forall j \in \mathcal{U}, \tag{6.11}$$

$$\begin{aligned}
\frac{\sum_{i\in\mathcal{M}} \chi_j^{(i)}}{|\mathcal{M}|} - \nu_j \leq 0,\ \forall j \in \mathcal{U}, \\
\nu_j - \sum_{i\in\mathcal{M}} \chi_j^{(i)} \leq 0,\ \forall j \in \mathcal{U}.
\end{aligned} \tag{6.12}$$

It is also observed that the jth user is served if any of the $\chi_j^{(i)}$ is unity. Otherwise, if all $\chi_j^{(i)}$'s of the jth user are not unity, then no suitable mirror element allocation for the jth user is found. Consequently, the jth user is not served. Besides this, if there is more than one feasible solution with the same maximum number of served users, then we break the tie by selecting the solution that achieves the highest rate. Therefore, to achieve this, the term $[\frac{\sum_{j\in\mathcal{U}}\sum_{i\in\mathcal{M}} \chi_j^{(i)} R_j^{(i,\theta_j^{(i)*})}}{\mathbb{R}}] < 1$ is added to the objective function, where $\mathbb{R} = \sum_{j\in\mathcal{U}}\sum_{i\in\mathcal{M}} R_j^{(i,\theta_j^{(i)*})}$. To linearize the either/or constraint, we introduce two additional auxiliary binary variables, $y_1^{(j)}$ and $y_2^{(j)}$, and replace the either/or constraint in equation (6.29) with the below given linear constraints:

$$\begin{aligned}
&\sum_{i\in\mathcal{M}} -R_j^{(i,\theta_j^{(i)*})} \chi_j^{(i)} \leq -R_j^D + \Xi y_1^{(j)}, \forall j \in \mathcal{U} \\
&\sum_{i\in\mathcal{M}} R_j^{(i,\theta_j^{(i)*})} \chi_j^{(i)} \leq 0 + \Xi y_2^{(j)}, \forall j \in \mathcal{U} \\
&y_1^{(j)} + y_2^{(j)} = 1, \forall j \in \mathcal{U},
\end{aligned} \tag{6.13}$$

where $\Xi \gg 1$. Using (6.30),(6.31),(6.32), and adding the constraints, the problem in (6.29) is re-formulated as

follows:

$$
\begin{aligned}
\mathbf{P1}: \max_{\chi_j^{(i)},\, \nu_j,\, y_1^{(j)},\, y_2^{(j)}} & \sum_{j\in\mathcal{U}} \nu_j + \frac{\sum_{j\in\mathcal{U}} \sum_{i\in\mathcal{M}} \chi_j^{(i)} R_j^{(i,\theta_j^{(i)*})}}{\mathbb{R}} \\
s.t. \; & \sum_{i\in\mathcal{M}} -R_j^{(i,\theta_j^{(i)*})} \chi_j^{(i)} \leq -R_j^{D} + \Xi y_1^{(j)}, \forall j \in \mathcal{U} \\
& \sum_{i\in\mathcal{M}} R_j^{(i,\theta_j^{(i)*})} \chi_j^{(i)} \leq 0 + \Xi y_2^{(j)}, \forall j \in \mathcal{U} \\
& \sum_{i\in\mathcal{M}} \mathcal{A}_j^{(i)} \chi_j^{(i)} \leq 0, \; \forall j \in \mathcal{U} \\
& \sum_{j\in\mathcal{U}} \chi_j^{(i)} \leq 1, \; \forall i \in \mathcal{M} \\
& \sum_{i\in\mathcal{M}} \chi_j^{(i)} \leq \kappa, \; \forall j \in \mathcal{U} \\
& \frac{\sum_{i\in\mathcal{M}} \chi_j^{(i)}}{|\mathcal{M}|} - \nu_j \leq 0, \; \forall j \in \mathcal{U}, \\
& \nu_j - \sum_{i\in\mathcal{M}} \chi_j^{(i)} \leq 0, \; \forall j \in \mathcal{U} \\
& y_1^{(j)} + y_2^{(j)} = 1, \forall j \in \mathcal{U}
\end{aligned}
\tag{6.14}
$$

6.4.3 The Proposed Solution

An observation of our formulated optimization problem in (6.33) reveals that this formulation is established as a BLP problem, where the optimal solution to such an optimization problem is NP-hard. To find the optimal solution, we can perform an exhaustive search of all possible combinations of mirror elements and user allocations. However, this search for possible combinations grows exponentially with the number of users U and mirror elements M. The computational complexity of an exhaustive search in polynomial time is very high. Thus, we adopt a BSFLP procedure proposed in [131–133] to find a near-optimal polynomial-time solution to the proposed optimization problem given in (6.33). The BSFLP procedure has already been utilized to solve such types of optimization problems in prior research works, and it is shown that suboptimal solutions for BLP problems can be achieved in polynomial time [131–133].

6.5 Performance Evaluation and Discussion

This section investigates the performance of the proposed JA-MEA scheme under proactive jamming attacks in the case of different jamming severity levels. Specifically, the performance of JA-MEA scheme is compared to three different reference schemes: JU-MEA [13], JA-EMA, and JU-EMA schemes [13]. In the JU-MEA scheme, mirror elements are allocated to each user, but this scheme does not account for jamming attacks (i.e., jamming Unaware (JU)). In the JA-EMA and JU-EMA schemes, an equivalent number of mirror elements are assigned to the user account with and without accounting jamming attacks, respectively. The average sum rate and blocking probability are the performance metrics that are computed via Monte Carlo simulations for the

Table 6.1: Simulation parameters for performance evaluation of OIRS-assisted UAV-based FSO network

Parameters	Simulation values
P_T	80 mW
$\Re$	0.5 A/W
A_{PD}	7 mm^2
λ	1550 nm
a	5 cm
$G(\varphi)$	1
$C_n^2(0)$	1×10^{-13} $m^{-2/3}$
σ_j	30 cm
σ_n^2	$10^{-15} A^2/Hz$
L	2 kB

performance evaluation of JA-MEA and other reference schemes.

6.5.1 Simulation Setup

In this chapter, we assume an OIRS-assisted UAV-based FSO network with $M = |\mathcal{M}|$ mirror elements and $U = |\mathcal{U}|$ legitimate users. The optical transmitter in the network has a laser source operating at 1550 nm to generate an optical beam that is directed towards the OIRS surface of the OIRS-assisted UAV. The OIRS-assisted UAV hovers at a vertical height of 50 m in an outdoor region of 100 m $\times$ 100 m, where the U users are uniformly distributed. The distance between the optical transmitter and the OIRS-assisted UAV is assumed to be 200 m, and the optical transmitter is located at a height of 10 m. Furthermore, we consider a mirror-based OIRS with a square geometrical shape, comprising an array of multiple micro-mirror elements. Each element is square-shaped with a side length of 2 mm, and they are positioned 1 mm apart between adjacent mirrors [17]. We set $R_j^D = R_D, \forall j \in U$, the data packet length $L = 2$ kB, the threshold Λ to 0.1, and the number of permitted retransmissions to $N_r = 4$. The simulation parameters used to evaluate the performance are mentioned in TABLE 6.2.

6.5.2 Simulation Results

In this section, we evaluate the sum rate performance of all the schemes with respect to the R_D in an OIRS-assisted UAV-based FSO network under different levels of proactive jamming attacks. Fig. 6.2 illustrates the average sum rate under severe, moderate, and low jamming attacks for different rate demands R_D when $U = 4$ and $M = 16$. It is observed that as R_D increases, the average sum rate decreases for all schemes. This is because the probability of finding suitable mirror elements with higher demand rates decreases when R_D is increased, consequently decreasing the number of served users and reducing the network sum rate. Figs. 6.2 (a)–(c) show that jamming-aware mirror element allocation schemes JA-MEA and JA-EMA significantly outperform jamming-unaware mirror element allocation schemes JU-MEA and JU-EMA, irrespective of different levels of jamming attacks. This is because jamming-aware schemes have inherent jamming awareness to select the most suitable mirror elements for data transmissions. Under severe-to-low jamming attacks, it is noted that our proposed JA-MEA scheme significantly outperforms other schemes for the high value of R_D. In Fig. 6.2

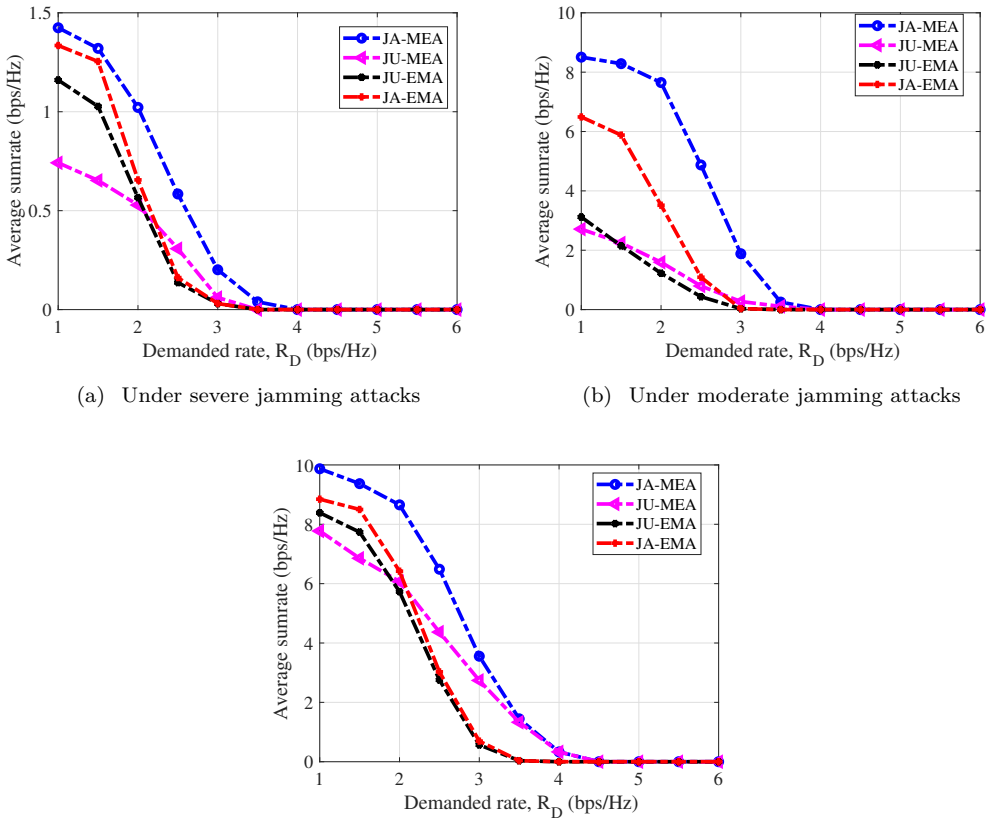

(a) Under severe jamming attacks

(b) Under moderate jamming attacks

(c) Under low jamming attacks

Figure 6.2: Average sum rate performance of JA-MEA, JA-EMA, JU-MEA, and JU-EMA schemes versus rate demand R_D for U= 4, M= 16

(a), under severe jamming attacks, it is observed that our proposed JA-MEA scheme significantly outperforms JA-EMA, JU-MEA and JU-EMA irrespective of R_D.

In Figs. 6.2 (b) and (c), under moderate-to-low jamming attacks, the average sum rate increases for all schemes, especially for the jamming-aware JA-MEA scheme. As the jamming attack becomes less severe, the time period between consecutive jamming signals becomes longer. This reduces the probability that jammers transmit packets; consequently, there is less impact of jamming on the network sum-rate performance. Fig. 6.3 shows the average sum rate as a function of the rate demands R_D under severe, moderate, and low jamming attacks when U =6 and M =36. Figs. 6.3 (a)–(c) also illustrate that as U and M increase, the average sum rate increases for all schemes under different levels of jamming attacks, especially at low values of R_D. This is because, as M increases, the sum rate achieved by users rises as a result of the increased availability of mirror elements. It is also observed that, under severe to low jamming attacks, JA-MEA, JA-EMA, JU-MEA, and JU-EMA offer comparable performance for higher values of R_D. JA-MEA outperforms other schemes in the case of low values of R_D. Figs. 6.4 (a)–(c) plot the blocking probability of users as a function of the rate demand R_D under different levels of jamming attacks for $U = 4$ and $M = 16$. Generally, under severe jamming activities, the chances of serving more users are reduced for all schemes, regardless of R_D. However, due to jamming and

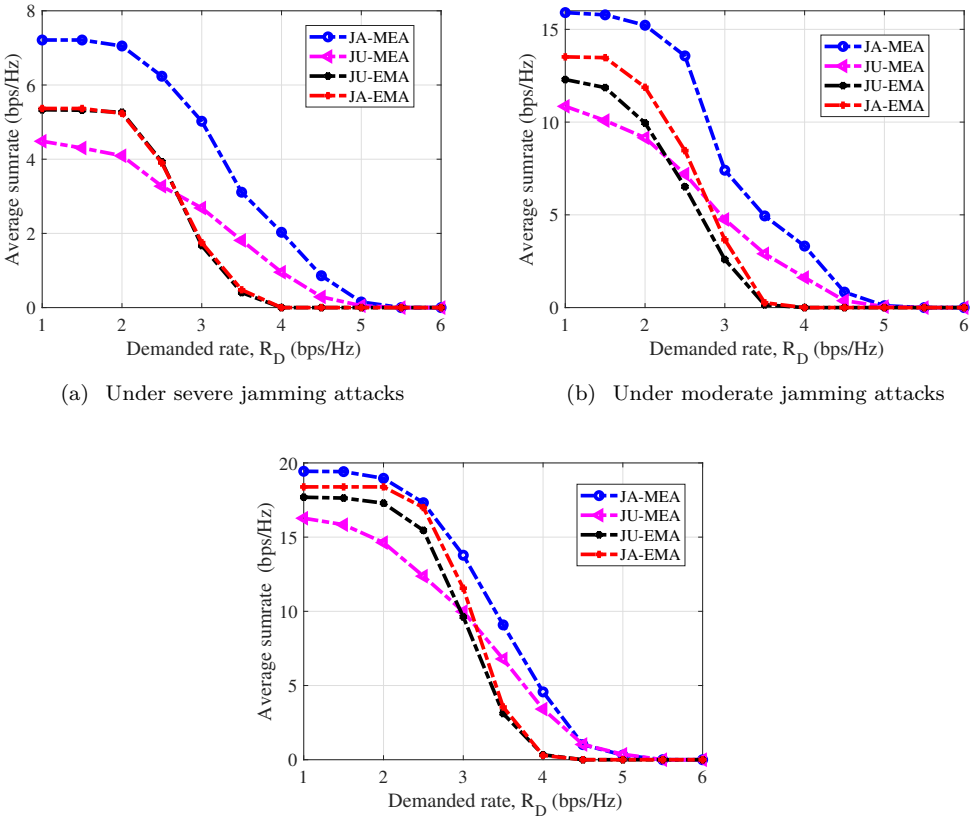

(a) Under severe jamming attacks

(b) Under moderate jamming attacks

(c) Under low jamming attacks

Figure 6.3: Average sum rate performance of JA-MEA, JA-EMA, JU-MEA, and JU-EMA schemes versus rate demand R_D for U= 6, M= 36

the rate demand awareness property, the JA-MEA scheme significantly outperforms the other schemes for low values of R_D and under moderate-to-low jamming attacks. Fig. 6.5 illustrates the blocking probability of users with respect to rate demands R_D under severe, moderate, and low jamming attacks when $U = 6$ and $M = 36$. Figs. 6.5 (a)–(c) indicate that as U and M increase, the probability of blocking decreases for all schemes under different levels of jamming attacks, especially at low values of R_D. When available mirror elements M increase, the JA-MEA scheme achieves significantly higher performance for lower R_D due to the availability of mirror elements, the inherent rate demand, and the awareness property of the jam. Hence, under lower rate demands R_D, the JA-MEA scheme satisfies more user rate demands irrespective of U.

Fig. 6.10 plots the average sum rate as a function of the number of mirror elements M in the case of $U = 4$ when R_D is set to 2.5 and 4.5 bps/Hz. The JA-MEA scheme outperforms the JA-MEA, JU-MEA, and JU-EMA schemes in terms of average sum rate. However, as the number of mirror elements M increases, the sum rate performance of all three schemes improves consistently. Figs. 6.10 (a)-(c) show that the average sum rate of the JA-MEA improves significantly compared to the other schemes in terms of the higher value of M for the lower value of R_D. This is because when R_D is low, more users can be served with proper utilization of mirror elements. Hence, the network's overall performance is enhanced in regard to the average sum rate. It is

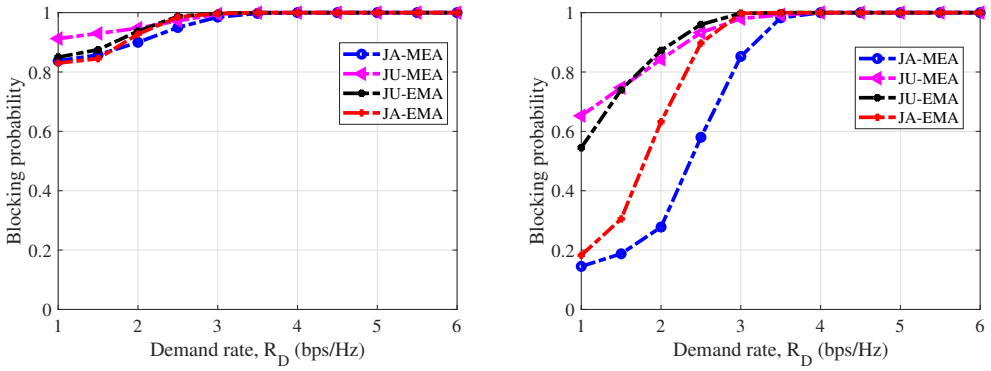

(a) Under severe attacks

(b) Under moderate attacks

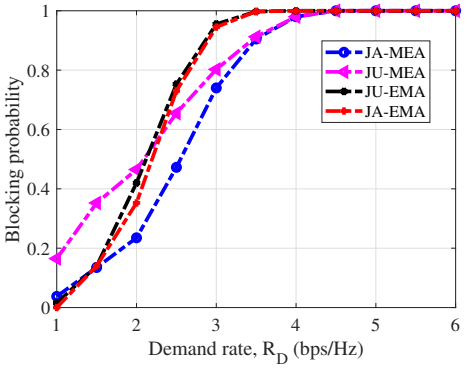

(c) Under low attacks

Figure 6.4: Blocking probability performance of the JA-MEA, JA-EMA, JU-MEA, and JU-EMA schemes versus rate demand R_D for $U=$ 4 and $M=$ 16.

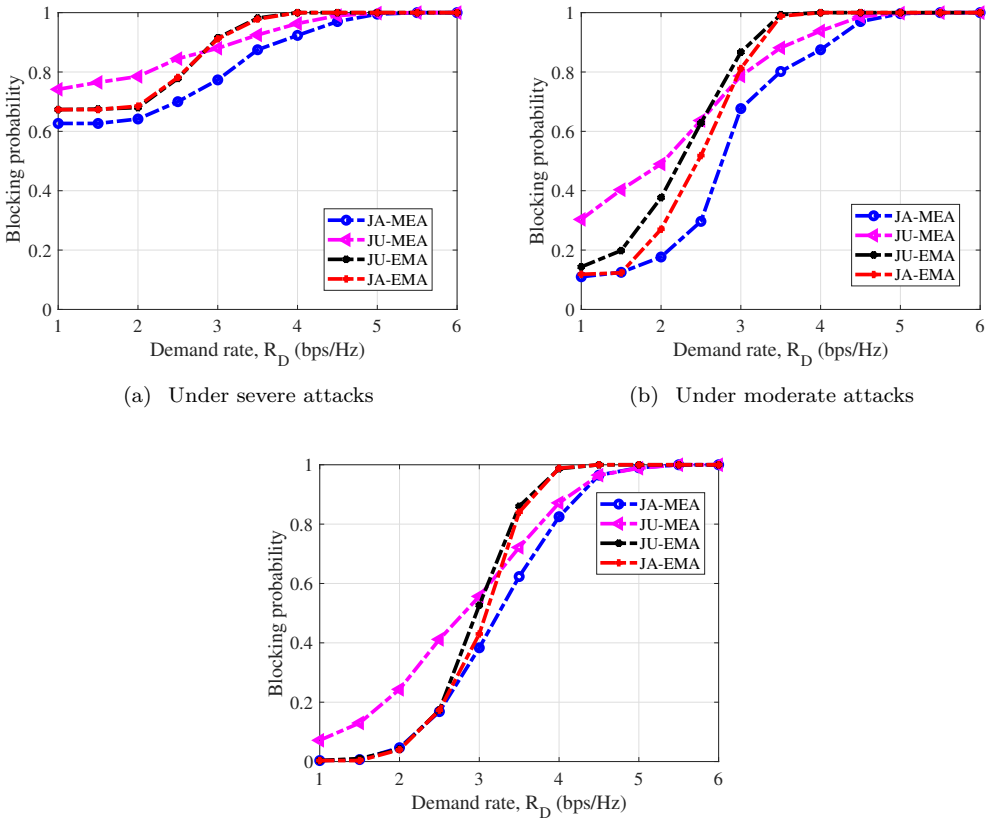

(a) Under severe attacks

(b) Under moderate attacks

(c) Under low attacks

Figure 6.5: Blocking probability performance of the JA-MEA, JA-EMA, JU-MEA, and JU-EMA schemes versus rate demand R_D for U= 6, M= 36

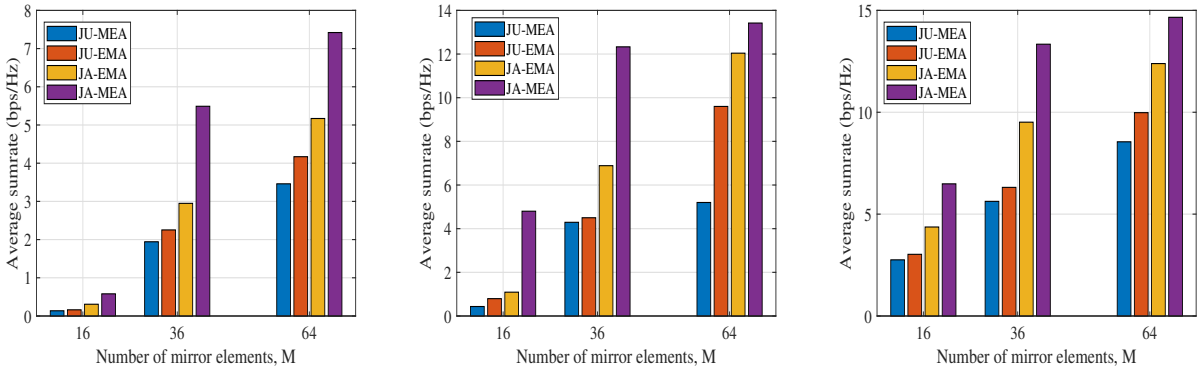

(a) Under severe attacks, when $R_D = 2.5$ bps/Hz (b) Under moderate attacks, when $R_D = 2.5$ bps/Hz (c) Under low attacks, when $R_D = 2.5$ bps/Hz

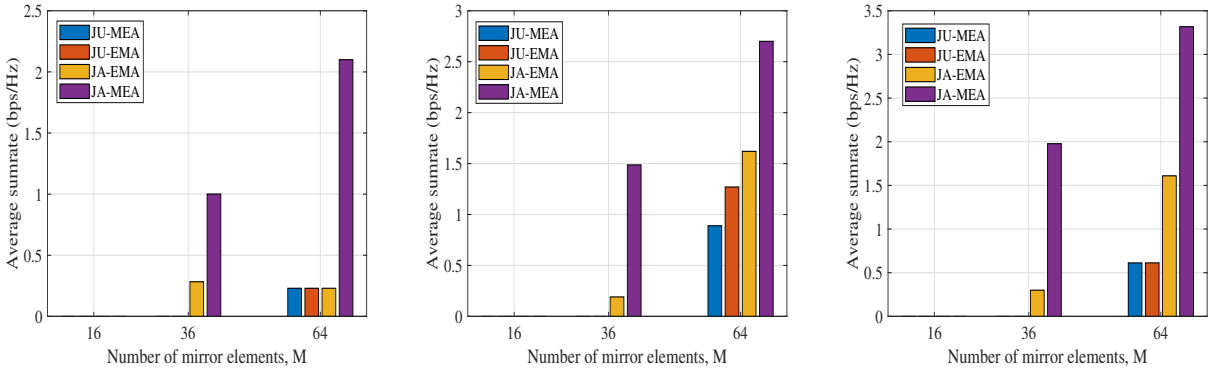

(d) Under severe attacks, when $R_D = 4.5$ bps/Hz (e) Under moderate attacks, when $R_D = 4.5$ bps/Hz (f) Under low attacks, when $R_D = 4.5$ bps/Hz

Figure 6.6: Achieved sum rate of JA-MEA, JA-EMA, JU-MEA, and JU-EMA schemes versus mirror elements M for $U = 4$.

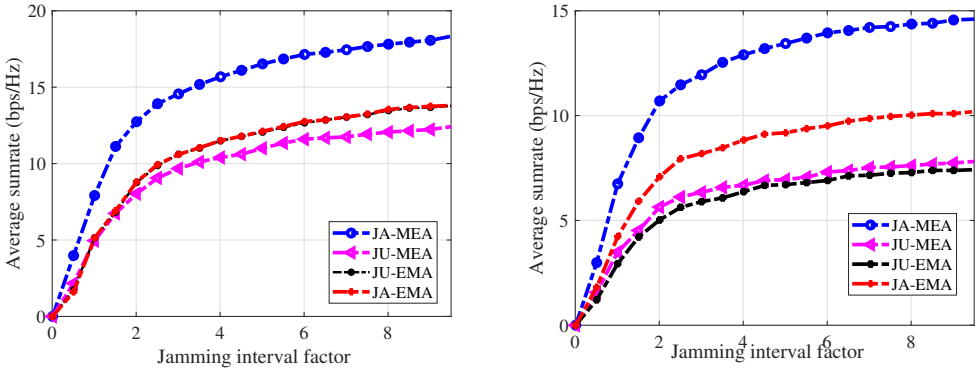

(a) When $R_D = 1$ bps/Hz

(b) When $R_D = 3$ bps/Hz

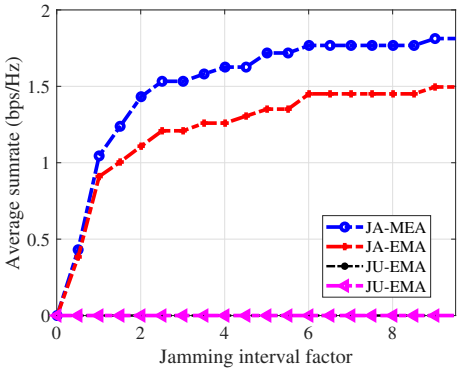

(c) When $R_D = 4.5$ bps/Hz

Figure 6.7: Achieved sum rate of the JA-MEA, JA-EMA, JU-MEA, and JU-EMA schemes versus jamming interval factor in case of U= 6, M= 36

observed that the performance of the sum rate of the JU-EMA and JU-MEA schemes is almost equal to each other at low values of M. It is also noted that with the low value of M, the achieved sum rate of the JA-MEA scheme for $R_D = 2.5$ bps/Hz is higher than for $R_D = 4.5$ bps/Hz. Users need more mirror elements to achieve $R_D = 4.5$ bps/Hz. However, with a lower value of M, achieving $R_D = 4.5$ bps/Hz is less possible. Figs. 6.10 (d)-(f) reveal that JU-MEA and JU-EMA do not enhance the performance of the sum of the rate with a higher value of M, especially under environments of severe jamming attacks for high demand rates. However, under higher rate demand, the JA-MEA scheme provides a significant sum rate improvement over the JA-EMA and other schemes with more mirror elements such as $M = 64$. Figs. 6.11 (a)-(c) illustrate the average sum rate as a function of the jamming interval factor for all schemes when $U = 6$ and $M = 36$. It can be observed that as the jamming interval factor increases, the average sum rate increases across all schemes. It is also noted that the average sum rate for $R_D = 1$ and 3 bps/Hz is higher than that for $R_D = 4.5$ bps/Hz. At the demand rate of 1 bps/Hz and 3 bps/Hz, the chance of finding suitable mirror elements is higher than that of finding mirror elements at the rate of 4.5 bps/Hz, which results in serving more users.

6.6 Optimizing OIRS and UAV-assisted FSO networks Under Proactive Jamming: Key Findings and Insights

In this part of the Chapter, the mirror-element allocation in an OIRS and UAV-assisted FSO networks under a proactive jammed environment is investigated, where the jammers may not have prior knowledge about the legitimate transmissions between the optical transmitter and the legitimate user. We developed an optimization problem that improves the network performance in terms of sum rate and blocking probability while satisfying the user's rate demand and unsuccessful transmission constraints. Under the jamming environment, to satisfy the rate demand of the users, a Jamming-Aware Mirror Element Allocation scheme, i.e., JA-MEA, is suggested, where mirror elements are optimally assigned to the users. In addition, we compared the performance of the JA-MEA scheme with the reference scheme, i.e., the JU-MEA, JU-EMA, and JA-EMA schemes. In both JA-EMA and JU-EMA schemes, an equal number of mirror elements are assigned to the users. JU-MEA and JU-EMA are working as a jamming unaware scheme. However, the JA-EMA scheme is a jamming-aware scheme. The reported results showed that the proposed JA-MEA improves the sum rate and blocking probability performance, especially when more mirror elements are available. The simulation results showed that the JA-MEA scheme has the potential to offer the required rate demand among multiple users in a jamming environment.

6.7 Mitigating Reactive Jamming in FSO-based Networks: Challenges and the Need for Resilient Optimization

Jamming attacks in FSO-based networks can be caused by either proactive or reactive jammers. Proactive jammers indiscriminately transmit interference without needing prior knowledge of the network infrastructure or user traffic. In contrast, reactive jammers monitor the network and initiate jamming only upon detecting activity on a communication channel. As compared to proactive jamming, reactive jamming is an energy-efficient technique as it optimally utilizes its transmit power to disrupt legitimate transmissions.

Several prior works have presented various methods, including detection, prevention, and countermeasures, to handle jamming threats in FSO-based networks. In [138], the authors proposed a countermeasure approach based on the Multi-Channel Ratio (MCR) variation, allowing the recovery of transmitted signals in the presence of a jamming attack in UAV-based FSO networks. In [139], the authors devised a method to counteract jammer attacks on a MISO FSO-based network by implementing an aperture selection technique. In [140], the authors considered the use of a friendly jammer that transmits an optical beam modulating a pseudo-random sequence towards the eavesdropper to prevent it from decoding legitimate information. In [141], the authors employed artificial noise injection to enhance the security of communication between the legitimate transmitter and receiver, effectively thwarting Eve from intercepting the information. In [13], the authors introduced a new scheme to allocate mirror elements optimally in indoor optical wireless communication networks. However, in this mirror element assignment scheme, only indoor optical channel conditions are considered to guarantee demand rates to the users under a non-jamming environment. It is evident from the above that most prior work achieves tolerance against jamming attacks in FSO-based networks by improving the network's diversity order through multiple transmit apertures, buffer usage, or deploying OIRS. However, these approaches are both costly and inconvenient due to the substantial hardware changes required. Therefore, it is necessary to develop a jamming-resilient optimization framework to improve the survivability of FSO-based networks

6.7.1 Motivation and our Contributions

FSO technology is expected to deliver high data rates and fulfill the key requirements of next-generation networks. However, jamming attacks pose a significant security threat to FSO-based networks. These jamming attacks are a major source of transmission failures, as they can interrupt optical channel transmissions by sending jamming signals either proactively or reactively, preventing users from accessing the network. Integrating OIRS and UAVs within FSO-based network is considered a promising approach to counteract the vulnerabilities of FSO channels, including inherent anomalies and jamming attacks. Consequently, it is necessary to develop a jamming-resilient mechanism to ensure reliability and sustainability in OIRS and UAV-assisted FSO networks. In this chapter, we present a novel mirror element allocation scheme designed to mitigate reactive jamming attacks in such networks while satisfying a set of QoS requirements for the users. This proposed mirror element allocation scheme takes into account the FSO channel's characteristics and users' demand rate requirements while being jamming-aware. Specifically, we introduce a Reactive Jamming Aware-Mirror Element Allocation (RJA-MEA) scheme that considers the unique characteristics of FSO-based networks, including FSO

channel conditions, jamming attack levels, and users' QoS requirements. The primary aim of the RJA-MEA scheme is to maximize the number of served users by performing simultaneous reactive jamming-aware mirror element allocation decisions while satisfying a set of design constraints. The main contributions of this chapter are summarized as follows:

1. Formulating the batch-based multimirror element allocation problem takes into account FSO channel conditions and user rate demands while being aware of the reactive jamming attacks, which have been shown to be NLBP problem.

2. Linearizing NLBP problem through mathematical manipulations.

3. Solving the linearized NLBP problem and implementing polynomial-time SFLP method to iteratively and simultaneously assign suitable mirror elements to legitimate users, ensuring that the allocation is jamming-aware.

4. Conducting rigorous simulations to evaluate the proposed RJA-MEA scheme under various conditions, including user rate demand, achieved sum rate, and severity of reactive jamming.

5. Comparing the performance of the RJA-MEA scheme with respect to conventional schemes such as the Reactive Jamming UnAware-Mirror Element Allocation (RJU-MEA) schemes [13], Reactive Jamming Aware-Equal Mirror element Allocation (RJA-EMEA) and Reactive Jamming Unaware-Equal Mirror element Allocation (RJU-EMEA) schemes [13].

6.8 System Model & Jamming Analysis

6.8.1 System Model

We consider an OIRS-capable UAV-assisted FSO-based network operating in a reactive jammed environment with a set of $\mathcal{U}$ users, where $U = |\mathcal{U}|$ denotes the number of users. These U users are uniformly distributed in a 3D outdoor space defined by coordinates (x, y, z), as illustrated in Fig. 6.8. An optical transmitter employs a laser source to transmit information to users through an OIRS-assisted UAV, with each user equipped with a PD as an optical receiver. In the proposed network, an OIRS-assisted UAV functions as a relay between the laser source and the receivers. This configuration effectively mitigates the impact of jamming and addresses the non-LoS communication issue. Considered OIRS in this chapter is a mirror-based OIRS. This type of IRS uses multiple micro-mirror elements that can mechanically adjust their orientations to converge the optical beam in the desired direction [12, 13, 17]. Each mirror element can be independently oriented via mechanical steering gears, controlled by a dedicated controller on the OIRS-assisted UAV [13]. Furthermore, the localization mechanism is utilized to transmit the location of users to the OIRS-assisted UAV via beacon messages [99, 109]. With this information, the controller computes the appropriate mirror elements for each user using the proposed allocation schemes and adjusts their orientation accordingly to target the specific user as shown [13]. Let $\mathcal{M}$ denote the set containing M mirror elements, where $M = |\mathcal{M}|$ represents the total number of mirror elements in the mirror-based OIRS. The positions of the OIRS-assisted UAV, laser source, and each mirror element

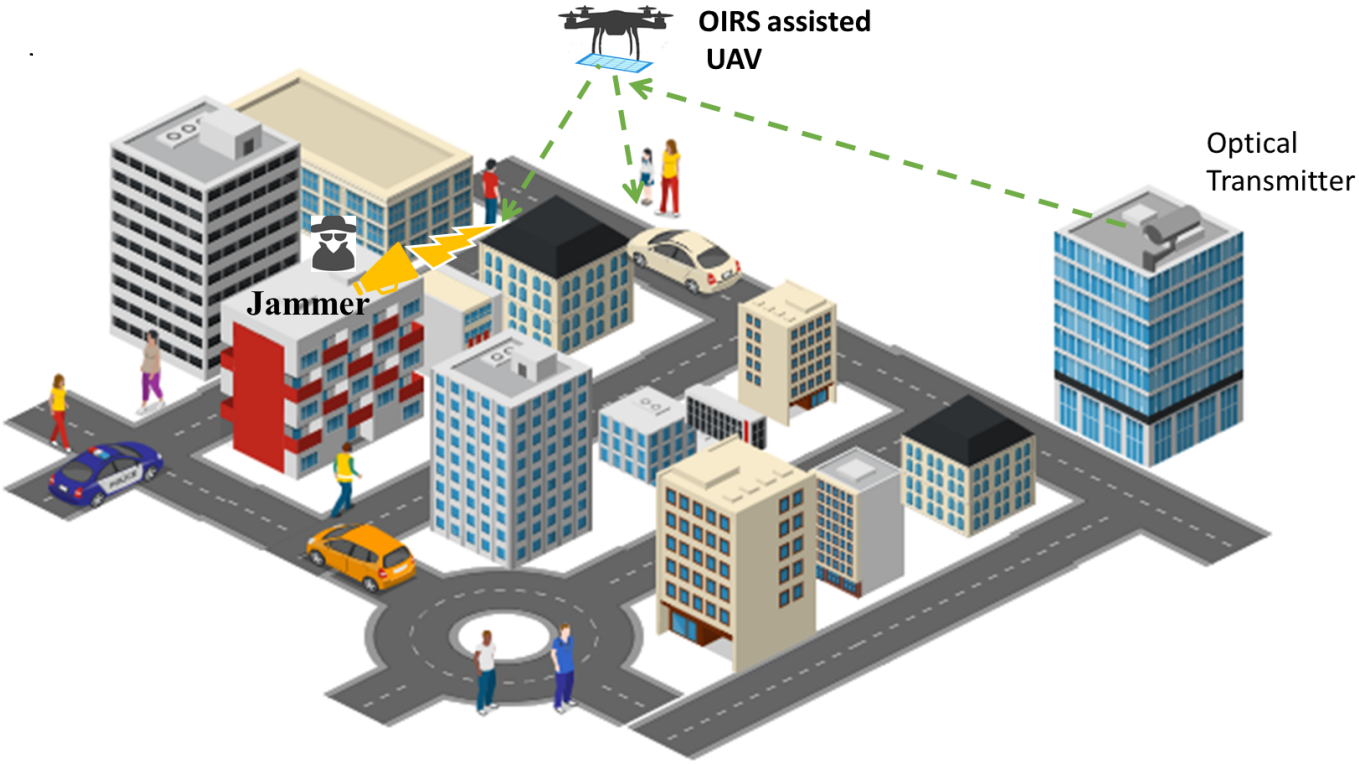

Figure 6.8: System model

of OIRS are represented using 3D coordinates (x, y, z). Moreover, we consider that the FSO communication links between the laser source and the OIRS-assisted UAV, and between the OIRS-assisted UAV and each user, are affected by atmospheric turbulence, atmospheric attenuation, misalignment errors due to the hovering OIRS-assisted UAV, and AoA fluctuations [46].

In this chapter, we may investigate reactive jamming attacks that disrupt legitimate transmissions by specifically targeting the receiver's aperture. These reactive jammers actively monitor the network and engage in jamming only when they detect ongoing transmission activities. In reactive jamming scenarios, successful packet delivery is contingent on ensuring that the packet is transmitted without interference from the jamming signals.

6.8.2 SNR and Rate Analysis

We assume that the OIRS is composed of multiple mirror elements, with the controller of the OIRS-assisted UAV governing the movement of each mirror element through a reliable and error-free link [17] and is defined in Chapter 2.

The FSO channel between the laser source and the receiver is modeled as a fading channel affected by atmospheric attenuation h_a, atmospheric turbulence (h_{at}), and pointing errors caused by beam misalignment (h_{pe}), as well as interruptions due to AoA fluctuations (h_{AoA}). The atmospheric turbulence h_{at} follows the Gamma-Gamma distribution model, and its PDF is defined as in [137]. Attenuation h_a along the FSO link is estimated using the Beer-Lambert law, as described in [46, 137]. The pointing error h_{pe} arises due to beam misalignment between the stationary laser source and the hovering OIRS-assisted UAV, and are computed ac-

cording to methods outlined in [137]. Additionally, fluctuations in AoA due to the hovering of OIRS-assisted UAV are considered, affecting network performance. The AoA fluctuation h_{AoA} is modeled as in [111]. Therefore, for transmitting information, the OIRS and UAV-assisted FSO channel is represented as the product of all the mentioned impairments, denoted as $h_F = h_{at}h_a h_{pe}h_{AoA}$. Consequently, the SNR of a user can be computed as follows:

$$\gamma_j = \frac{\left[\Re_j \mathcal{P}_j(x,y)a_j h_F\right]^2}{n_c \mathcal{B}}, \tag{6.15}$$

where $\Re_j$ is responsivity of the receiver's PD, a_j represents the effective area of the receiver's PD [113], $\mathcal{B}$ is bandwidth, and n_c is the AWGN with zero mean and variance σ_n^2. Consequently, the achievable transmission rate (in bits/s/Hz) for the jth user can be calculated as [130]:

$$R_j = \frac{1}{2}\log_2(1+\gamma_j). \tag{6.16}$$

6.8.3 Reactive Jamming Analysis

The probability of packet failure due to a reactive jamming attack is a critical metric for evaluating the performance of the communication system. To derive an expression for the failure probability P_f of packet transmission under a reactive jamming attack, we observe that a transmission will be successful if the following three independent events occur simultaneously:

- In the presence of jamming, a transmission will be successful if there are no users within the coverage area of the jammer's beam footprint, denoted by $A_j = \pi\omega_{L_F}^2$. The number of users within this area is modeled as a Poisson-distributed random variable with a mean $A_j\rho$, where ρ is the spatial density of the users.
- During legitimate transmission, the packet remains unaffected by jamming.
- Transmission succeeds when the jammer's transmission is not directed towards the user (i.e., a miss event occurs) within the specified region. The direction of the jamming attack uniformly affects various sub-regions within a given area, that is $\Pr\{u_r\} = 1/U$ for $1 \le u_r \le U$.

A closed-form expression for the probability of successful transmission, considering a given user density ρ in the presence of a jammer, can be derived as follows:

$$\begin{aligned} P_s &= (\Pr(\text{No user under } A_j)) \times (\{1-P_J\}) \times (1-\Pr(u_r)), \\ &= [1-(1-\exp^{-A_j\rho})] \times (\{1-P_J\}) \times (1-\Pr(u_r)), \\ &= \exp^{-(A_j\rho)} \times (1-(1/U)) \times (P_J). \end{aligned} \tag{6.17}$$

where P_J represents the probability of jamming. Accordingly, the expression for the failure probability after N_r re-transmission attempts calculated as follows:

$$P_f = (1-P_s)^{N_r} = (1-(\exp^{-(A_j\rho)} \times (1-(1/U)) \times (1-P_J)))^{N_r}. \tag{6.18}$$

To provide a QoS guarantee on system performance under reactive jamming, the failure probability after N_r retransmission attempts should be less than a threshold Λ as follows: Hence,

$$P_f \le \sqrt[N_r]{\Lambda}. \tag{6.19}$$

After performing some algebraic manipulations, the failure probability constraint for a given mirror element allocation can be formulated in terms of the jamming and transmission parameters as follows:

$$\ln\left(U(1-\sqrt[N_r]{\Lambda})\right)+A_j\rho\leq\sum_{i\in\mathcal{M}}\left(\ln(1-P_J^{(i)})\right). \tag{6.20}$$

6.9 Reactive Jamming Aware Mirror Element Allocation Problem

6.9.1 Problem Statement and Design Constraints

Our problem statement is as follows: given the set of mirror elements $\mathcal{M}$ with optimal deflection angles $\theta_j^{(i)*}$, and considering the set of competing legitimate users $\mathcal{U}$ with rate demands R_j^D for all $j\in\mathcal{U}$, our objective is to determine a reactive jamming-resilient allocation of mirror elements. This allocation seeks to maximize the number of users served at the same time while complying with the design constraints outlined below.

C.1.) **Rate demand**: This constraint allows each jth user to choose multiple mirror elements to meet the required rate demand R_j^D.

C.2.) **Failure probability constraint**: This constraint guarantees that the failure probability P_f of a link does not exceed a predefined threshold value Λ.

C.3.) **Mirror element constraint**: This constraint specifies that each mirror element can be assigned to only one user.

C.4.) **Resource constraint**: This limitation allows each user to be assigned a maximum of κ mirror elements.

6.9.2 Problem Formulation

The main objective is to maximize the number of served users under a reactive jamming attack, which can be formulated mathematically as:

$$\sum_{j\in\mathcal{U}}\mathbf{1}\left[\sum_{i=1}^{M}\chi_j^{(i)}\geq 1\right], \tag{6.21}$$

where $\mathbf{1}[.]$ denotes the indicator function. For the given data transmission, the design constraints can be rewritten in terms of a binary decision variable $\chi_j^{(i)}$ described as follows:

$$\chi_j^{(i)}=\begin{cases}1, & \text{if mirror element i is assigned to user j}\\ 0, & \text{otherwise.}\end{cases} \tag{6.22}$$

In reactive jamming, the failure probability constraint in (6.20) can be rewritten in terms of the binary decision variable $\chi_j^{(i)}$ as follows.

$$\sum_{i=1}^{M}\left(\ln(\left(U(1-\sqrt[N_r]{\Lambda})\right))R_j^{(i)}+A_j\rho\right)\chi_j^{(i)}\leq\sum_{i=1}^{M}\sum_{k=1}^{M}\ln(1-P_J^{(i)})R_j^{(k)}\chi_j^{(i)}\chi_j^{(k)} \tag{6.23}$$

where $R_j^{(i,\theta_j^{(i)*})}$ denotes the rate of the jth user. After some algebraic manipulation, (6.23) can be rewritten in a linear form as:

$$\sum_{i=1}^{M}b_j^{(i)}\chi_j^{(i)}\leq\sum_{i=1}^{M}\sum_{k=1}^{M}c_j^{(ik)}\chi_j^{(i)}\chi_j^{(k)} \tag{6.24}$$

In order to linearize (6.24)[1], the quadratic term $\chi_j^{(i)}\chi_j^{(k)}$ is replaced with a new binary variable $w_j^{(ik)}$ and introduced the following linear set constraints on $w_j^{(ik)}$ as follows:

$$w_j^{(ik)} \leq \chi_j^{(i)}, \quad \forall j \in \mathcal{U},\ i,k \in \mathcal{M} \tag{6.25}$$

$$w_j^{(ik)} \leq \chi_j^{(k)}, \quad \forall j \in \mathcal{U},\ i,k \in \mathcal{M} \tag{6.26}$$

$$w_j^{(ik)} \geq \chi_j^{(i)} + \chi_j^{(k)} - 1 \quad \forall j \in \mathcal{U},\ i,k \in \mathcal{M} \tag{6.27}$$

It may be noted that if either $\chi_j^{(i)}$ or $\chi_j^{(k)} = 0$, then $w_j^{(ik)} = 0$ and if both $\chi_j^{(i)}$ or $\chi_j^{(k)} = 1$, then, $w_j^{(ik)} = 1$. Thus, it is an exact formulation. This will yield $3 \times \mathcal{M} \times \mathcal{M}$ constraints to the problem formulation. Thus, the constraint in (6.24) can be re-written as:

$$\begin{aligned}
&\sum_{i=1}^{M} b_j^{(i)}\chi_j^{(i)} \leq \sum_{i=1}^{M}\sum_{k=1}^{M} c_j^{(ik)}\chi_j^{(i)}\chi_j^{(k)} \\
&w_j^{(ik)} \leq \chi_j^{(i)}, \quad \forall j \in \mathcal{U},\ i,k \in \mathcal{M} \\
&w_j^{(ik)} \leq \chi_j^{(k)}, \quad \forall j \in \mathcal{U},\ i,k \in \mathcal{M} \\
&w_j^{(ik)} \geq \chi_j^{(i)} + \chi_j^{(k)} - 1, \quad \forall j \in \mathcal{U},\ i,k \in \mathcal{M}.
\end{aligned} \tag{6.28}$$

Now, we have $\mathcal{M}\chi_j^{(i)}$ variables and $\mathcal{M}^2 w_j^{(ik)}$ variables. By substituting the non-linear constraint with its equivalent linear form as given in (6.28), the main objective function in (6.21) with design constraints in (C1–C4) under reactive jamming can be re-formulated as follows:

Given the main objective function in (6.21) with design constraints in (C1–C4), our problem can be formulated as follows.

$$\begin{aligned}
\mathbf{P1}: \underset{\chi_j^{(i)},\ w_j^{(ik)}}{\text{maximize}} \ & \sum_{j\in\mathcal{U}} \mathbf{1}\left[\sum_{i=1}^{M}\chi_j^{(i)} \geq 1\right] \\
s.t. \ & \sum_{i\in\mathcal{M}} R_j^{(i,\theta_j^{(i)*})}\chi_j^{(i)} \geq R_j^D \text{ or } 0, \ \forall j \in \mathcal{U} \\
& \sum_{i\in\mathcal{M}} b_j^{(i)}\chi_j^{(i)} - \sum_{i\in\mathcal{M}}\sum_{k\in\mathcal{M}} c_j^{(ik)} w_j^{(ik)} \leq 0 \\
& \sum_{j\in\mathcal{U}} \chi_j^{(i)} \leq 1, \ \forall i \in \mathcal{M} \\
& \sum_{i\in\mathcal{M}} \chi_j^{(i)} \leq \kappa, \ \forall j \in \mathcal{U} \\
& w_j^{(ik)} \leq \chi_j^{(i)}, \quad \forall j \in \mathcal{U},\ \forall i,k \in \mathcal{M} \\
& w_j^{(ik)} \leq \chi_j^{(k)}, \quad \forall j \in \mathcal{U},\ \forall i,k \in \mathcal{M} \\
& w_j^{(ik)} \geq \chi_j^{(i)} + \chi_j^{(k)} - 1 \quad \forall j \in \mathcal{U},\ \forall i,k \in \mathcal{M} \\
& \chi_j^{(i)},\ w_j^{(ik)} \in \{0,1\},\ \forall j \in \mathcal{U},\ \forall i,k \in \mathcal{M}.
\end{aligned} \tag{6.29}$$

To optimize the indicator function, introducing a new binary variable ν_j and linearizing the objective function are essential. This can be achieved by incorporating two more linear constraints as follows:

$$\nu_j = \mathbf{1}\left[\sum_{i=1}^{M}\chi_j^{(i)} \geq 1\right], \ \forall j \in \mathcal{U}, \tag{6.30}$$

[1]Linear programming problems are easier to solve than non-linear ones

$$\frac{\sum_{i\in\mathcal{M}}\chi_j^{(i)}}{|\mathcal{M}|}-\nu_j\leq 0,\ \forall j\in\mathcal{U},$$
$$\nu_j-\sum_{i\in\mathcal{M}}\chi_j^{(i)}\leq 0,\ \forall j\in\mathcal{U}. \tag{6.31}$$

It is also observed that jth user is served if any of the $\chi_j^{(i)}$ is unity. Otherwise, if all $\chi_j^{(i)}$'s of the jth user are not unity, then no suitable mirror element allocation is found for the jth user. Consequently, jth user is not served. Besides this, if there is more than one feasible solution with the same maximum number of served users, then we break the tie by selecting the solution that achieves the highest rate. Therefore, to achieve this, the term $[\frac{\sum_{j\in\mathcal{U}}\sum_{i\in\mathcal{M}}\chi_j^{(i)}R_j^{(i,\theta_j^{(i)*})}}{\mathbb{R}}]<1$ is added to the objective function, where $\mathbb{R}=\sum_{j\in\mathcal{U}}\sum_{i\in\mathcal{M}}R_j^{(i,\theta_j^{(i)*})}$. To linearize the either/or constraint, we introduce two additional auxiliary binary variables, $y_1^{(j)}$ and $y_2^{(j)}$, and replace the either/or constraint in equation (6.29) with the below given linear constraints:

$$\sum_{i\in\mathcal{M}}-R_j^{(i,\theta_j^{(i)*})}\chi_j^{(i)}\leq -R_j^D+\Xi y_1^{(j)},\forall j\in\mathcal{U}$$
$$\sum_{i\in\mathcal{M}}R_j^{(i,\theta_j^{(i)*})}\chi_j^{(i)}\leq 0+\Xi y_2^{(j)},\forall j\in\mathcal{U}$$
$$y_1^{(j)}+y_2^{(j)}=1,\forall j\in\mathcal{U}, \tag{6.32}$$

where $\Xi\gg 1$. Using (6.30),(6.31),(6.32), and adding the constraints, the problem in (6.29) is re-formulated as follows:

$$\mathbf{P2}:\underset{\chi_j^{(i)},\ w_j^{(ik)},\ \nu_j,\ y_1^{(j)},\ y_2^{(j)}}{\text{maximize}}\ \sum_{j\in\mathcal{U}}\nu_j+\frac{\sum_{j\in\mathcal{U}}\sum_{i\in\mathcal{M}}\chi_j^{(i)}R_j^{(i,\theta_j^{(i)*})}}{\mathbb{R}}$$
$$s.t.\ \sum_{i\in\mathcal{M}}-R_j^{(i,\theta_j^{(i)*})}\chi_j^{(i)}\leq -R_j^D+\Xi y_1^{(j)},\ \forall j\in\mathcal{U}$$
$$\sum_{i\in\mathcal{M}}R_j^{(i,\theta_j^{(i)*})}\chi_j^{(i)}\leq 0+\Xi y_2^{(j)},\ \forall j\in\mathcal{U}$$
$$\sum_{i\in\mathcal{M}}\mathcal{A}_j^{(i)}\chi_j^{(i)}\leq 0,\ \forall j\in\mathcal{U}$$
$$\sum_{j\in\mathcal{U}}\chi_j^{(i)}\leq 1,\ \forall i\in\mathcal{M}$$
$$\sum_{i\in\mathcal{M}}\chi_j^{(i)}\leq\kappa,\ \forall j\in\mathcal{U}$$
$$\frac{\sum_{i\in\mathcal{M}}\chi_j^{(i)}}{|\mathcal{M}|}-\nu_j\leq 0,\ \forall j\in\mathcal{U},$$
$$\nu_j-\sum_{i\in\mathcal{M}}\chi_j^{(i)}\leq 0,\ \forall j\in\mathcal{U}$$
$$w_j^{(ik)}\leq\chi_j^{(i)},\quad \forall j\in\mathcal{U},\ \forall i,k\in\mathcal{M}$$
$$w_j^{(ik)}\leq\chi_j^{(k)},\quad \forall j\in\mathcal{U},\ \forall i,k\in\mathcal{M}$$
$$w_j^{(ik)}\geq\chi_j^{(i)}+\chi_j^{(k)}-1,\quad \forall j\in\mathcal{U},\ \forall i,k\in\mathcal{M}$$
$$y_1^{(j)}+y_2^{(j)}=1,\ \forall j\in\mathcal{U}.$$
$$\chi_j^{(i)},\ w_j^{(ik)},\ y_1^{(j)},\ y_2^{(j)}\in\{0,1\}\ \forall j\in\mathcal{U},\ \forall i,k\in\mathcal{M}. \tag{6.33}$$

6.9.3 The Proposed Solution

Upon analyzing the formulated optimization problem in (6.33), it is apparent that this formulation resembles a BLP problem, which is known to be NP-hard. There are many other ways to solve the BLP, including cutting plane methods, decomposition methods, branch-and-bound methods, gradient ascent-based method, and greedy-based method [142–144]. However, our investigation of the multi-mirror element multi-user matching problem is known to be an NP-hard combinatorial optimization problem. Consequently, finding the closed-form solution in polynomial time for this problem is impossible for this problem [115]. Specifically, our formulated optimization problem is a BLP, where the optimal solution to such a problem is, in general, NP-hard. Such problems can be solved through an exhaustive search by searching of all possible combinations of mirror element-user allocations. However, the search space for possible combinations grows exponentially with the number of users U and mirror elements M. Therefore, we employ a BSFLP procedure, as proposed in [131–133], to approximate a near-optimal solution to the optimization problem described in (6.33) in polynomial time. The BSFLP procedure has been successfully applied to solve similar optimization problems in previous research. It has been demonstrated that suboptimal solutions for BLP problems can be attained within polynomial time [131–133].

6.10 Performance Evaluation

This section examines the performance of the proposed RJA-MEA scheme under varying levels of reactive jamming attacks. Specifically, the RJA-MEA scheme is compared against three reference schemes: RJU-MEA [13], RJA-EMEA, and RJU-EMEA schemes [13]. In the RJU-MEA scheme, mirror elements are allocated to each user without considering jamming attacks, i.e., Reactive Jamming Unaware (RJU). In contrast, the RJA-EMEA and RJU-EMEA schemes allocate an equivalent number of mirror elements to the users, with the former accounting for jamming attacks and the latter not considering them. Performance evaluation of the RJA-MEA and other reference schemes is performed using Monte Carlo simulations to compute the average sum rate and blocking probability.

6.10.1 Simulation Setup

In this chapter, we consider an OIRS-assisted UAV-based FSO network with $M = |\mathcal{M}|$ mirror elements and $U = |\mathcal{U}|$ legitimate users. The network's optical transmitter employs a laser source operating at 1550 nm to generate an optical beam directed towards the OIRS surface on the UAV. The OIRS-assisted UAV hovers at a vertical height of 50 m within an outdoor area of 100 m $\times$ 100 m, where the U users are uniformly distributed. The optical transmitter is assumed to be 200 m from the OIRS-assisted optical UAV, with the transmitter positioned at a height of 10 m. We establish $R_j^D = R_D, \forall j \in U$, with a data packet length $L = 2$ kB, a threshold Λ set to 0.1, and the maximum number of permitted retransmissions $N_r = 4$. In our simulations, we assume that the jammer's position is fixed and the reactive jammer is programmed to continuously emit a high-output optical beam based on the parameter P_J^{Max}. The simulation parameters used for performance evaluation are detailed in TABLE 6.2.

Table 6.2: Simulation parameters considered in OIRS-assisted UAV-based FSO network

Parameters	Simulation values
P_T	80 mW
$\Re$	0.5 A/W
A_{PD}	7 mm^2
λ	1550 nm
a	5 cm
$G(\varphi)$	1
$C_n^2(0)$	1×10^{-13} $m^{-2/3}$
σ_j	30 cm
σ_n^2	$10^{-15} A^2/Hz$

6.10.2 Simulation Results

In this section, we assess the sum rate performance of RJA-MEA, RJU-MEA, RJA-EMEA, and RJU-EMEA schemes relative to rate demand R_D in an OIRS-assisted UAV-based FSO network under varying degrees of reactive jamming attacks. Fig. 6.9 (a)–(c) presents the average sum rate as a function of the rate demands R_D under low, moderate, and strong jamming attacks when $U = 6$ and $M = 36$. Figs. 6.9 (a)–(c) indicate that as U and M increase, the average sum rate improves across all schemes, especially noticeable at lower values of R_D. This improvement stems from the increased number of mirror elements M, which enhances the sum rate achievable by users under lower R_D. Additionally, RJA-MEA, RJA-EMEA, RJU-MEA, and RJU-EMEA exhibit similar performance across different levels of jamming attacks, particularly noticeable at higher R_D. Notably, RJA-MEA performs exceptionally well when R_D is low, regardless of the level of jamming attack. Figs. 6.9 (d)–(f) plot the average sum rate of users against the rate demand R_D under varying levels of reactive jamming attacks, with $U = 8$ and $M = 64$. Increasing the number of mirror elements M and users U enhances the overall achievable sum rate, even at higher rate demands R_D, regardless of the level of jamming attack. Generally, under light jamming attacks, all schemes have a greater potential to serve more users, regardless of R_D, thus significantly improving the network sum rate. However, due to its awareness of the demand for rate and its effective handling of jamming, the RJA-MEA scheme significantly outperforms other schemes at low values R_D and under moderate to strong jamming attacks.

Fig. 6.10 illustrates the average sum rate as a function of the number of mirror elements M for $U = 4$ at rate demands $R_D = 2$ and 3.5 bps/Hz. The RJA-MEA scheme achieves the highest average sum rate compared to the RJU-MEA, RJU-EMEA, and RJA-EMEA schemes. However, as the number of mirror elements M increases, the sum rate performance of the RJA-MEA, RJU-MEA, and RJA-EMEA schemes consistently improves. Figs. 6.10 (a)-(c) demonstrate that the average sum rate of RJA-MEA improves significantly compared to other schemes, particularly at higher values of M and lower values of $R_D = 2$ bps/Hz. This enhancement occurs because more users can be served by effectively utilizing mirror elements, thereby enhancing the network's overall performance in terms of average sum rate. Furthermore, it is observed that the sum rate performance of the RJU-EMEA and RJA-EMEA schemes is nearly equal to each other at lower values of M. It is also observed that with a lower value of M, the sum rate achieved by the RJA-MEA scheme is higher at $R_D = 2$ bps/Hz compared to

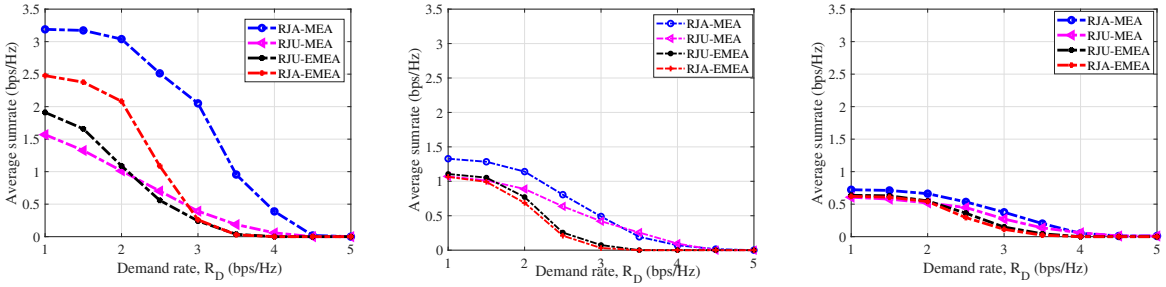

(a) Under light jamming attacks for U= 6, M= 36

(b) Under moderate jamming attacks for U= 6, M= 36

(c) Under strong jamming attacks for U= 6, M= 36

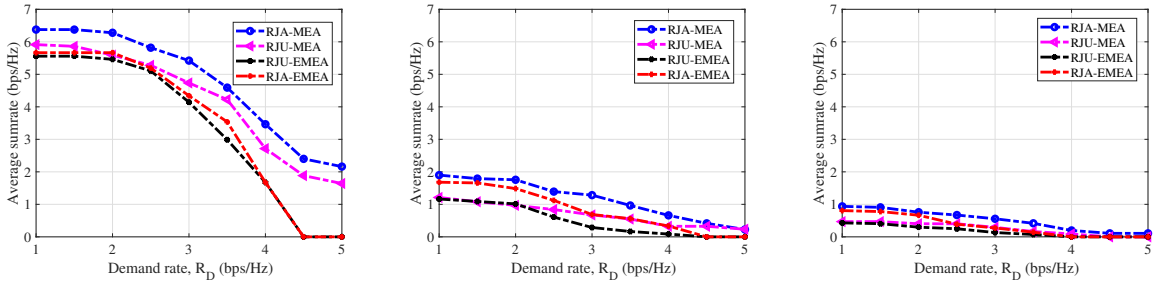

(d) Under light jamming attacks for U= 8, M= 64

(e) Under moderate jamming attacks for U= 8, M= 64

(f) Under strong jamming attacks for U= 8, M= 64

Figure 6.9: Average sum rate performance of RJA-MEA, RJA-EMEA, RJU-MEA, and RJU-EMEA schemes versus rate demand R_D

R_D = 3.5 bps/Hz. Achieving R_D = 3.5 bps/Hz requires more mirror elements for users. However, it is less feasible to achieve R_D = 3.5 bps/Hz with a lower value of M. Figs. 6.10 (d)-(f) It is evident that RJU-EMEA and RJA-EMEA do not improve the sum rate performance significantly with higher values of M, particularly in environments with strong jamming attacks and a high demand rate of R_D = 3.5 bps/Hz. However, under higher rate demands, the RJA-MEA scheme shows a substantial improvement in the sum rate compared to RJU-MEA and other schemes with a larger number of mirror elements, such as M = 64.

Figs. 6.11 (a)-(b) illustrate the average sum rate as a function of the maximum jamming probability P_J^{Max} for all schemes across various configurations: $U = 4$ $M = 16$ and $U = 6$ $M = 36$. As P_J^{Max} increases, the average sum rate decreases across all schemes. Furthermore, it is evident that the sum rate is inversely proportional to P_J^{Max}, reaching its lowest value at $P_J^{Max} = 0.5$, when jamming attacks are the most intense. At lower P_J^{Max}, the sum rate performance of the RJ-MEA scheme surpasses that of other schemes in all configurations, especially when R_D = 2 bps/Hz.

6.11 Optimizing OIRS and UAV-assisted FSO networks Under Reactive Jamming: Key Findings and Insights

This chapter focuses on optimizing the allocation of mirror elements in an OIRS and UAV-assisted FSO-based network under reactive jamming attacks. In this scenario, jammers actively monitor legitimate transmissions and launch attacks only when they detect ongoing transmission activities. An optimization problem is formulated

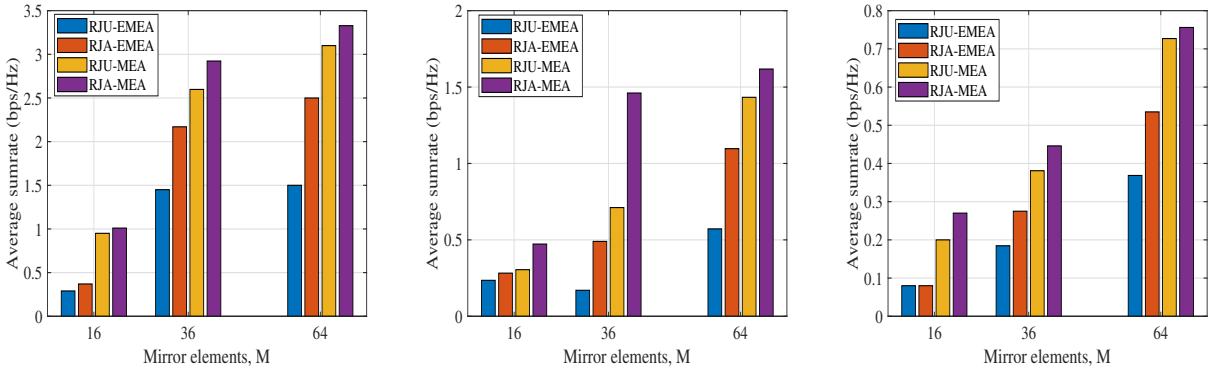

(a) Under light attacks, when R_D= 2 bps/Hz (b) Under moderate attacks, when R_D= 2 bps/Hz (c) Under strong attacks, when R_D= 2 bps/Hz

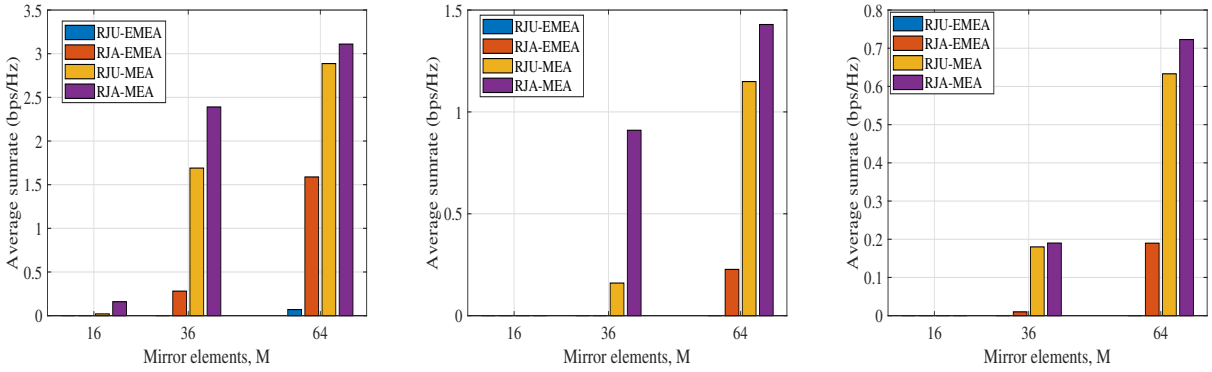

(d) Under light attacks, when R_D= 3.5 bps/Hz (e) Under moderate attacks, when R_D= 3.5 bps/Hz (f) Under strong attacks, when R_D= 3.5 bps/Hz

Figure 6.10: Achieved sum rate of RJA-MEA, RJA-EMEA, RJU-MEA, and RJU-EMEA schemes versus number of mirror elements M for $U = 4$.

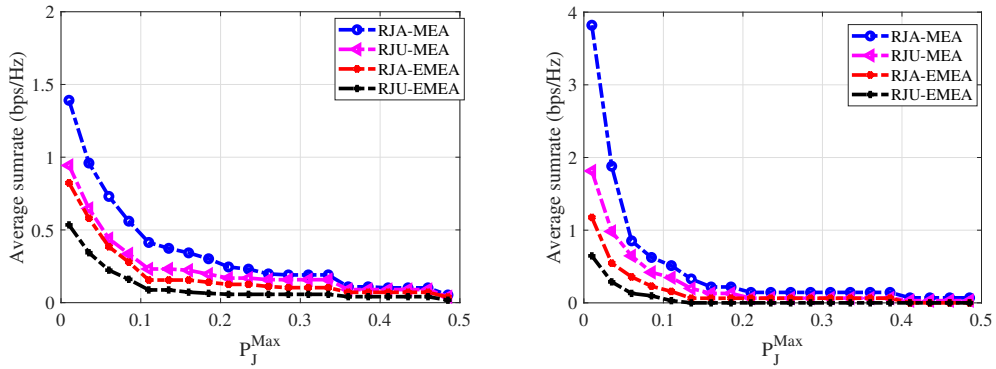

(a) When U= 4, M= 16 (b) When U= 6, M= 36

Figure 6.11: Achievable aggregate sum rate of the RJA-MEA, RJA-EMEA, RJU-MEA, and RJU-EMEA schemes versus Probability of Jamming P_J^{Max} in case of $R_D = 2$ bps/Hz

to aim at enhancing network performance in terms of sum rate while meeting user rate demands and addressing jamming constraints. To accommodate user rate demands under a reactive jamming scenario, we propose a scheme called RJA-MEA. This scheme optimally assigns mirror elements to users with built-in jamming awareness. Furthermore, we compared the performance of the RJA-MEA scheme with the reference schemes: RJU-MEA, RJU-EMEA, and RJA-EMEA. The results indicated that the proposed RJA-MEA improves the sum-rate performance, particularly with increased availability of mirror elements and lower rate demands from users. The simulation results demonstrate that the RJA-MEA scheme can effectively meet the required lower rate demands across multiple users, even in reactive jamming environments.

6.12 A Use case: Jamming-aware FSO-based vehicular network

Vehicular communication has become a transformative technology within intelligent transportation systems, significantly enhancing how vehicles interact on the road [145]. In today's densely populated and technologically advanced environments, traffic accidents remain a pressing issue, often resulting in substantial loss of life and property. Vehicular communication addresses this challenge by enabling real-time data exchange among vehicles, supporting the transmission of critical information such as location, speed, acceleration, and direction. This capability enhances road safety, optimizes traffic flow, improves fuel efficiency, and elevates the overall driving experience [146]. In recent years, vehicular optical wireless communication has emerged as a cost-effective and high-performance solution that meets the stringent demands of modern vehicular networks. It offers high data rates, wide bandwidth, minimal interference, and enhanced security. To meet these requirements, this use case leverages FSO communication for vehicle-to-infrastructure links to deliver emergency or safety-critical messages to vehicles.

We consider a model comprising a road network with vehicles equipped with optical transceivers that communicate with FSO-based roadside units via vehicle-to-infrastructure communication, as illustrated in Fig. 6.12. The system adopts an all-optical dual-hop architecture, where FSO-based roadside unit-2 acts as a relay. In the event of a vehicular collision near roadside unit-1, the unit initiates emergency messaging using a laser source to transmit information symbols modulated via intensity modulation and direct detection (IM/DD) and OOK. The optical beam is directed to roadside unit-2, which performs a decode-and-forward operation by demodulating, re-encoding, and retransmitting the emergency message toward the emergency vehicle [147]. However, this FSO link is susceptible to jamming attacks, where an adversary attempts to disrupt communication by injecting optical interference into the roadside unit-2's receiver. Furthermore, FSO channel impairments—such as atmospheric attenuation, turbulence, and pointing errors—affect both legitimate and malicious transmissions.

To ensure secure and reliable transmission of emergency messages under such adversarial and degraded conditions, an OIRS-assisted UAV is deployed as a dynamic airborne relay. This OIRS-assisted UAV maintains LoS connectivity, adapts to environmental variations, and avoids interference factors essential for sustaining robust communication. The proposed JA-MEA and RJA-MEA schemes can be applied in real time to dynamically assign mirror elements, redirect FSO beams, prioritize time-sensitive transmissions, and uphold fairness and quality of service QoS throughout the network.

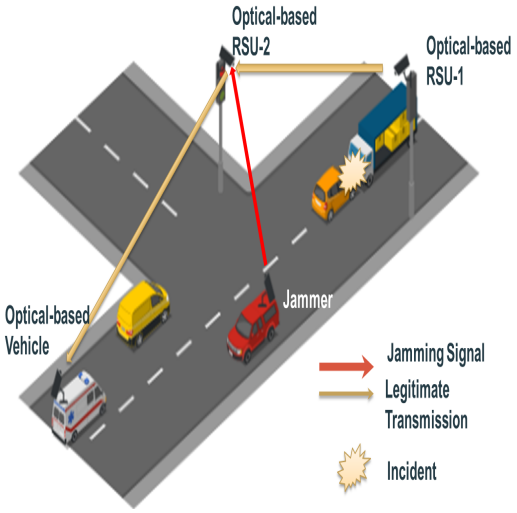

Figure 6.12: FSO-based vehicular network under jamming attack.

6.13 Chapter Summary

This chapter addresses the challenge of ensuring secure and reliable OIRS and UAV-assisted FSO networks, particularly in the presence of jamming attacks. The focus is on two major types of jamming threats: proactive and reactive jamming. In proactive jamming, the jammer does not possess prior knowledge of legitimate transmissions and attempts to disrupt communication indiscriminately. In contrast, reactive jamming involves actively monitoring the network and launching attacks only when ongoing transmissions are detected, making it more sophisticated and harder to mitigate. Part I of this chapter investigates the jamming-resilient mirror element allocation scheme for OIRS and UAV-assisted FSO network under a proactive jamming environment. The mirror element allocation problem is modeled as a binary non-linear optimization problem, aiming to maximize the average data rate per user while satisfying QoS and design constraints. To address user rate demands in the presence of proactive jamming, a scheme named JA-MEA is proposed. The performance of the JA-MEA scheme is benchmarked against reference schemes such as JU-MEA, JU-EMA, and JA-EMA. The reported results reveal that the proposed JA-MEA achieves improved sum rate and blocking probability performance, particularly as the number of available mirror elements increases. Part II focuses on optimizing the allocation of mirror elements in an OIRS and UAV-assisted FSO network under a reactive jamming attack. In this context, a novel scheme called RJA-MEA is introduced to meet users' rate requirements despite active adversarial interference from the attacker. The performance of RJA-MEA is compared against other reference schemes including RJU-MEA, RJU-EMEA, and RJA-EMEA. The simulation results demonstrate that the RJA-MEA scheme effectively satisfies lower-bound rate demands for multiple users, maintaining robust communication even in the presence of reactive jamming.

Chapter 7

Conclusion and Future Work

This chapter summarizes the key conclusions derived from the research presented in this thesis and highlights potential directions for future work based on the findings.

7.1 Summary of the Contribution Works

The next-generation terrestrial communication networks aim to improve key performance indicators (KPIs) such as extremely high data rates, low latency, massive device connectivity, energy efficiency, and security. However, existing RF-based wireless communication infrastructure cannot meet these stringent requirements. FSO is expected to play a significant role in delivering high QoS to users at low installation costs in future terrestrial networks. FSO offers freedom from spectrum licensing regulations and provides a wide bandwidth, making it a highly viable solution to meet the performance needs of terrestrial communication networks. In this thesis, the focus is primarily on FSO-based networks, which offer improved spectrum efficiency, although their practical deployment is constrained by channel impairments inherent to FSO technology. First, we compare the performance of hybrid architectures like FiLi, FiLA, FoWi, FoLi, and FoLA with the conventional FiWi architecture [7, 148]. These architectures are evaluated on the basis of metrics like average throughput, deployment cost, cost-per-bit, fairness, and reliability. The proposed FoWi, FoLi, and FoLA architectures provide a cost-effective alternative for short-range communications and scenarios where optical fiber installation is impractical. The performance of these architectures under varying atmospheric turbulence conditions—weak, moderate, and high—is also evaluated. The results indicate that the proposed hybrid architectures outperform the conventional FiWi architecture in cost efficiency and overall network performance.

This thesis also investigates the performance of an OWC-based integrated TAU communication framework for future 6G networks [137]. The end-to-end performance of the proposed OWC-based integrated TAU network is compared with conventional RF based TAU communication framework in terms of the outage probability. An optimization problem is formulated to minimize the outage probability in the FSO link between ONU and OSS relay by optimizing the divergence angle of the optical beam, ensuring the target data rate for the AUV. The proposed optimization solution, solved using the CODAT algorithm, shows that beam misalignment due to UAV movement can be mitigated by using a small beam divergence angle. However, a trade-off between

transmission distance and achievable data rate limits the end-to-end data rate. The results show that the OWC based integrated TAU communication framework outperforms conventional RF-based network in terms of overall performance.

Additionally, the thesis examines the performance of OIRS-assisted UAV-based FSO networks, which can enhance QoS to meet the growing demands of next-generation networks [12, 13]. The work presents an optimization problem for mirror element allocation, aimed at maximizing user data rates while maintaining QoS constraints. The proposed mirror element allocation scheme significantly outperforms conventional methods in terms of users served, average sum rate, and fairness. Notably, this scheme delivers significant performance improvements for larger numbers of users and mirror elements, providing a computationally efficient and scalable solution.

While FSO networks offer high data rates for bandwidth-intensive applications, they are more vulnerable to jamming attacks due to inherent technical limitations. This thesis extensively studies the threat of jamming attacks in OIRS-assisted UAV-based FSO based networks [63, 65, 66]. To address this, a Jamming-Aware Mirror Element Allocation scheme is proposed to optimize network performance in terms of sum rate and blocking probability while meeting users' rate demands and QoS constraints. The simulation results demonstrate that this scheme significantly improves the sum rate and reduces the blocking probability, especially in environments with a higher number of mirror elements, offering a robust solution for FSO-based networks under jamming conditions.

7.2 Future Work

There are numerous ways in which the work of this thesis can be extended. The following are some potential future research directions.

- User coverage by OIRS-assisted UAVs is significantly affected by obstacles, posing an open challenge to maximizing service areas under such conditions. Specifically, given user and obstacle locations within the network, the 3D positioning of an OIRS-assisted UAV must be optimized to serve the maximum number of users effectively.

- An UAV's flight time is significantly influenced by factors such as the number of users, onboard energy, and transmission rate. Specifically, given user locations, UAV energy reserves, and available mirror elements on the OIRS to serve users, a promising approach would be to jointly optimize the position of the OIRS-assisted UAV and the assignment of mirror elements of the OIRS. This would aim to minimize the UAV's flight time while effectively serving the users.

- Efficient network planning using multiple OIRS-assisted UAVs is crucial for 6G communication networks, yet remains an open challenge. Key questions include determining the number of UAVs required to ensure full coverage of a given geographical area. In addition, developing robust and adaptive network planning is essential to provide UAVs on-demand to effectively support user communications.

- A jamming-resilient system must enable rapid detection of the jammer and use localization algorithms to continuously track its position within the network. However, because jammers can relocate and disrupt different network segments, preventing jamming by leveraging historical data on jammer activity remains an open challenge. An intriguing direction for future research could involve developing a jamming-resilient system that incorporates real-time detection and location tracking, providing valuable insights for designing robust, practical systems.

- Developing an efficient, innovative, and practical anti-jamming strategy is essential for FSO-based networks, one capable of handling any network topology, detecting jamming activities, and locating both mobile and static jammers. While most existing anti-jamming systems are designed for fixed networks, designing one for dynamic networks presents additional challenges, as jammers can change position to evade countermeasures.

- In an OIRS-assisted UAV-based FSO network, optimizing the UAV's trajectory is essential for meeting QoS-related performance metrics, which include the UAV's onboard energy, user mobility patterns, and specific QoS requirements. An intriguing area of focus could be optimizing the trajectory of OIRS-assisted UAVs in the presence of a jammer while considering these performance metrics.

- Additionally, training an FSO-based network against jamming attacks can benefit from both supervised and unsupervised learning approaches. Supervised learning enables precise detection and classification of jamming attacks, while unsupervised learning can identify data anomalies caused by jamming activities. Effective FSO jamming mitigation often combines these methods to capitalize on their respective strengths. Moreover, a multi-class classification model could be developed to assess the severity of jamming, providing a more comprehensive defense strategy.

Bibliography

[1] A. Douik, H. Dahrouj, T. Y. Al-Naffouri, and M.-S. Alouini, "Hybrid radio/free-space optical design for next generation backhaul systems," *IEEE Transactions on Communications*, vol. 64, no. 6, pp. 2563–2577, 2016.

[2] W. Jiang, B. Han, M. A. Habibi, and H. D. Schotten, "The road towards 6G: A comprehensive survey," *IEEE Open Journal of the Communications Society*, vol. 2, pp. 334–366, 2021.

[3] Y. Zhou, L. Liu, L. Wang, N. Hui, X. Cui, J. Wu, Y. Peng, Y. Qi, and C. Xing, "Service-aware 6G: An intelligent and open network based on the convergence of communication, computing and caching," *Digital Communications and Networks*, vol. 6, no. 3, pp. 253–260, 2020.

[4] Y. Su, Y. Liu, Y. Zhou, J. Yuan, H. Cao, and J. Shi, "Broadband LEO satellite communications: Architectures and key technologies," *IEEE Wireless Communications*, vol. 26, no. 2, pp. 55–61, 2019.

[5] M. Alzenad, M. Z. Shakir, H. Yanikomeroglu, and M.-S. Alouini, "FSO-based vertical backhaul/fronthaul framework for 5G+ wireless networks," *IEEE Communications Magazine*, vol. 56, no. 1, pp. 218–224, 2018.

[6] H. Kaushal and G. Kaddoum, "Optical communication in space: Challenges and mitigation techniques," *IEEE communications surveys & tutorials*, vol. 19, no. 1, pp. 57–96, 2016.

[7] P. Singh, A. Gupta, V. A. Bohara, and A. Srivastava, "Cost effective hybrid FSO-wireless architecture for broadband access network," in *2022 International Conference on Optical Network Design and Modeling (ONDM)*, 2022, pp. 1–6.

[8] H. Haas, L. Yin, Y. Wang, and C. Chen, "What is LiFi?" *Journal of lightwave technology*, vol. 34, no. 6, pp. 1533–1544, 2016.

[9] P. Singh, H. A. Bany Salameh, V. A. Bohara, A. Srivastava, and M. Ayyash, "Opportunities and challenges of OIRS-assisted UAV-based FSO communication systems," in *2023 International Conference on Intelligent Computing, Communication, Networking and Services (ICCNS)*, 2023, pp. 92–98.

[10] M. A. Khalighi and M. Uysal, "Survey on free space optical communication: A communication theory perspective," *IEEE Communications Surveys & Tutorials*, vol. 16, no. 4, pp. 2231–2258, 2014.

[11] S. A. Al-Gailani, M. F. Mohd Salleh, A. A. Salem, R. Q. Shaddad, U. U. Sheikh, N. A. Algeelani, and T. A. Almohamad, "A survey of free space optics (FSO) communication systems, links, and networks," *IEEE Access*, vol. 9, pp. 7353–7373, 2021.

[12] P. Singh, V. A. Bohara, and A. Srivastava, "On the optimal assignment of mirror element in UAV and OIRS-assisted OWC based architecture," in *2023 IEEE 97th Vehicular Technology Conference (VTC2023-Spring)*, 2023, pp. 1–7.

[13] P. Singh, H. B. Salameh, V. A. Bohara, A. Srivastava, and M. Ayyash, "Optimizing connectivity in OIRS-assisted UAV indoor optical networks: Efficient admission control and mirror-element assignment," *IEEE Transactions on Network Science and Engineering*, pp. 1–11, 2024.

[14] H. Ajam, M. Najafi, V. Jamali, and R. Schober, "Ergodic sum rate analysis of UAV-based relay networks with mixed RF-FSO channels," *IEEE Open Journal of the Communications Society*, vol. 1, pp. 164–178, 2020.

[15] T. Zhang, X. Sun, and C. Wang, "On optimizing the divergence angle of an FSO based fronthaul link in drone assisted mobile networks," *IEEE Internet of Things Journal*, 2021.

[16] V. Jamali, H. Ajam, M. Najafi, B. Schmauss, R. Schober, and H. V. Poor, "Intelligent reflecting surface assisted free-space optical communications," *IEEE Communications Magazine*, vol. 59, no. 10, pp. 57–63, 2021.

[17] H. Wang, Z. Zhang, B. Zhu, J. Dang, L. Wu, and Y. Zhang, "Approaches to array-type optical IRSs: Schemes and comparative analysis," *Journal of Lightwave Technology*, 2022.

[18] S. Aboagye, T. M. Ngatched, O. A. Dobre, and A. R. Ndjiongue, "Intelligent reflecting surface-aided indoor visible light communication systems," *IEEE Communications Letters*, vol. 25, no. 12, pp. 3913–3917, 2021.

[19] P. Paul, M. R. Bhatnagar, and A. Jaiswal, "Jamming in free space optical systems: Mitigation and performance evaluation," *IEEE transactions on communications*, vol. 68, no. 3, pp. 1631–1647, 2019.

[20] P. Paul, S. Ghosh, and M. R. Bhatnagar, "Abating jamming in free space optical systems—a game-theoretic solution," *IEEE Transactions on Communications*, vol. 69, no. 12, pp. 8375–8387, 2021.

[21] M.-A. Khalighi, N. Schwartz, N. Aitamer, and S. Bourennane, "Fading reduction by aperture averaging and spatial diversity in optical wireless systems," *J. Opt. Commun. Netw.*, vol. 1, pp. 580–593, Nov 2009.

[22] M. A. Khalighi and M. Uysal, "Survey on free space optical communication: A communication theory perspective," *IEEE communications surveys & tutorials*, vol. 16, no. 4, pp. 2231–2258, 2014.

[23] L. C. Andrews, "Laser beam propagation through random media," in *SPIE-International Society for Optical Engineering*, 2005.

[24] P. Singh, V. A. Bohara, and A. Srivastava, "Reliable and cost effective all-optical wireless architecture for a broadband access network," *Journal of Optical Communications and Networking*, vol. 15, no. 2, pp. 98–110, 2023.

[25] M. R. Bhatnagar and Z. Ghassemlooy, "Performance analysis of Gamma–Gamma fading FSO MIMO links with pointing errors," *Journal of Lightwave technology*, vol. 34, no. 9, pp. 2158–2169, 2016.

[26] S. Sharma, A. Madhukumar, and R. Swaminathan, "Effect of pointing errors on the performance of hybrid FSO/RF networks," *IEEE Access*, vol. 7, pp. 131 418–131 434, 2019.

[27] S. Li, L. Yang, D. B. da Costa, and S. Yu, "Performance analysis of UAV-based mixed RF-UWOC transmission systems," *IEEE Transactions on Communications*, vol. 69, no. 8, pp. 5559–5572, 2021.

[28] L. Yang, Q. Zhu, S. Li, I. S. Ansari, and S. Yu, "On the performance of mixed FSO-UWOC dual-hop transmission systems," *IEEE Wireless Communications Letters*, vol. 10, no. 9, pp. 2041–2045, 2021.

[29] M. M. Azari, F. Rosas, K.-C. Chen, and S. Pollin, "Ultra reliable UAV communication using altitude and cooperation diversity," *IEEE Transactions on Communications*, vol. 66, no. 1, pp. 330–344, 2018.

[30] J. N. Laneman, D. N. Tse, and G. W. Wornell, "Cooperative diversity in wireless networks: Efficient protocols and outage behavior," *IEEE Transactions on Information theory*, vol. 50, no. 12, pp. 3062–3080, 2004.

[31] C.-H. Yeh, W.-H. Hsu, B.-Y. Wang, W.-Y. You, J.-R. Chen, C.-W. Chow, and S.-K. Liaw, "Fiber-and FSO-protected connections for long-reach TWDM access architecture with fault protection," *IEEE Access*, vol. 8, pp. 189 982–189 988, 2020.

[32] A. E. Farghal, "On the performance of OCDMA/SDM PON based on FSO under atmospheric turbulence and pointing errors," *Optics & Laser Technology*, vol. 114, pp. 196–203, 2019.

[33] C.-H. Yeh, W.-P. Lin, C.-M. Luo, Y.-R. Xie, Y.-J. Chang, and C.-W. Chow, "Utilizing single lightwave for delivering Baseband/FSO/MMW traffics simultaneously in PON architecture," *IEEE Access*, vol. 7, pp. 138 927–138 931, 2019.

[34] C.-H. Yeh, Y.-R. Xie, C.-M. Luo, and C.-W. Chow, "Integration of FSO traffic in ring-topology bidirectional fiber access network with fault protection," *IEEE Communications Letters*, vol. 24, no. 3, pp. 589–592, 2019.

[35] G. Susanna, S. Di Bartolo, D. Carleo, S. Penna, S. Betti, and A. Reale, "Weather influence on performance of a seamless free space optic (FSO) link in a PON scenario," in *2019 21st International Conference on Transparent Optical Networks (ICTON)*. IEEE, 2019, pp. 1–5.

[36] T. V. Nguyen, H. T. Nguyen, H.-C. Le, N. D. Nguyen, and N. T. Dang, "Performance analysis of Gigabit-capable mobile backhaul networks exploiting TWDM-PON and FSO technologies," in *2016 International Conference on Advanced Technologies for Communications (ATC)*. IEEE, 2016, pp. 180–185.

[37] E. E. Elsayed and B. B. Yousif, "Performance evaluation and enhancement of the modified OOK based IM/DD techniques for hybrid Fiber/FSO communication over WDM-PON systems," *Optical and Quantum Electronics*, vol. 52, no. 9, pp. 1–27, 2020.

[38] S. S. Jaffer, A. Hussain, M. A. Qureshi, J. Mirza, and K. K. Qureshi, "A low cost PON-FSO based fronthaul solution for 5G CRAN architecture," *Optical Fiber Technology*, vol. 63, p. 102500, 2021.

[39] R. Kovalchukov, D. Moltchanov, A. Samuylov, A. Ometov, S. Andreev, Y. Koucheryavy, and K. Samouylov, "Analyzing effects of directionality and random heights in drone-based mmwave communication," *IEEE Transactions on Vehicular Technology*, vol. 67, no. 10, pp. 10 064–10 069, 2018.

[40] G. A. Cap, H. H. Refai, and J. J. Sluss, "Optical tracking and auto-alignment transceiver system," in *2008 IEEE/AIAA 27th Digital Avionics Systems Conference*. IEEE, 2008, pp. 2–B.

[41] M. Khan, S. Bhunia, M. Yuksel, and L. C. Kane, "Line-of-sight discovery in 3D using highly directional transceivers," *IEEE Transactions on Mobile Computing*, vol. 18, no. 12, pp. 2885–2898, 2018.

[42] M. T. Dabiri, M. Rezaee, I. S. Ansari, and V. Yazdanian, "Channel modeling for UAV-based optical wireless links with nonzero boresight pointing errors," *IEEE Transactions on Vehicular Technology*, vol. 69, no. 12, pp. 14 238–14 246, 2020.

[43] T. Zhang, X. Sun, and C. Wang, "On optimizing the divergence angle of an FSO based fronthaul link in drone assisted mobile networks," *IEEE Internet of Things Journal*, pp. 1–1, 2021.

[44] M. T. Dabiri and S. M. S. Sadough, "Optimal placement of UAV-assisted free-space optical communication systems with DF relaying," *IEEE Communications Letters*, vol. 24, no. 1, pp. 155–158, 2020.

[45] J.-H. Lee, K.-H. Park, Y.-C. Ko, and M.-S. Alouini, "A UAV-mounted free space optical communication: Trajectory optimization for flight time," *IEEE Transactions on Wireless Communications*, vol. 19, no. 3, pp. 1610–1621, 2020.

[46] M. Najafi, H. Ajam, V. Jamali, P. D. Diamantoulakis, G. K. Karagiannidis, and R. Schober, "Statistical modeling of the FSO fronthaul channel for UAV-based communications," *IEEE Transactions on Communications*, vol. 68, no. 6, pp. 3720–3736, 2020.

[47] N. Ansari, Q. Fan, X. Sun, and L. Zhang, "Soarnet," *IEEE Wireless Communications*, vol. 26, no. 6, pp. 37–43, 2019.

[48] J. Ouyang, Y. Che, J. Xu, and K. Wu, "Throughput maximization for laser-powered UAV wireless communication systems," in *2018 IEEE International Conference on Communications Workshops (ICC Workshops)*. IEEE, 2018, pp. 1–6.

[49] W. Jaafar and H. Yanikomeroglu, "Dynamics of laser-charged uavs: A battery perspective," *IEEE Internet of Things Journal*, vol. 8, no. 13, pp. 10 573–10 582, 2020.

[50] C. Abou-Rjeily, G. Kaddoum, and G. K. Karagiannidis, "Ground-to-air FSO communications: when high data rate communication meets efficient energy harvesting with simple designs," *Optics Express*, vol. 27, no. 23, pp. 34 079–34 092, 2019.

[51] P. D. Diamantoulakis, K. N. Pappi, Z. Ma, X. Lei, P. C. Sofotasios, and G. K. Karagiannidis, "Airborne radio access networks with simultaneous lightwave information and power transfer (SLIPT)," in *2018 IEEE Global Communications Conference (GLOBECOM)*. IEEE, 2018, pp. 1–6.

[52] H. Ajam, M. Najafi, V. Jamali, B. Schmauss, and R. Schober, "Modeling and design of IRS-assisted multilink fso systems," *IEEE Transactions on Communications*, vol. 70, no. 5, pp. 3333–3349, 2022.

[53] S. Malik, P. Saxena, and Y. H. Chung, "Performance analysis of a UAV-based IRS-assisted hybrid RF/FSO link with pointing and phase shift errors," *Journal of Optical Communications and Networking*, vol. 14, no. 4, pp. 303–315, 2022.

[54] O. Bouachir, M. Aloqaily, I. A. Ridhawi, O. Alfandi, and H. B. Salameh, "UAV-assisted vehicular communication for densely crowded environments," in *NOMS 2020 - 2020 IEEE/IFIP Network Operations and Management Symposium*, 2020, pp. 1–4.

[55] T. N. Do, G. Kaddoum, T. L. Nguyen, D. B. da Costa, and Z. J. Haas, "Aerial reconfigurable intelligent surface-aided wireless communication systems," in *2021 IEEE 32nd Annual International Symposium on Personal, Indoor and Mobile Radio Communications (PIMRC)*, 2021, pp. 525–530.

[56] A. M. Salhab and L. Yang, "Mixed RF/FSO relay networks: RIS-equipped RF source vs RIS-aided RF source," *IEEE Wireless Communications Letters*, vol. 10, no. 8, pp. 1712–1716, 2021.

[57] A. R. Ndjiongue, T. M. Ngatched, O. A. Dobre, A. G. Armada, and H. Haas, "Analysis of RIS-based terrestrial-FSO link over GG turbulence with distance and jitter ratios," *Journal of Lightwave Technology*, vol. 39, no. 21, pp. 6746–6758, 2021.

[58] M. Najafi, B. Schmauss, and R. Schober, "Intelligent reflecting surfaces for free space optical communication systems," *IEEE Transactions on Communications*, vol. 69, no. 9, pp. 6134–6151, 2021.

[59] H. Ajam, M. Najafi, V. Jamali, B. Schmauss, and R. Schober, "Modeling and design of IRS-assisted multilink FSO systems," *IEEE Transactions on Communications*, vol. 70, no. 5, pp. 3333–3349, 2022.

[60] H. Pirayesh and H. Zeng, "Jamming attacks and anti-jamming strategies in wireless networks: A comprehensive survey," *IEEE communications surveys & tutorials*, vol. 24, no. 2, pp. 767–809, 2022.

[61] S. Vadlamani, B. Eksioglu, H. Medal, and A. Nandi, "Jamming attacks on wireless networks: A taxonomic survey," *International Journal of Production Economics*, vol. 172, pp. 76–94, 2016.

[62] M. A. Aref, S. K. Jayaweera, and E. Yepez, "Survey on cognitive anti-jamming communications," *IET Communications*, vol. 14, no. 18, pp. 3110–3127, 2020.

[63] P. Singh, H. B. Salameh, V. A. Bohara, A. Srivastava, and M. Ayyash, "Jamming attacks on fso networks: Challenges, opportunities, and a public safety use-case," in *2024 IEEE World Forum on Public Safety Technology (WFPST)*, 2024, pp. 7–12.

[64] P. Paul and M. R. Bhatnagar, "Jamming threats in free-space optics," *IEEE Communications Magazine*, vol. 60, no. 12, pp. 104–108, 2022.

[65] P. Singh, H. B. Salameh, V. A. Bohara, A. Srivastava, and M. Ayyash, "On mitigating reactive jamming with dynamic resource allocation in optical irs and uav-assisted fso-based networks," *Physical Communication*, p. 102520, 2024. [Online]. Available: https://www.sciencedirect.com/science/article/pii/S1874490724002386

[66] ——, "Jamming-resilient mirror element allocation scheme for oirs-aided uav-based fso networks," *IEEE Transactions on Intelligent Vehicles*, pp. 1–12, 2024.

[67] P. Paul, M. R. Bhatnagar, and A. Jaiswal, "Alleviation of jamming in Free Space Optical communication over Gamma-Gamma channel with pointing errors," *IEEE Photonics Journal*, vol. 11, no. 5, pp. 1–18, 2019.

[68] ——, "Jamming in free space optical systems: Mitigation and performance evaluation," *IEEE Transactions on Communications*, vol. 68, no. 3, pp. 1631–1647, 2020.

[69] A. K. Shukla and M. R. Bhatnagar, "Mitigating jamming in FSO cooperative networks: A buffer-aided relaying approach," *IEEE Communications Letters*, 2023.

[70] I. Chauhan and M. R. Bhatnagar, "UAV-based FSO communication under jamming," in *2022 IEEE 95th Vehicular Technology Conference: (VTC2022-Spring)*, 2022, pp. 1–5.

[71] P. Paul and M. R. Bhatnagar, "Random relay jamming in cooperative free space optical systems," *IEEE Systems Journal*, vol. 16, no. 2, pp. 2413–2424, 2022.

[72] P. Saxena and Y. H. Chung, "Analysis of jamming effects in irs assisted uav dual-hop fso communication systems," *IEEE Transactions on Vehicular Technology*, 2023.

[73] K. Wang, C. M. Machuca, L. Wosinska, P. J. Urban, A. Gavler, K. Brunnström, and J. Chen, "Techno-economic analysis of active optical network migration toward next-generation optical access," *Journal of Optical Communications and Networking*, vol. 9, no. 4, pp. 327–341, 2017.

[74] A. Gupta, N. Sharma, P. Garg, and M.-S. Alouini, "Cascaded FSO-VLC communication system," *IEEE Wireless Communications Letters*, vol. 6, no. 6, pp. 810–813, 2017.

[75] Z. Huang, Z. Wang, M. Huang, W. Li, T. Lin, P. He, and Y. Ji, "Hybrid optical wireless network for future SAGO-integrated communication based on FSO/VLC heterogeneous interconnection," *IEEE Photonics Journal*, vol. 9, no. 2, pp. 1–10, 2017.

[76] P. Pesek, S. Zvánovec, P. Chvojka, Z. Ghassemlooy, and P. A. Haigh, "Demonstration of a hybrid FSO/VLC link for the last mile and last meter networks," *IEEE Photonics Journal*, vol. 11, no. 1, pp. 1–7, 2018.

[77] R. Deka and S. Anees, "Performance analysis of DF based cascaded VLC-FSO-VLC system," in *2020 3rd International Conference on Advanced Communication Technologies and Networking (CommNet)*, 2020, pp. 1–6.

[78] R. Ahmad, M. D. Soltani, M. Safari, and A. Srivastava, "Reinforcement learning-based near-optimal load balancing for heterogeneous LiFi WiFi network," *IEEE Systems Journal*, pp. 1–12, 2021.

[79] J. Kong, Z.-Y. Wu, M. Ismail, E. Serpedin, and K. A. Qaraqe, "Q-learning based two-timescale power allocation for multi-homing hybrid RF/VLC networks," *IEEE Wireless Communications Letters*, vol. 9, no. 4, pp. 443–447, 2020.

[80] N. M. Karoti, S. Paramita, R. Ahmad, V. A. Bohara, and A. Srivastava, "Improving the performance of heterogeneous LiFi-WiFi network using a novel link aggregation framework," in *2022 IEEE Wireless Communications and Networking Conference (WCNC)*. IEEE, 2022, pp. 2322–2327.

[81] C. Zeng and S. Licardie, "Systems and methods for performing layer one link aggregation over wireless links," Sep. 1 2015, US Patent 9,125,084.

[82] X. Wu, M. Safari, and H. Haas, "Access point selection for hybrid Li-Fi and Wi-Fi networks," *IEEE Transactions on Communications*, vol. 65, no. 12, pp. 5375–5385, 2017.

[83] L. Yin, W. O. Popoola, X. Wu, and H. Haas, "Performance evaluation of non-orthogonal multiple access in visible light communication," *IEEE Transactions on Communications*, vol. 64, no. 12, pp. 5162–5175, 2016.

[84] N. I. Miridakis, M. Matthaiou, and G. K. Karagiannidis, "Multiuser relaying over mixed RF/FSO links," *IEEE Transactions on Communications*, vol. 62, no. 5, pp. 1634–1645, 2014.

[85] VPI. [Online]. Available: http://www.vpiphotonics.com/"

[86] R. Priyadarshani, M. R. Bhatnagar, Z. Ghassemlooy, and S. Zvanovec, "Effect of correlation on BER performance of the FSO-MISO system with repetition coding over gamma–gamma turbulence," *IEEE Photonics Journal*, vol. 9, no. 5, pp. 1–15, 2017.

[87] X. Song and J. Cheng, "Subcarrier intensity modulated MIMO optical communications in atmospheric turbulence," *Journal of Optical Communications and Networking*, vol. 5, no. 9, pp. 1001–1009, 2013.

[88] R. K. Jain, D.-M. W. Chiu, W. R. Hawe *et al.*, "A quantitative measure of fairness and discrimination," *Eastern Research Laboratory, Digital Equipment Corporation, Hudson, MA*, 1984.

[89] B. Kantarci and H. T. Mouftah, "Availability and cost-constrained long-reach passive optical network planning," *IEEE Transactions on Reliability*, vol. 61, no. 1, pp. 113–124, 2012.

[90] B. P. Rimal, D. P. Van, and M. Maier, "Mobile-edge computing versus centralized cloud computing over a converged FiWi access network," *IEEE Transactions on Network and Service Management*, vol. 14, no. 3, pp. 498–513, 2017.

[91] H. Beyranvand, W. Lim, M. Maier, C. Verikoukis, and J. A. Salehi, "Backhaul-aware user association in FiWi enhanced LTE-A heterogeneous networks," *IEEE Transactions on Wireless Communications*, vol. 14, no. 6, pp. 2992–3003, 2015.

[92] FSO link price. [Online]. Available: https://www.gigabit-wireless.com/tag/free-space-optics/"

[93] M. Tatarko, L. Ovseník, and J. Turán, "Properties of hybrid FSO/RF link with 60 GHz RF backup link," in *2013 36th International Convention on Information and Communication Technology, Electronics and Microelectronics (MIPRO)*, 2013, pp. 495–497.

[94] Z. Zhang, Y. Xiao, Z. Ma, M. Xiao, Z. Ding, X. Lei, G. K. Karagiannidis, and P. Fan, "6G wireless networks: Vision, requirements, architecture, and key technologies," *IEEE Vehicular Technology Magazine*, vol. 14, no. 3, pp. 28–41, 2019.

[95] H. Kaushal and G. Kaddoum, "Underwater optical wireless communication," *IEEE access*, vol. 4, pp. 1518–1547, 2016.

[96] Z. Zeng, S. Fu, H. Zhang, Y. Dong, and J. Cheng, "A survey of underwater optical wireless communications," *IEEE communications surveys & tutorials*, vol. 19, no. 1, pp. 204–238, 2016.

[97] S. Dang, O. Amin, B. Shihada, and M.-S. Alouini, "What should 6G be?" *Nature Electronics*, vol. 3, no. 1, pp. 20–29, 2020.

[98] C. Christopoulou, H. G. Sandalidis, and I. S. Ansari, "Outage probability of a multisensor mixed UOWC–FSO setup," *IEEE Sensors Letters*, vol. 3, no. 8, pp. 1–4, 2019.

[99] H.-J. Moon, H.-B. Jeon, and C.-B. Chae, "RF lens antenna array-based one-shot coarse pointing for hybrid RF/FSO communications," *IEEE Wireless Communications Letters*, 2021.

[100] A. El Gamal and Y.-H. Kim, *Network information theory*. Cambridge university press, 2011.

[101] A. Papoulis and S. U. Pillai, *Probability, random variables, and stochastic processes*. Tata McGraw-Hill Education, 2002.

[102] Q. Fan, N. Ansari, J. Feng, R. Rojas-Cessa, M. Zhou, and T. Zhang, "Reducing the number of FSO base stations with dual transceivers for next-generation ground-to-train communications," *IEEE Transactions on Vehicular Technology*, vol. 67, no. 11, pp. 11 143–11 153, 2018.

[103] M. Kong, Y. Guo, O. Alkhazragi, M. Sait, C. H. Kang, T. K. Ng, and B. S. Ooi, "Real-time optical-wireless video surveillance system for high visual-fidelity underwater monitoring," *IEEE Photonics Journal*, vol. 14, no. 2, pp. 1–9, 2022.

[104] K. H. Heng, W.-D. Zhong, T. H. Cheng, N. Liu, and Y. He, "Beam divergence changing mechanism for short-range inter-unmanned aerial vehicle optical communications," *Applied optics*, vol. 48, no. 8, pp. 1565–1572, 2009.

[105] V. V. Mai and H. Kim, "Non-mechanical beam steering and adaptive beam control using variable focus lenses for free-space optical communications," *Journal of Lightwave Technology*, vol. 39, no. 24, pp. 7600–7608, 2021.

[106] M. M. Azari, F. Rosas, K.-C. Chen, and S. Pollin, "Ultra reliable UAV communication using altitude and cooperation diversity," *IEEE Transactions on Communications*, vol. 66, no. 1, pp. 330–344, 2017.

[107] D. Park, K. Kwak, W. K. Chung, and J. Kim, "Development of underwater short-range sensor using electromagnetic wave attenuation," *IEEE Journal of Oceanic Engineering*, vol. 41, no. 2, pp. 318–325, 2015.

[108] M. Najafi, B. Schmauss, and R. Schober, "Intelligent reflecting surfaces for free space optical communication systems," *IEEE Transactions on Communications*, vol. 69, no. 9, pp. 6134–6151, 2021.

[109] Yapar, R. Levie, G. Kutyniok, and G. Caire, "Real-time outdoor localization using radio maps: A deep learning approach," *IEEE Transactions on Wireless Communications*, pp. 1–1, 2023.

[110] T. V. Nguyen, H. D. Le, and A. T. Pham, "On the design of RIS-UAV relay-assisted hybrid FSO/RF satellite-aerial-ground integrated network," *IEEE Transactions on Aerospace and Electronic Systems*, pp. 1–15, 2022.

[111] M. T. Dabiri, S. M. S. Sadough, and M. A. Khalighi, "Channel modeling and parameter optimization for hovering UAV-based free-space optical links," *IEEE Journal on Selected Areas in Communications*, vol. 36, no. 9, pp. 2104–2113, 2018.

[112] D. Singh and S. R, "Comprehensive performance analysis of hovering UAV-based FSO communication system," *IEEE Photonics Journal*, vol. 14, no. 5, pp. 1–13, 2022.

[113] Y. Kaymak, R. Rojas-Cessa, J. Feng, N. Ansari, and M. Zhou, "On divergence-angle efficiency of a laser beam in free-space optical communications for high-speed trains," *IEEE Transactions on Vehicular Technology*, vol. 66, no. 9, pp. 7677–7687, 2017.

[114] L. Yin, W. O. Popoola, X. Wu, and H. Haas, "Performance evaluation of non-orthogonal multiple access in visible light communication," *IEEE Transactions on Communications*, vol. 64, no. 12, pp. 5162–5175, 2016.

[115] G. J. Woeginger, "Exact algorithms for NP-hard problems: A survey," in *Combinatorial optimization—eureka, you shrink!* Springer, 2003, pp. 185–207.

[116] M. D. Soltani, H. Kazemi, E. Sarbazi, T. E. El-Gorashi, J. M. Elmirghani, R. V. Penty, I. H. White, H. Haas, and M. Safari, "High-speed imaging receiver design for 6G optical wireless communications: A rate-fov trade-off," *IEEE Transactions on Communications*, 2022.

[117] H. Kazemi, E. Sarbazi, M. D. Soltani, M. Safari, and H. Haas, "A Tb/s indoor optical wireless backhaul system using VCSEL arrays," in *2020 IEEE 31st Annual International Symposium on Personal, Indoor and Mobile Radio Communications*. IEEE, 2020, pp. 1–6.

[118] A. Singh, H. B. Salameh, M. Ayyash, and H. Elagla, "A novel VL-based positioning model for obstacle location sensing and 3D shape detection in crowded indoor networks," *IEEE Sensors Letters*, 2023.

[119] H. Kazemi, E. Sarbazi, M. D. Soltani, T. E. H. El-Gorashi, J. M. H. Elmirghani, R. V. Penty, I. H. White, M. Safari, and H. Haas, "A Tb/s indoor MIMO optical wireless backhaul system using VCSEL arrays," *IEEE Transactions on Communications*, vol. 70, no. 6, pp. 3995–4012, 2022.

[120] Y. Hong, F. Feng, K. R. Bottrill, N. Taengnoi, R. Singh, G. Faulkner, D. C. O'Brien, and P. Petropoulos, "Demonstration of $>$ 1Tbit/s WDM OWC with wavelength-transparent beam tracking-and-steering capability," *Optics Express*, vol. 29, no. 21, pp. 33 694–33 702, 2021.

[121] T. Koonen, K. Mekonnen, Z. Cao, F. Huijskens, N. Q. Pham, and E. Tangdiongga, "Ultra-high-capacity wireless communication by means of steered narrow optical beams," *Philosophical Transactions of the Royal Society A*, vol. 378, no. 2169, p. 20190192, 2020.

[122] R. Singh, F. Feng, Y. Hong, G. Faulkner, R. Deshmukh, G. Vercasson, O. Bouchet, P. Petropoulos, and D. O'Brien, "Design and characterisation of Terabit/s capable compact localisation and beam-steering terminals for fiber-wireless-fiber links," *Journal of Lightwave Technology*, vol. 38, no. 24, pp. 6817–6826, 2020.

[123] F. Ahmad, R. Sathisha, K. M. Jyothsna, and V. Raghunathan, "Hybrid laser-LED transmitter with closed-loop beam-steering control for indoor optical wireless communication," *Journal of Lightwave Technology*, vol. 40, no. 12, pp. 3557–3566, 2022.

[124] M. D. Soltani, E. Sarbazi, N. Bamiedakis, P. De Souza, H. Kazemi, J. M. Elmirghani, I. H. White, R. V. Penty, H. Haas, and M. Safari, "Safety analysis for laser-based optical wireless communications: A tutorial," *Proceedings of the IEEE*, 2022.

[125] N. Yu, P. Genevet, M. A. Kats, F. Aieta, J.-P. Tetienne, F. Capasso, and Z. Gaburro, "Light propagation with phase discontinuities: generalized laws of reflection and refraction," *science*, vol. 334, no. 6054, pp. 333–337, 2011.

[126] R. M. Gagliardi and S. Karp, "Optical communications," *New York*, 1976.

[127] X. Wang, X. Wang, and S. Mao, "Deep convolutional neural networks for indoor localization with CSI images," *IEEE Transactions on Network Science and Engineering*, vol. 7, no. 1, pp. 316–327, 2020.

[128] B. E. Saleh and M. C. Teich, "Fundamentals of photonics 3rd edn (hoboken," 2019.

[129] D. Wu, Z. Ghassemlooy, H. LeMinh, S. Rajbhandari, and Y. S. Kavian, "Power distribution and Q-factor analysis of diffuse cellular indoor visible light communication systems," in *2011 16th European Conference on Networks and Optical Communications*, 2011, pp. 28–31.

[130] A. Lapidoth, S. M. Moser, and M. A. Wigger, "On the capacity of free-space optical intensity channels," *IEEE Transactions on Information Theory*, vol. 55, no. 10, pp. 4449–4461, 2009.

[131] H. A. B. Salameh, H. Kasasbeh, and B. Harb, "A batch-based MAC design with simultaneous assignment decisions for improved throughput in guard-band-constrained cognitive networks," *IEEE Transactions on Communications*, vol. 64, no. 3, pp. 1143–1152, 2016.

[132] H. A. B. Salameh, M. Krunz, and D. Manzi, "Spectrum bonding and aggregation with guard-band awareness in cognitive radio networks," *IEEE Transactions on Mobile Computing*, vol. 13, no. 3, pp. 569–581, 2014.

[133] H. Bany Salameh, S. Almajali, M. Ayyash, and H. Elgala, "Batch-based security-aware spectrum sharing with simultaneous assignment decisions in time-critical IoT networks with cognitive radio capabilities," *Transactions on Emerging Telecommunications Technologies*, vol. 29, no. 11, p. e3317, 2018.

[134] H. B. Salameh and M. Al-Quraan, "Securing delay-sensitive CR-IoT networking under jamming attacks: Parallel transmission and batching perspective," *IEEE Internet of Things Journal*, vol. 7, no. 8, pp. 7529–7538, 2020.

[135] A. B. Sediq, R. H. Gohary, R. Schoenen, and H. Yanikomeroglu, "Optimal tradeoff between sum-rate efficiency and jain's fairness index in resource allocation," *IEEE Transactions on Wireless Communications*, vol. 12, no. 7, pp. 3496–3509, 2013.

[136] H. A. B. Salameh, S. Almajali, M. Ayyash, and H. Elgala, "Spectrum assignment in cognitive radio networks for internet-of-things delay-sensitive applications under jamming attacks," *IEEE Internet of Things Journal*, vol. 5, no. 3, pp. 1904–1913, 2018.

[137] P. Singh, V. A. Bohara, and A. Srivastava, "On the optimization of integrated terrestrial-air-underwater architecture using optical wireless communication for future 6G network," *IEEE Photonics Journal*, vol. 14, no. 6, pp. 1–12, 2022.

[138] M. Sliti, W. Abdallah, and N. Boudriga, "Jamming attack detection in optical UAV networks," in *2018 20th International Conference on Transparent Optical Networks (ICTON)*, 2018, pp. 1–5.

[139] I. Chauhan and M. R. Bhatnagar, "Performance of transmit aperture selection to mitigate jamming," *Applied Sciences*, vol. 12, no. 4, 2022.

[140] ——, "Information theoretic study of friendly jammer abating an eavesdropper in FSO communication," *IEEE Transactions on Communications*, vol. 72, no. 4, pp. 2106–2123, 2024.

[141] A. Sikri, A. Mathur, M. Bhatnagar, G. Kaddoum, P. Saxena, and J. Nebhen, "Artificial noise injection–based secrecy improvement for FSO systems," *IEEE Photonics Journal*, vol. 13, no. 2, pp. 1–12, 2021.

[142] L. A. Wolsey, *Integer programming*. John Wiley & Sons, 2020.

[143] Y. Yang, Y. Gong, and Y.-C. Wu, "Intelligent-reflecting-surface-aided mobile edge computing with binary offloading: Energy minimization for IoT devices," *IEEE Internet of Things Journal*, vol. 9, no. 15, pp. 12 973–12 983, 2022.

[144] ——, "Energy sensitive binary offloading for reconfigurable-intelligent-surface-assisted wireless powered mobile edge computing," *IEEE Internet of Things Journal*, 2023.

[145] S. K. Bhoi and P. M. Khilar, "Vehicular communication: a survey," *IET networks*, vol. 3, no. 3, pp. 204–217, 2014.

[146] S. Zeadally, J. Guerrero, and J. Contreras, "A tutorial survey on vehicle-to-vehicle communications," *Telecommunication Systems*, vol. 73, pp. 469–489, 2020.

[147] P. Paul and M. R. Bhatnagar, "Random relay jamming in cooperative free space optical systems," *IEEE Systems Journal*, vol. 16, no. 2, pp. 2413–2424, 2021.

[148] P. Singh, V. A. Bohara, and A. Srivastava, "Reliable and cost effective all-optical wireless architecture for a broadband access network," *J. Opt. Commun. Netw.*, vol. 15, no. 2, pp. 98–110, Feb 2023. [Online]. Available: https://opg.optica.org/jocn/abstract.cfm?URI=jocn-15-2-98